UCLA
UCLA Electronic Theses and Dissertations

Title

In the Heat of the Moment: Uncoupling Hypothalamic Cellular Identity from Marker Gene Function to Understand Murine Thermoregulatory Circuits

Permalink

https://escholarship.org/uc/item/3rj8034x

ISBN

9798173772381

Author

Sandoval, Norma Patricia

Publication Date

2026-11-09

Peer reviewed|Thesis/dissertation

eScholarship.org Powered by the California Digital Library
University of California

UNIVERSITY OF CALIFORNIA

Los Angeles

In the Heat of the Moment:

Uncoupling Hypothalamic Cellular Identity from Marker Gene Function to Understand Murine Thermoregulatory Circuits

A dissertation submitted in partial satisfaction of the requirements

for the degree Doctor of Philosophy

in Molecular, Cellular, and Integrative Physiology

by

Norma P. Sandoval

2026

©Copyright by

Norma P. Sandoval

2026

ABSTRACT OF THE DISSERTATION

In the Heat of the Moment:
Uncoupling Hypothalamic Cellular Identity from Marker Gene Function to Understand Murine Thermoregulatory Circuits

by

Norma P. Sandoval
Doctor of Philosophy in Molecular, Cellular and Integrative Physiology
University of California, Los Angeles, 2026
Professor Stephanie M. Correa, Chair

Estrogen deficiency at menopause is associated with a plethora of symptoms with long-lasting effects on quality of life and health span. These symptoms include decreased energy expenditure that is often accompanied by unpredictable and uncomfortable changes in body temperature known as hot flashes. Hormone therapy can improve metabolic profiles after menopause but can also increase the risk for certain cancers. The overarching goal of my dissertation is to uncover the neuronal and molecular targets of estrogen in the hypothalamus that modulate various aspects of thermoregulation and understand the physiologically relevant contexts in which they function. Ultimately, my research may identify therapeutics that mimic the thermal effects of estrogen while circumventing the negative effects of hormone therapy.

The ventrolateral subdivision of the ventromedial hypothalamic nucleus (VMHvl) modulates aspects of energy expenditure and comprises heterogenous estrogen-sensitive neuronal populations. However, whether its role in energy expenditure arise from the activity of specific neuronal subpopulations or the genes defining them, remains unknown. We previously found that the p53-regulated and estrogen-responsive gene Reprimo (*Rprm*) is expressed within

the VMHvl, shows higher expression in females than males, and increases body temperature when transiently silenced. While this initial work identified a molecular candidate that may regulate body temperature in a sex-specific manner, outstanding questions remained due to the lack of a mouse model allowing us to probe further into the function of this specific cell type.

My dissertation research has aimed to rigorously define the function of the *Rprm*$^{+}$ neuronal population in the VMHvl by discriminating the role of the *Rprm* gene from the actions of *Rprm*$^{+}$ neurons. This is an important distinction to make since the function of a gene does not necessarily equate to the function of the cells that express it. For instance, genes can function in cell non-autonomous ways and neurons express many different genes that coordinate function. To address this, we generated a *Rprm*$^{Cre\text{-}FRT}$ knock-in mouse model that has enabled me to use state-of-the-art viral tools to understand the molecular, cellular, and circuit-level characteristics of this neuronal population. Altogether, this dissertation makes three key contributions to our understanding of the *Rprm*$^{+}$ population in the VMHvl. First, I thoroughly characterized the novel *Rprm*$^{Cre\text{-}FRT}$ mouse line, verifying construct integrity, Cre recombinase activity and function, and gene expression fidelity (Chapter 2). With this model validated, I then took advantage of the Cre-lox system to define the function of *Rprm*$^{+}$ neurons, both by manipulating their activity to determine whether this was sufficient to alter thermoregulation, and by using circuit-mapping viral tools to characterize the anatomical circuitry in which these neurons operate (Chapter 3). Finally, I leveraged the *Rprm*$^{Cre\text{-}FRT}$ mouse model and the Flp-FRT system to permanently ablate *Rprm* expression via two approaches differing in temporal and spatial scale, assessing its necessity for thermoregulation across different physiological contexts (Chapter 4).

The dissertation of Norma P. Sandoval is approved.

Andrea L. Hevener

Arthur P. Arnold

Claudio J. Villanueva

Stephanie M. Correa, Committee Chair

University of California, Los Angeles

2026

To all who believed I could, this is as much yours as it is mine

To the mice, without you this work would not be possible

To my cats, for the infinite emotional support

Table of Contents

ABSTRACT OF THE DISSERTATION ii

Committee iv

Dedication v

ACKNOWLEDGEMENTS viii

VITA xii

Chapter 1: From tumor suppressor to thermoregulator: the role of *Rprm*, the VMH, and the neural basis of novelty responses 1

- The role of *Rprm* as a tumor suppressor 2
- The role of *Rprm* in the mouse brain 3
- The thermoregulatory and behavioral roles of the VMH 4
- The behavioral and physiological responses to novelty 5
- Next steps 6

Chapter 2: Validating a novel mouse model pivotal to establishing the functional role of the $Rprm^{+}$ population in the VMHvl 8

- The need for a mouse model 9
- Designing the $Rprm^{Cre\text{-}FRT}$ mouse line 10
- Sequencing the $Rprm^{Cre\text{-}FRT}$ transgene verifies construct integrity 10
- Validating Cre recombinase expression and functional activity in $Rprm^{Cre\text{-}FRT}$ mice 11
- Validating gene expression fidelity in $Rprm^{Cre\text{-}FRT}$ mice 12
- Scope of this dissertation 14

FIGURES 15

- Figure 2.1: $Rprm^{Cre\text{-}FRT}$ knock-in design 15
- Figure 2.2: Sanger sequencing reveals significant errors in sequence integrity for $Rprm^{Cre\text{-}FRT}$ mouse line 23 16
- Figure 2.3: Sanger sequencing reveals near perfect sequence integrity for $Rprm^{Cre\text{-}FRT}$ mouse line 26 17
- Figure 2.4: *Rprm* lineage tracing reveals robust expression in the brain and peripheral tissues 20
- Figure 2.5: Validating the functionality and fidelity of the $Rprm^{Cre\text{-}FRT}$ transgene 21
- Figure 2.6: Endogenous *Rprm* gene expression is not altered by the knock-in allele in $Rprm^{Cre\text{-}FRT}$ mice 23

MATERIALS AND METHODS 24

Chapter 3: Defining the functional and anatomical outputs of the $VMHvl^{Rprm}$ cell population 30

INTRODUCTION 31

RESULTS 33

DISCUSSION 38

FIGURES 39
Figure 3.1: Activating VMHvl^{Rprm} neurons is sufficient to elicit a sustained hyperthermia in female mice 39
Figure 3.2: Chemogenetic activation of VMHvl^{Rprm} neurons alters the thermoregulatory profile of male mice 41
Figure 3.3: The activity of *Rprm*$^{+}$ neurons in the MBH is not required for the circadian elevations in T_c observed at night 43
Figure 3.4: VMHvl^{Rprm} neurons project to nodes involved in thermoregulation and the processing of social and survival sensory cues 46
Figure 3.5: Neither cold- nor sickness-induced thermogenesis are associated with cFOS immunoreactivity in the VMHvl 48
Figure S3.1 related to Figures 1 and 2: CNO treatment in mice lacking hM3Dq expression does not alter thermoregulation 49
Figure S3.2 related to Figure 3: Optimizing the oral administration of DCZ via voluntary ingestion of peanut butter 51
MATERIALS AND METHODS 52

Chapter 4: Temporally and spatially distinct approaches to knockout *Rprm* expression in the brain reveal context-dependent roles 63
INTRODUCTION 64
RESULTS 65
DISCUSSION 70
FIGURES 74
Figure 4.1: Female mice harboring a *Rprm* KO in *Vglut2*-lineage cells display mild alterations to T_c when housed in standard ambient temperatures (22-23 °C) 74
Figure 4.2: Female mice harboring a *Rprm* KO in *Vglut2*-lineage cells have unaltered T_c when housed at thermoneutrality (29-30 °C) 76
Figure 4.3. Female mice harboring a *Rprm* KO in *Vglut2*-lineage cells have unaltered T_c when exposed to a substantial cold challenge (15 °C) 78
Figure 4.4: Female mice harboring an adult-specific *Rprm* KO in the VMHvl have unaltered T_c at standard ambient temperatures (22-23 °C) 79
..... 80
Figure 4.5: Female mice harboring an adult-specific *Rprm* KO in the VMHvl display an enhanced hyperthermia in response to novel object presentation 81
Figure S4.1 related to Figures 1-5: Schematic of the two approaches used to generate *Rprm* KO mice 82
Figure S4.2 related to Figure 5: Week-long daily habituation is sufficient to reduce T_c spikes for the assessment of stress-induced hyperthermia 83
MATERIALS AND METHODS 84

REFERENCES 91

ACKNOWLEDGEMENTS

To my mentor, Dr. Stephanie Correa, thank you for cultivating a lab environment where we could be our authentic selves, from talking about the latest paper on thermoregulation to Bad Bunny's latest album. Your positive outlook helped us keep going when things got rough: the pandemic, accidents, fires, the instability of academia as we know it, just to name a few. You have been our fearless leader through all of it. Thank you for giving me the freedom to make the Reprimo story my own, even when it took unexpected turns, you let me pursue these crazy questions. In all my writing, you gave me feedback but ultimately always let my scientific voice come through, allowing me to gain confidence in my ideas and ability to articulate them. This freedom helped me become a more confident scientist.

To the Correa lab members, you are not just my colleagues, you became my family. The OG lab members: my dear friend Megan Massa, beyond teaching me the nitty gritty science techniques, you also taught me that my opinion matters and it's ok to speak up and ask questions. To Alexia Josef, you were my first mentee but truly, you mentored me. It was an honor watching you flourish as a scientist and now following along your med school journey.

To Laura, words cannot describe what you have meant to me throughout this journey. My wiser younger sister (even though we both look super young lol). When the science confused me or I was trying to navigate the complexities of career development, you became a mentor to me, someone whom I could go to without fear of judgement. Your ability to remain calm in moments of stress and to always see the cup half full is inspirational. I cannot wait to see the amazing things you will accomplish when you run your own lab, your mentees are beyond lucky to have you!

To Paul, Rachel, and Kelly, the younger siblings I didn't know I wanted lol. It has been an absolute pleasure navigating this crazy and confusing world of academia with you. Paul, I

admire the patience you have even when things are frustrating, you know when to take a step back and that is something I admire. You are meticulous and have such a refined care for your work. Rachel, your ability to recall a zillion details astonishes me. Not only are you a careful scientist, but you are also one of the most committed and passionate mentors I have met. From color-coding protocols, creating a whole (funded) tutorial, and guiding your students through technique and theory, you have genuinely made science more accessible for those who might have quickly been dismissed because they did not have a research background. To both Paul and Rachel, the future of academia looks a lot brighter because you're in it! Kelly, my fellow Slytherin, it has been a true pleasure working with you. From the early days of RNAscope to watching you lead your own project; you are such a badass. You have not had the easiest journey so far, but you carry yourself with such grace and assertiveness. Beyond a colleague, I am grateful to call you a friend. We instantly bonded over our shared perspective on things (some call it being judgy but we're just analytical and opinionated lol). I truly enjoyed our chats on future career goals, and I am so excited to see all you do in industry, and hey, maybe we'll work together again!

To Monay I could write a whole dissertation about you. At a time when I was questioning my place in science, you came and restored my love for the field and for mentorship. Your genuine passion and curiosity inspired me every day. You came in with a smile and ready to learn, and that gave me the energy to push forward. While I couldn't directly work with you during your master's project, I am so unbelievably proud of everything you accomplished. You are one of the best scientists I have ever met; you carry all your work with integrity, honesty, and rigor! These qualities are what will also make you an amazing doctor. I am certain you will positively impact patients' lives and I look forward to following along in your journey. Above all, I am so incredibly grateful to call you, my friend.

Hannah and Monay, our friendship means the world to me. We bonded over the most random pet peeves (and like I mentioned above with Kelly, over our analytical and opinionated character lol) and found a safe space where we could be our authentic selves. Our iPhone sticker collection is elite, and I look forward to getting all the voice notes (and I will respond with my 5-min long rants lol). Hannah, you instantly light up a room when you walk in; your energy is magnetic! You are such a kind and genuine soul, and it is these traits that will make you an incredible professor (at UCLA of course)!

To my parents, you gave up everything you had in El Salvador, your support system, your family, to make sure I had opportunities that were never afforded to you. I cannot express how much I admire your bravery and resilience. This is for you.

To Nathan, Princess, and Cammy, you are my entire world, my reason to keep going. None of this would be possible without your support. There are not enough pages in this universe to describe what you mean to me.

To my doctoral committee, Drs. Andrea Hevener, Art Arnold, and Claudio Villanueva, thank you for your scientific guidance, your flexibility, and your willingness to talk science with me and entertain my crazy theories!

To my collaborators, Drs. Tara Raam, Weizhe Hong, Heidi Schmidt, Thomas Vallim, Shannon Stephens, Alexander Kauffman, and Celine Camon, thank you for entrusting me with your projects. It has been an honor seeing your work positively impact the field.

Chapters 2-4 are adapted from a manuscript that is under revision at Cell Reports:

> **Sandoval, N.P.**, Vranich, K.L., Dilday, E.A., Martinez, R.M., Cortes, L.R., Park, J.W., Vree A.R., Richardson, G., Martignago Cassol, M.F., Kammel, L.G., van Veen J.E., & Correa, S.M. Dissociating Cell Identity from Gene Function Reveals a Role for Reprimo in Novelty-Induced Hyperthermia and Hyperactivity (2026).

I would also like to acknowledge the funding sources that made this work possible. This work was supported by funding from the National Institutes of Health (R01 AG066821, and R01 DK136073 to Dr. Stephanie Correa; R56 AG066821 to Dr. Stephanie Correa and Dr. Ed van Veen), a Pilot and Feasibility Grant and David Geffen School of Medicine Dean's Award to Dr. Stephanie Correa from the UCSD/UCLA Diabetes Research Center (P30 DK063491), a UCLA Core Voucher from the UCLA CTSI (UL1TR001881) to Dr. Stephanie Correa, and a UCLA Brain Research Institute Graduate Student Research Grant to Dr. Laura Kammel. I was supported by a National Science Foundation Graduate Research Fellowship (DGE-2034835), a Ford Foundation Predoctoral Fellowship provided through the National Academies of Sciences, Engineering, and Medicine, a UCLA Graduate Council Diversity Fellowship, and a UCLA Graduate Division Dean's Scholar Award. During the preparation of this work, Claude AI was used to suggest edits for improving the clarity of the text. I reviewed and edited the output as needed and take full responsibility for the content presented here.

Contributions:

I am eternally grateful to all those who contributed to this work through their feedback, ideas, and technical assistance. To Dr. Laura G. Kammel, who started the Reprimo project and generated the *Rprm*$^{Cre\text{-}FRT}$ mouse line, giving me a strong foundation to build upon. To Dr. Ed van Veen, who was incredibly helpful when I joined the lab and taught me stereotaxic surgery. To Kelly L. Vranich, Rosalizbeth M. Martinez, Elizabeth A. Dilday, Jae W. Park, Gabrielle Richardson, Adriana R. Vree, and Maria Fernanda Martignago Cassol, for your contributions in making the experiments outlined here happen. To Higor J. Fideles, for performing critical experiments for a collaboration, which allowed me to complete the experiments in this dissertation. To Dr. Laura R. Cortes for her help performing important revisions on the current manuscript. None of this work would be possible without all your contributions, thank you.

VITA

EDUCATION

Sept 2019 – Present	**University of California, Los Angeles (UCLA):** Doctor of Philosophy Candidate Major: Molecular, Cellular, & Integrative Physiology (MCIP) GPA: 4.0/4.0
Sept 2013 – June 2015	**University of California, Los Angeles (UCLA):** Bachelor of Science, June 2015 Major: Physiological Science *Summa cum laude,* College Honors*,* Regent's Scholar GPA: 3.92/4.0
Aug 2009 – June 2013	**Santa Monica College (SMC):** Associate of Arts, June 2013 Double Major: General Science Liberal Arts, Social and Behavioral Science Highest Honors GPA: 4.0/4.0

FELLOWSHIPS

- The National Academies Ford Foundation Predoctoral Fellowship (2021-2026)
- The National Science Foundation Graduate Research Fellowship (2021-2026)

ACADEMIC AWARDS AND HONORS

- 2026 Jan R. Cloyde Travel Award, 13th International Meeting: Steroids and Nervous System
- 2023 Equity, Diversity, and Inclusion Student Leadership Award, UCLA
- 2022 Best Poster Award, *Hypothalamus Gordon Research Conference*
- 2022 Fan Favorite Poster Award, *Annual Meeting of the Society for Behavioral Neuroendocrinology*
- 2022 Carl Storm Underrepresented Minority Fellowship Award, *Hypothalamus Gordon Research Conference*
- 2022 Travel Award, *Annual Meeting of the Society for Behavioral Neuroendocrinology*
- 2021 Welcome Initiative Award, *the Society for Behavioral Neuroendocrinology*
- 2020 Graduate Council Diversity Fellowship recipient, UCLA
- 2019 Graduate Division Dean's Scholar Award recipient, UCLA

INDUSTRY RESEARCH EXPERIENCE

Translational Neuroscience, Genentech June-Sept 2023

Summer Intern, Principal Investigators: Dr. William Meilandt and Dr. Nikhil Janak Pandya

- *Working in the drug discovery sector, my research employed in vivo and in vitro tools evaluating the molecular interactions between a lipoprotein of interest and the beta-amyloid*

peptide. The goal was to assess the possible therapeutic value of this lipoprotein as a target for the treatment of Late-onset Alzheimer's disease.

ACADEMIC RESEARCH EXPERIENCE

Department of Integrative Biology & Physiology, UCLA July 2020-present
Graduate Student Researcher, Principal Investigator: Dr. Stephanie Correa

- *Elucidating the estrogen-sensitive neuronal populations within the hypothalamus that modulate thermoregulatory and behavioral responses.*

Cardiology Department, David Geffen School of Medicine May 2016-Sept 2019
Research Associate, Principal Investigator: Dr. Stephen Young

- *Investigating the properties and mechanisms of action of a glycosylphosphatidylinositol (GPI)-anchored endothelial cell protein, GPIHBP1, which is required for the processing of triglyceride-rich lipoproteins (TRLs). Participated in groundbreaking research identifying the presence of GPIHBP1 autoantibodies in human patients diagnosed with chylomicronemia, a disorder in which the body fails to break down lipids.*

PUBLICATIONS

Submitted Manuscripts:

1. **Sandoval, N.P.**, Vranich, K.L., Dilday, E.A., Martinez, R.M., Cortes, L.R., Park, J.W., Vree A.R., Richardson, G., Martignago Cassol, M.F., Kammel, L.G., van Veen J.E., & Correa, S.M. Dissociating Cell Identity from Gene Function Reveals a Role for Reprimo in Novelty-Induced Hyperthermia and Hyperactivity (2026). *Under Revision at Cell Reports.*
2. Schmidt, H.M., Srikanth, K., Jin Kim, M., Rubert, G.E., Jarrett, K.E., Do, D.C., Brearley-Sholto, M.C., Chan, A.P., Lai, R., Little, I., Peluso Smith, E., Baltazar-Nuñez, R., Steel, M.E., Cheng, A.S., Taveras, M.O., **Sandoval, N.P.**, Correa, S.M., Turner, M., Sobreira, D.R., Tarling, E.J., & de Aguiar Vallim, T.Q. mRNA Decay Pathways Limit Hepatokine Levels to Control Systemic Metabolism (2025).

Peer-Reviewed Publications (4 out of 16):

1. Cortes, L.R., Reis, F.M.C.V., Vree, A.R., Kim, N., Hansen, M.R., **Sandoval, N.P.**, Rashid, S., Lopez, J., Colwell, C., Van Veen, J.E., He, Y., Adhikari, A., Correa, S.M. Estrogen-responsive neurons modulate thermoregulation in pregnancy. *Proc Natl Acad Sci USA.* 123(39):e2611415123 (2026).
2. Cara, A.L., Guthman, E.M., Mishra, A., Hall, A.L., Yokoyama, S., Azadi, H.N., Gregg, I.P., Martinez, R.M., **Sandoval, N.P.**, Aghi, K., Soma, K.K., Correa, S.M., Falkner, A.L., & van Veen, J.E. A Bifunctional optical reporter for tracking estrogen response dynamics in neurons. *Neuron.* 115, 1-14 (2026).
3. Camon, C., Kip, E., Lord, R., Decourt, C., Prescott, M., Clarkson, J., **Sandoval, N.P.**, Vander, P.B., van Veen, J.E., Prokai-Tatrai, K., Correa, S.M., Campbell, R.E., & Garratt, M. (2026). Targeting Estrogen to the Brain via DHED potentially does not Protect Against Metabolic Dysfunction in Obese, OVX mice. *Endocrinology.* bqag082 (2026).
4. Raam, T., Li, Q., Gu, L., Elagio, G., Lim, K.Y., Taimish, J.Y., Zhang, X., **Sandoval, N.P.**, Correa S.M., & Hong, W. Prefrontal regulation of collective social dynamics during environmental challenge. *Nat Neurosci.* 29, 901–914 (2026).

Chapter 1: From tumor suppressor to thermoregulator: the role of *Rprm*, the VMH, and the neural basis of novelty responses

The role of *Rprm* as a tumor suppressor

Reprimo (*Rprm*) is a p53- and estrogen-responsive gene encoding a 109 amino acid protein whose structure is not clearly defined beyond a putative transmembrane helix (UniProt: Q9JJ72) (The UniProt Consortium et al., 2025). While *Rprm* is expressed in healthy tissues in both humans and rodents, most reports on *Rprm* function have focused on its pathophysiological role in cancerous tissues, emphasizing its tumor-suppressing abilities as a p53 target gene (Ohki et al., 2000; Takikawa and Ohki, 2025). For instance, *Rprm* has been shown to play a critical role in the DNA damage response in mice (Li et al., 2022; Ye et al., 2023; Zhang et al., 2022). Interestingly, *Rprm* deletion has a greater protective effect against radiation-induced hematopoietic injury in male but not female mice (Li et al., 2022), potentially due to the repressive effects of estrogens on *Rprm* (Malik et al., 2010). Further, hypermethylation of the *Rprm* promoter, and the resulting reduction in *Rprm* expression, has been reported in various cancers (Takikawa and Ohki, 2025) including gastric (Amigo et al., 2018; Ooki et al., 2013), pancreatic (Sato et al., 2008, 2003), pituitary (M. Xu et al., 2012), and breast (Buchegger et al., 2017) cancers.

Recent studies have begun elucidating the molecular mechanisms by which *Rprm* exerts its tumor suppressing effects. For instance, both cytoplasmic and nuclear intracellular sites of action have been identified, as well as a recently discovered extracellular role for *Rprm* via its binding to receptors of the protocadherin family (Takikawa et al., 2025; Takikawa and Ohki, 2025). Further, in mouse models of gastric cancer, *Rprm* overexpression suppresses tumor growth via both autocrine and paracrine activity (Ooki et al., 2013; Takikawa and Ohki, 2025). However, while the role of *Rprm* in cancer suppression and its underlying mechanisms of action have been the focus of increasing study, the physiological and context-dependent roles of *Rprm* in healthy tissues have remained largely undefined until recent work from our group.

The role of *Rprm* in the mouse brain

Estrogen-sensitive neurons in the ventrolateral subdivision of the ventromedial hypothalamic nucleus (VMHvl) regulate aspects of metabolism such as glucose homeostasis (He et al., 2020; Routh, 2010; Yoon and Diano, 2021) and two components of energy expenditure, physical activity and thermogenesis (Correa et al., 2015; Krause et al., 2021; Martínez de Morentin et al., 2014; Musatov et al., 2007; Park et al., 2026; van Veen et al., 2020; Xu et al., 2011; Ye et al., 2022), in sex-specific ways. Beyond modulating metabolism, the VMHvl also regulates reproductive and social behaviors (Hashikawa et al., 2017; Oliveira et al., 2025; Silva et al., 2013; Yin et al., 2022), anxiety (Cheung et al., 2015; Mccarthy et al., 1996), and arousal (Devidze et al., 2006; Krause et al., 2021).

Our group previously identified striking expression of *Rprm* within the VMHvl in female mice (van Veen et al., 2020). We further discovered that partial *Rprm* gene knockdown in the VMHvl via short interfering RNA pools (siRNAs) alters energy expenditure by increasing core body temperature (T_c) and brown adipose tissue (BAT) thermogenesis without affecting movement in female mice (van Veen et al., 2020). Knockdown of *Rprm* in males, which express little to no *Rprm* in the VMHvl, does not alter T_c (van Veen et al., 2020).

To gain further insight into the function of this population, we generated a $Rprm^{Cre\text{-}FRT}$ knock-in mouse line (Park et al., 2026) allowing us to leverage the Cre/loxP and Flp/FRT systems. We first used this novel mouse to characterize the *Rprm* lineage by crossing it with a Cre-dependent *Ai14*-mediated reporter. In doing so, we identified robust *Rprm* expression throughout the brain, uterus, ovary, pituitary, and pancreas, all estrogen-sensitive tissues (Park et al., 2026). We further discovered that female mice harboring a knockout of estrogen receptor alpha (*Esr1* encoding ERα) in *Rprm* lineage cells displayed mild alterations in T_c and BAT thermogenesis. Further, caspase-mediated loss of $Rprm^{+}$ cells throughout the mediobasal hypothalamus (MBH) caused a subtle yet sustained decrease in T_c in female mice (Park et al.,

2026). These studies, along with our prior siRNA manipulations, cement the idea that *Rprm*$^{+}$ cells, and the estrogen signaling within them, play important roles in regulating BAT thermogenesis and core body temperature. Interestingly, neither of these manipulations resulted in significant alterations to overall metabolic outcomes, such as body weight or composition. Thus, it is possible that these *Rprm*-mediated alterations to energy expenditure impact physiologies beyond metabolism in females.

The thermoregulatory and behavioral roles of the VMH

While the functions of the VMHvl are often studied independently, they are inextricably linked, offering an opportunity to develop a more integrated understanding of the crosstalk between energy expenditure and behavior. For instance, previous studies have identified neuronal subpopulations within the dorsomedial subdivision of the VMH (VMHdm) that modulate energy expenditure across broader behavioral contexts. Namely, preprodynorphin (*Pdyn*)-expressing cells modulate social interactions and a resulting hyperthermia, in part, by activating BAT thermogenesis (Feng et al., 2022). Further, Cav3.1 expression in the male VMHdm mediates neuronal activity patterns during chronic stress and integrates this information to regulate energy expenditure and anxiety (Shao et al., 2022). Subpopulations defining the broader VMH, not just the VMHdm, have also been implicated in the regulation of anxiety-like behaviors and energy expenditure, such as those defined by expression of vesicular glutamate transporter 2 (*Vglut2*) (Cheung et al., 2015), calmodulin-dependent protein kinase II alpha (CaMKII) (Li et al., 2023), and steroidogenic factor 1 (SF1) (Kunwar et al., 2015; Shao et al., 2023; Silva et al., 2013; Viskaitis et al., 2017; Zhao et al., 2008).

The association between anxiety-like behaviors and T_c elevations is known as stress-induced hyperthermia (SIH) (Adriaan Bouwknecht et al., 2007; Harshaw et al., 2021; McGivern et al., 2009; Nakamura, 2015; Oka, 2018, 2015; Olivier et al., 2003; Veening et al., 2004;

Vinkers et al., 2009a, 2009b; Zethof et al., 1994). One of the most well-defined SIH responses arises from social interactions, which, as we described above, is in part regulated by *Pdyn*$^{+}$ neurons in the VMHdm (Feng et al., 2022). Novelty, whether a new environment or an unfamiliar object, is another environmental stimulus known to elicit an SIH response (Adriaan Bouwknecht et al., 2007; Oka, 2018, 2015). Interestingly, it has been shown that female mice lacking glutamatergic signaling in the VMHvl display heightened novelty-associated changes in locomotion and anxiety-like behaviors (Cheung et al., 2015), potentially contributing to the SIH response. These studies highlight a critical link between the VMH, energy expenditure, and broader behavioral responses that require further study.

The behavioral and physiological responses to novelty

When rodents are exposed to novelty, this may represent a potential threat or a rewarding experience. The adaptive behavioral and physiological responses to novelty reflect this dual nature. Initial exposure often triggers an anxiety-like response known as neophobia, characterized by freezing, avoidance, and hesitant movement. This is then followed by a phase of intense exploration and hyperactivity, known as neophilia, which gradually subsides to basal activity levels as rodents habituate to the novel stimulus (Lustberg et al., 2020). The locomotor response to novelty has been widely reported in rodents and is often used as a tool to assess an animal's predisposition to develop anxiety-, depressive-, or addictive-like behaviors (Cain et al., 2005; Gancarz et al., 2012; Kirschmann et al., 2025; Nyssen et al., 2016; Piazza et al., 1989; Redolat et al., 2009; Shimosato and Watanabe, 2003; Vidal-Infer et al., 2012; White et al., 2007). For instance, it has been shown that rats displaying high novelty-induced locomotor reactivity are prone to elevated risk-taking and addictive behaviors whereas those with damped novelty-induced locomotion are prone to developing anxiety- and depressive-like behaviors after stress (Belin et al., 2011; Calvo et al., 2011; Davis et al., 2008; Dellu et al., 1996; Kirschmann et al., 2025; Piazza et al., 1991; Suto et al., 2001).

The striatal dopamine system modulates the locomotor response to novelty. Rats characterized by heightened novelty-induced locomotion have more spontaneous dopamine release events, elevated dopamine levels within the nucleus accumbens, and lower mRNA expression of the dopamine D2 receptor in the dorsal striatum, than rats with low novelty-induced locomotion (Flagel et al., 2014; Hooks et al., 1994; Kirschmann et al., 2025; Mabrouk et al., 2018; Marinelli and White, 2000). The noradrenergic system is another critical mediator of novelty-induced behavioral outcomes. For instance, damage to the locus coeruleus (LC) norepinephrine (NE) system suppresses behavioral responses to novelty (Archer et al., 1981; Delini-Stula et al., 1984; Harro et al., 1995; Neophytou et al., 2001; Sara et al., 1995; Stone et al., 1999), and mice lacking NE display blunted novelty-induced locomotion (Lustberg et al., 2020). Further, a putative noradrenergic novelty network (NNN), comprised of several nuclei including the LC, bed nuclei of the stria terminalis (BST), and the basolateral amygdalar nuclei (BLA), among others, has recently been identified (Lustberg et al., 2020). Interestingly, many of these regions are downstream targets of estrogen-sensitive VMHvl neurons (Cabrera-Zapata et al., 2026; Krause et al., 2021; Lo et al., 2019).

As discussed previously, the VMHvl is a critical modulator of thermogenesis and physical activity in mice, which have primarily been studied in the context of gross energy metabolism and the resulting effects on body weight and composition. Thus, it will be imperative for future studies to elucidate whether these estrogen-sensitive VMHvl subpopulations, such as those defined by *Rprm* expression, function within the NNN to exert effects at the intersection of energy expenditure, behavior, and affective states.

Next steps

This brief introduction outlines our current understanding of *Rprm* function, from its pathophysiological roles involving DNA damage and cancer, to the VMHvl-specific thermoregulatory role in healthy female mice. Homing in on the VMHvl, we situate this *Rprm*$^{+}$

subpopulation within the greater body of work linking the VMH to energy expenditure, anxiety, and behavior. We further discuss stress-induced hyperthermia and its extension to novelty as a naturalistic stimulus that engages both thermoregulatory and anxiety-related circuits. Despite this knowledge, the function of *Rprm*$^{+}$ neurons in the VMHvl within this broad behavioral and thermoregulatory network remains undefined. The following chapters aim to address these gaps by first characterizing the thermoregulatory role of *Rprm*$^{+}$ neurons within the VMHvl and then defining the specific contribution of *Rprm* gene expression to novelty-induced changes in body temperature and behavior.

Chapter 2: Validating a novel mouse model pivotal to establishing the functional role of the *Rprm*$^{+}$ population in the VMHvl

The need for a mouse model

The p53- and estrogen-responsive gene, Reprimo (*Rprm*), defines a sexually dimorphic subpopulation within the ventromedial hypothalamic nucleus (VMHvl) characterized by robust enrichment in female mice (van Veen et al., 2020). This female- and VMHvl-specific expression pattern led us to hypothesize that the *Rprm*-expressing (*Rprm*$^{+}$) population may function in at least one of the known female-specific roles modulated by the VMHvl, such as sexual behavior (Lee et al., 2014; Oliveira et al., 2025; Yin et al., 2022), aggression (Hashikawa et al., 2017), or energy expenditure (Correa et al., 2015; Krause et al., 2021; Martínez de Morentin et al., 2014; Musatov et al., 2007; Park et al., 2026; van Veen et al., 2020; Xu et al., 2011; Ye et al., 2022), to name a few. To begin deciphering the function of the *Rprm*$^{+}$ population, we first used short interfering RNA pools (siRNAs) injected into the VMHvl to silence gene function and discovered that partial *Rprm* gene knockdown increased brown adipose tissue (BAT) thermogenesis and core body temperature without affecting physical activity (van Veen et al., 2020). While informative for identifying the short-term consequences of destabilizing *Rprm* expression and pointing to a potential role in thermogenesis, this approach led to partial knockdown, precluded analysis of the long-term consequences of gene loss, and failed to fully address the function of *Rprm*$^{+}$ cells, which of course express other genes and signaling molecules. Further, this study did not elucidate the anatomical connectivity nor the physiologically relevant contexts under which *Rprm*-mediated thermogenesis is required. However, at the time, we were limited by the lack of a mouse model permitting *Rprm*-specific manipulations. To address these limitations, we designed and generated a *Rprm*$^{Cre\text{-}FRT}$ mouse line allowing me to leverage the Cre/loxP and Flp/FRT systems to thoroughly characterize the *Rprm*$^{+}$ population at the circuit, cellular, and molecular level, teasing apart the thermoregulatory dynamics of *Rprm*$^{+}$ neurons from the contribution of *Rprm* gene expression. This is an important distinction to make since the function of a gene does not necessarily equate to the function of the cells that express it.

Designing the *Rprm*$^{Cre\text{-}FRT}$ mouse line

We designed our construct using a CRISPR-based approach targeting the genomic locus of the 327 bp single exon *Rprm* gene on murine chromosome 2 as described previously (Kammel, 2019; Park et al., 2026). In brief, the donor construct consisted of a double-stranded DNA repair cassette that included the coding sequence for *Rprm* linked to the codon-improved Cre recombinase (iCre) sequence via a P2A peptide. The P2A peptide was included due to its ability to induce ribosomal skipping, increasing the likelihood that distinct peptide products are generated, in roughly equal amounts, from a single multicistronic construct (J. H. Kim et al., 2011). A 21 bp nuclear localization sequence was placed at the 5′ end of the *iCre* exon to help direct proteins into the nucleus. To induce proper DNA insertion, we also included homology arms (~2000 bp) both upstream and downstream of the *Rprm* and *iCre* coding sequences. Finally, two 34 bp Flippase recognition target (FRT) sites were inserted in the upstream and downstream homology arms within 250 bp of the 5′ and 3′ exons, respectively (**Figure 2.1**).

Once the construct was designed, it was then custom-synthesized and cloned (Genewiz, Inc), for a total length of approximately 8.0 kb. Injection of the CRISPR reagents and donor construct into pronuclear state embryos, and the transfer of viable embryos into foster females, as described previously (Kammel, 2019), was performed by the UCSD Transgenic Core Facility. The resulting pups and their foster mothers were then transferred to UCLA for subsequent model validation.

Sequencing the *Rprm*$^{Cre\text{-}FRT}$ transgene verifies construct integrity

Mouse transgenesis produced 20 pups, out of which two (mouse lines 23 and 26), successfully expressed Cre recombinase, and only one (mouse line 26) expressed both the 5’ and 3’ FRT sites as assessed via PCR and crude genotyping. Proper integration into the correct genomic locus was also successfully validated for line 26 but not line 23 (Kammel, 2019). Next, we used sanger sequencing to assess the entire knock-in cassette for lines 23 and 26. This will

help reveal any potential errors during integration that might be missed with simple PCR. To do so, we designed 9 pairs of overlapping primers using the Benchling software, spanning between the 5' and 3' junctions where the transgene meets the host gene. DNA was amplified via PCR and then extracted and purified for sequencing. Alignment against our theoretical reference sequence revealed significant integration errors in line 23, including mutations in the iCre sequence and a completely missing 3' FRT site, in line with our previous PCR and crude genotyping results (**Figure 2.2A, B**). Line 26 displayed near perfect alignment to our reference sequence, with a single point mutation found in the 3' UTR (**Figure 2.3A, B**). Female mouse 26 was therefore used to propagate the line by breeding with a male C57BL/6J mouse. Heterozygous offspring from this cross were then used to generate a stable homozygous *Rprm*$^{Cre\text{-}FRT}$ mouse line that was used for future experiments (**Figure 2.3C**).

Validating Cre recombinase expression and functional activity in *Rprm*$^{Cre\text{-}FRT}$ mice

Having validated the sequence integrity of our knock-in allele in line 26, we next assessed whether Cre recombinase was functionally active in *Rprm*$^{Cre\text{-}FRT}$ mice. To do so, we first crossed *Rprm*$^{Cre\text{-}FRT}$ mice to a floxed *Ai14* reporter strain to characterize the *Rprm* lineage. This should mark cells that express *Rprm* at any point throughout development with tdTomato fluorescence. We identified Cre-mediated tdTomato fluorescence in the brain, uterus, ovary, pituitary, and pancreas in adult *Rprm*$^{Cre\text{-}FRT}$*/tdTomato*+ female mice (**Figure 2.4A, B**) (Park et al., 2026), in line with evidence from human data demonstrating *Rprm* expression in the brain, female reproductive organs, endocrine tissues, and the gastrointestinal tract, with one difference being that humans express low levels of *Rprm* in the pancreas (The Human Protein Atlas, RPRM protein expression summary; (Uhlén et al., 2015). Specifically, the mouse brain exhibited widespread tdTomato that was most striking in the cortex, in accordance with the pattern of *Rprm* expression detected during early mouse development (**Figure 2.4A**) (Allen Institute for

Brain Science developing mouse brain, ISH data, entrez ID: 67874; (Thompson et al., 2014a). Conversely, tdTomato expression was absent in adipose tissue depots (**Figure 2.4C**).

Since *Ai14*-mediated lineage tracing fails to distinguish developmental versus adult-specific gene expression, marking any cell that has ever expressed *Rprm* and inducing fluorescence throughout the brain, we next specifically assessed Cre recombinase function in adult mice. To do so, we stereotaxically co-delivered two adeno-associated viruses (AAVs) into the VMH, a non-Cre-dependent AAV-GFP that labels the targeted region green, and a Cre-dependent AAV-DIO-mCherry that specifically labels Cre^+ (and by extension, $Rprm^+$) cells red. *Rprm* expression within the VMH of female mice follows a distinctive pattern, with the most prominent expression confined within the estrogen-sensitive ventrolateral subdivision (VMHvl). Thus, if Cre recombinase in our model is functional, we would expect to see pronounced Cre-mediated mCherry fluorescence specifically within the VMHvl. Fluorescent microscopy of the dual AAV injection in $Rprm^{Cre\text{-}FRT}$ mice validated that prediction (**Figure 2.5A**), with green fluorescence labeling the broader VMH, marking the area we targeted stereotaxically, while mCherry fluorescence was largely confined within the VMHvl, marking our $Rprm^+$ population. Thus, while we previously validated the sequence integrity of our transgene, these temporally distinct approaches (the use of a reporter mouse to mark developmental *Rprm* expression and adult-specific stereotaxis with viral constructs) extend those results and confirm Cre recombinase functional activity in the $Rprm^{Cre\text{-}FRT}$ model.

Validating gene expression fidelity in $Rprm^{Cre\text{-}FRT}$ mice

While we validated that the Cre recombinase in our mouse line is functionally active, this does not inform us on the efficiency or specificity of Cre expression. Thus, we next assessed if the $Rprm^{Cre\text{-}FRT}$ transgene results in the stoichiometric expression of *Rprm* and *Cre*, as is expected due to the presence of the P2A peptide in our construct, or whether deviations in expression patterns occur. For instance, the introduction of a transgene can cause off-target Cre

recombinase expression. This would result in a higher proportion of cells that express *Cre* without *Rprm*. This would be a limitation since functionally it would lead us to inadvertently manipulate cells beyond those that express our gene of interest. Another concern arises from a potential failure of ribosomes to continue translation after reaching the P2A peptide. In our model, this would lead to a higher proportion of cells that express *Rprm* without *Cre*. Functionally, this would hinder our ability to fully characterize the *Rprm*$^{+}$ population, as we would be unable to manipulate the subset of *Rprm*$^{+}$ cells that do not express *Cre*.

To assess the expression patterns of *Rprm* and *Cre* in *Rprm*$^{Cre\text{-}FRT}$ mice and determine whether any of these limitations are in effect, we used single-molecule *in situ* hybridization (ISH) to probe for *Cre* and *Rprm* mRNA transcripts in the VMHvl. We found that *Cre* expression faithfully recapitulated and was exclusively restricted to *Rprm*$^{+}$ cells (**Figure 2.5B, C**). Thus, not only is Cre recombinase functionally active in *Rprm*$^{Cre\text{-}FRT}$ mice, but it also accurately and specifically targets *Rprm*$^{+}$ cells.

With the fidelity of *Cre* and *Rprm* expression in the *Rprm*$^{Cre\text{-}FRT}$ mouse validated, we next assessed whether the presence of the transgene itself alters endogenous *Rprm* expression when compared to wildtype C57BL/6J mice. Single-molecule ISH labeling *Rprm* mRNA transcripts did not detect differences in either the intensity of *Rprm* fluorescence (**Figure 2.6A, B**) or the number of *Rprm*$^{+}$ cells (**Figure 2.6C**) between *Rprm*$^{Cre\text{-}FRT}$ and wildtype mice (Park et al., 2026). Thus, the endogenous pattern of *Rprm* expression in *Rprm*$^{Cre\text{-}FRT}$ mice is not affected by the transgene. Furthermore, we characterized the estrogen sensitivity of VMHvl neurons in *Rprm*$^{Cre\text{-}FRT}$ female mice and discovered that approximately 39.5 ± 3.4% of estrogen-sensitive (*Esr1*$^{+}$) cells express *Cre*, and by proxy, *Rprm*, consistent with previous findings in wildtype mice (**Figure 2.5D**) (Park et al., 2026; van Veen et al., 2020). This further verifies that the *Rprm*$^{Cre\text{-}FRT}$ transgene does not affect endogenous gene expression patterns.

Scope of this dissertation

In this chapter, we described the design, generation, and rigorous validation of the *Rprm*$^{Cre\text{-}FRT}$ mouse model, a powerful tool that has allowed me to complete the fundamental goal of this dissertation, to characterize the *Rprm*$^{+}$ population in the VMHvl at the circuit, cellular, and molecular level. Chapter 3 leverages the Cre expression within our model, using chemogenetic and circuit tracing tools to define the thermoregulatory function and anatomical connectivity of the *Rprm*$^{+}$ neurons in the VMHvl, respectively. Chapter 4 takes advantage of the FRT sites flanking *Rprm* to permanently knockout gene expression using two approaches differing in temporal and spatial scale to identify the thermoregulatory contexts in which this population functions. Altogether, these studies establish a framework for understanding how neuronal populations and the genes defining them can have distinct contributions to physiology. As increasingly refined molecular markers are used to define neuronal cell types, distinguishing cellular identity from marker gene function will be essential for understanding how molecular diversity shapes hypothalamic circuits and their function.

FIGURES

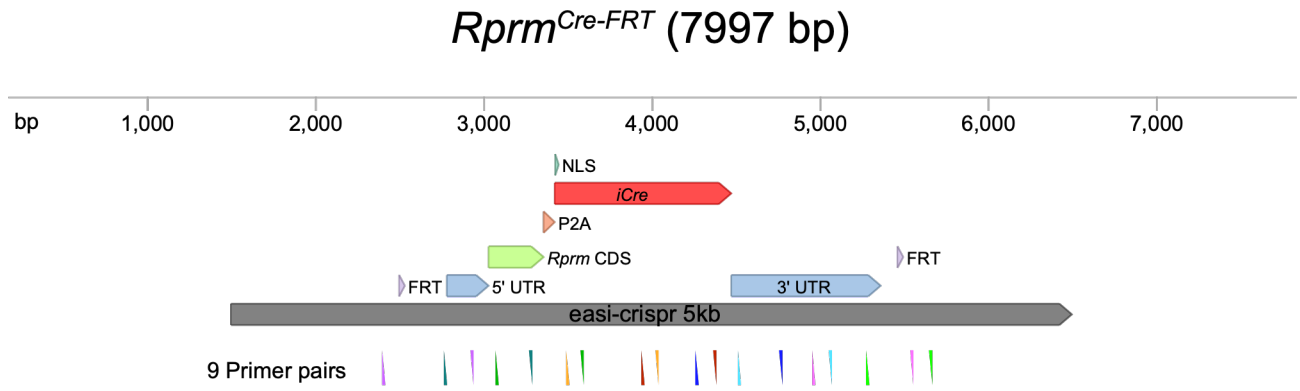


Figure 2.1: *Rprm*$^{Cre\text{-}FRT}$ knock-in design

The 8.0 kb construct consists of homology arms (~2kb in length) found upstream and downstream of the 5' and 3' *Rprm* UTRs, respectively, and contain the 34 bp FRT sites. The 5' UTR is then followed by the 327 bp *Rprm* CDS that is then linked to the 1049 bp iCre sequence via the P2A (66 bp) and NLS (21 bp) sequences. Finally, the 3' UTR is followed by the downstream homology arm. Below the construct diagram, the 9 color-coded primer pairs used to verify the sequence of the entire transgene are depicted, positioned at the location along the sequence where they bind. UTR = untranslated region, CDS = coding DNA sequence, FRT = Flippase recognition target sites, NLS = nuclear localization sequence.

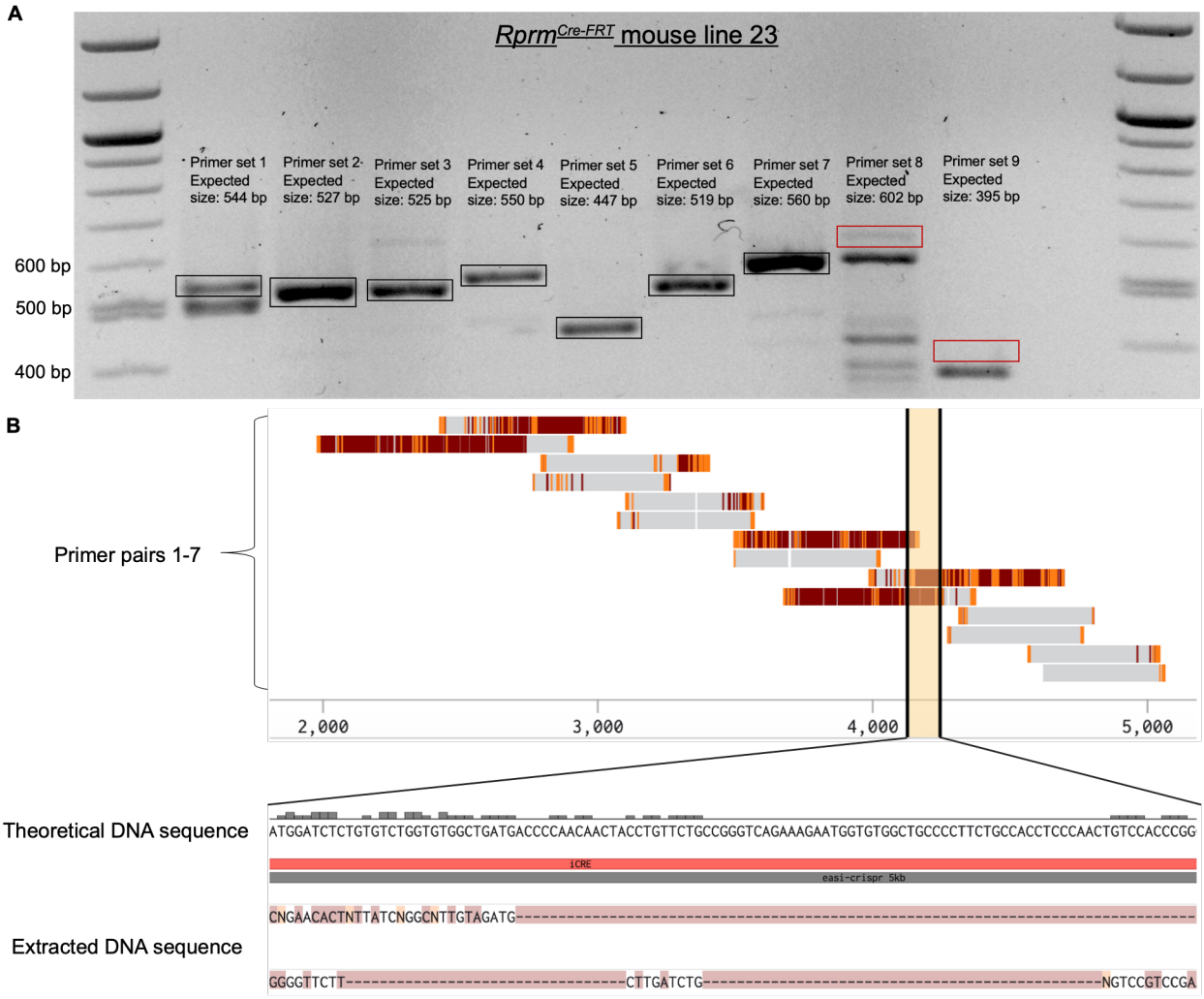


Figure 2.2: Sanger sequencing reveals significant errors in sequence integrity for *Rprm*$^{Cre\text{-}FRT}$ mouse line 23

(A) DNA from line 23 was extracted and selected target regions spanning the entire *Rprm*$^{Cre\text{-}FRT}$ transgene were amplified via 9 different PCR reactions. Only 7 out of 9 reactions yielded the appropriately sized fragments following gel electrophoresis and were therefore excised, purified, and processed for Sanger sequencing. (B) Results from Sanger sequencing aligned to the theoretical sequence via the Benchling software. Highlighted region represents a portion of the iCre sequence with significant errors, expanded below. Alignment success is depicted as follows: Grey = perfect alignment, red = mismatches, orange = low-confidence uncalled bases.

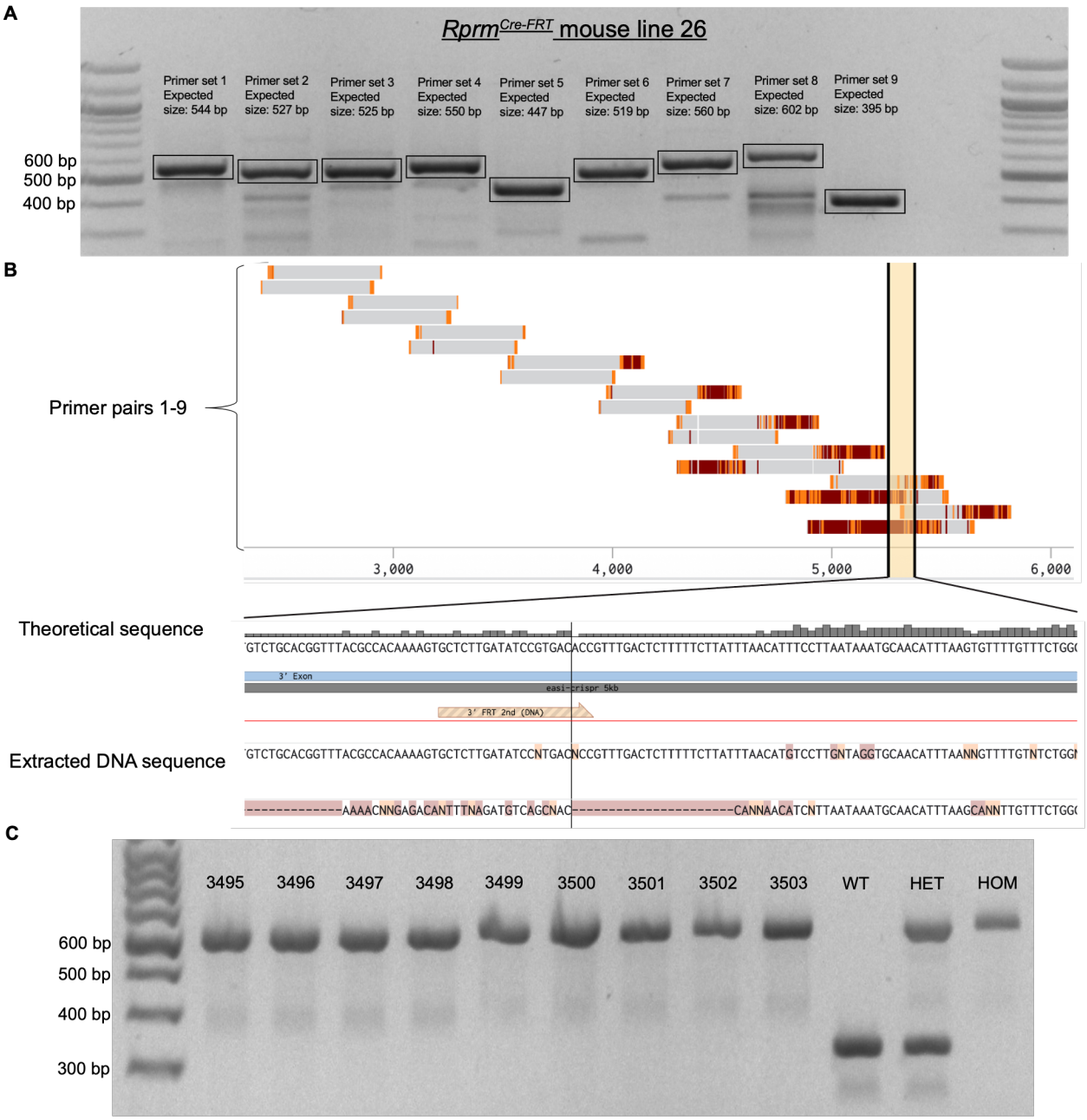


Figure 2.3: Sanger sequencing reveals near perfect sequence integrity for *Rprm*$^{Cre\text{-}FRT}$ mouse line 26

(A) DNA from line 26 was extracted and selected target regions spanning the entire *Rprm*$^{Cre\text{-}FRT}$ transgene were amplified via 9 different PCR reactions. All 9 reactions yielded the appropriately sized fragments following gel electrophoresis and were therefore excised, purified, and processed for Sanger sequencing. (B) Results from Sanger sequencing aligned to the

theoretical sequence via the Benchling software. Highlighted region represents a portion of the 3’ UTR where a single point mutation was detected. Alignment success is depicted as follows: Grey = perfect alignment, red = mismatches, orange = low-confidence uncalled bases.

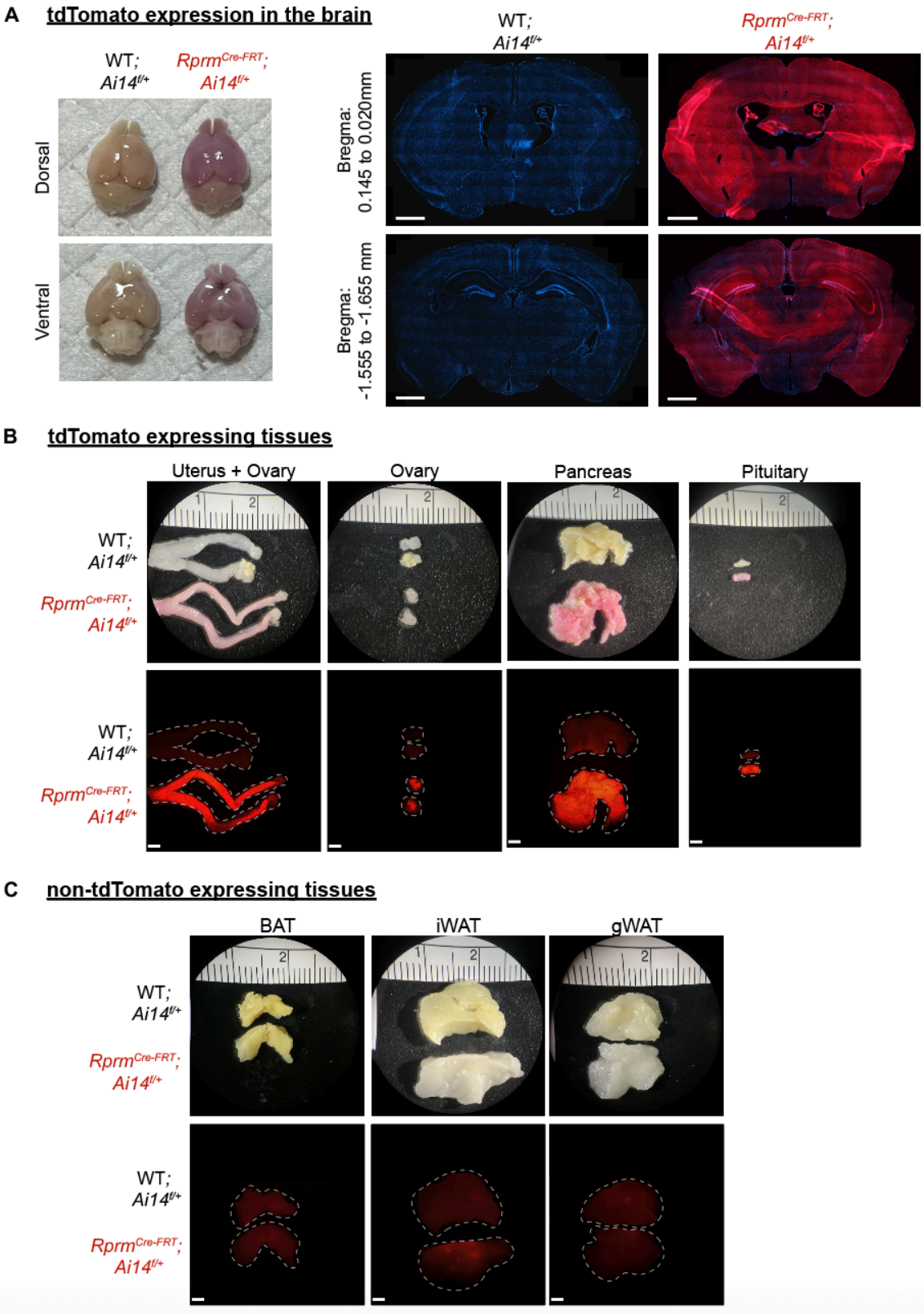

A
tdTomato expression in the brain
WT; Ai14f/+
Rprm Cre-FRT; Ai14f/+
Dorsal
Ventral
Bregma: 0.145 to 0.020mm
Bregma: -1.555 to -1.655 mm
B
tdTomato expressing tissues
Uterus + Ovary
Ovary
Pancreas
Pituitary
C
non-tdTomato expressing tissues
BAT
iWAT
gWAT

Figure 2.4: *Rprm* lineage tracing reveals robust expression in the brain and peripheral tissues

Heterozygous *Rprm*$^{Cre\text{-}FRT}$ mice were bred with *Ai14*$^{f/f}$ mice to produce *Rprm*$^{Cre\text{-}FRT}$*; Ai14*$^{f/+}$ mice expressing tdTomato in *Rprm* lineage tissues. Cre-negative littermates (WT*; Ai14*$^{f/+}$ *mice*) were used to establish baseline tdTomato levels. (A-C) Representative images of tissues harvested from adult (13-15 weeks old) *Rprm*$^{Cre\text{-}FRT}$*; Ai14*$^{f/+}$ and WT*; Ai14*$^{f/+}$ mice. (A) Left, images highlighting tdTomato expression throughout the whole brain in male mice. Right, 30 μm DAPI-stained coronal brain sections emphasize the expression of tdTomato in the cortex, thalamus, and hypothalamus across representative bregma levels. Scale bars = 1 mm. (B) Peripheral tissues exhibiting tdTomato expression include the uterus, ovary, pancreas, and pituitary in female mice. (C) Peripheral tissues that do not express tdTomato include adipose tissue depots (BAT, iWAT, and gWAT) in female mice. Brightfield images displayed on top, fluorescent images below. Scale bars = 200 μm. BAT = brown adipose tissue, iWAT = inguinal white adipose tissue, gWAT = gonadal white adipose tissue.

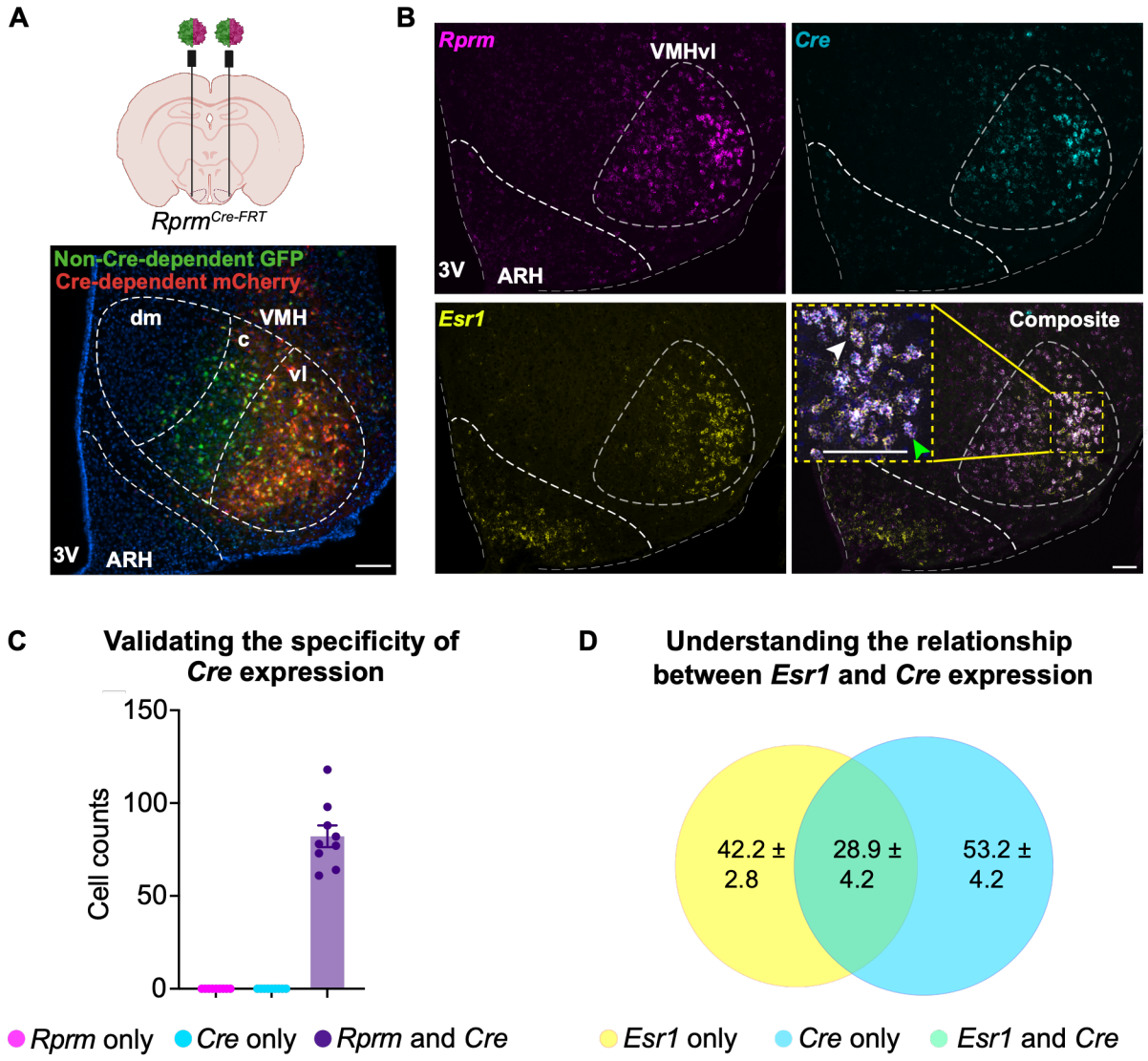


Figure 2.5: Validating the functionality and fidelity of the *Rprm*$^{Cre\text{-}FRT}$ transgene

(A) Top, schematic of stereotaxic AAV delivery into the VMH of *Rprm*$^{Cre\text{-}FRT}$ mice. Bottom, representative image of Cre-dependent mCherry (red) and non-Cre-dependent GFP (green) fluorescence in the VMH of a co-injected *Rprm*$^{Cre\text{-}FRT}$ female mouse; scale bar = 100 μm. (B) Representative images following single molecule *in situ* hybridization labeling *Rprm* (magenta), *Cre* (Cyan), and *Esr1* (yellow) in *Rprm*$^{Cre\text{-}FRT}$ female mice; scale bars = 100 μm. Inset shows a zoomed-in image of the VMHvl, with a white arrow pointing to a cell expressing *Rprm, Cre,* and *Esr1*, and a green arrow pointing to a cell expressing *Rprm* and *Cre*, but no *Esr1*. (C)

Quantification of the number of cells expressing *Rprm* alone (magenta), *Cre* alone (Cyan), and both *Rprm* and *Cre* (purple) in the VMHvl (*n* = 9) with the mean ± SEM and data points for each mouse shown. In all 9 mice, *Cre* expression was exclusively restricted to *Rprm*$^{+}$ cells. (D) Average number of cells expressing *Esr1* alone (yellow), *Cre* alone (Cyan), and both *Esr1* and *Cre* (green) in the VMHvl are depicted (*n* = 9). VMH = ventromedial nucleus of the hypothalamus; dm = dorsomedial, c = central, & vl = ventrolateral subdivisions, ARH = arcuate nucleus, 3V = third ventricle.

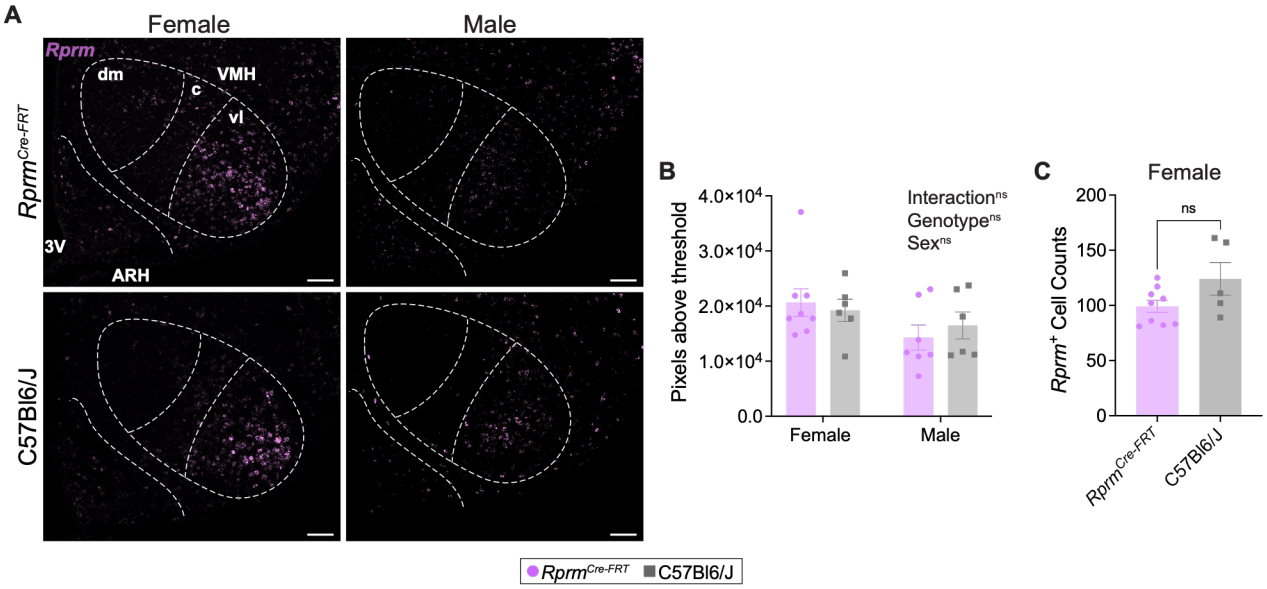


Figure 2.6: Endogenous *Rprm* gene expression is not altered by the knock-in allele in *Rprm*$^{Cre\text{-}FRT}$ mice

(A) Representative images following single molecule *in situ* hybridization labeling *Rprm* (lavender) in *Rprm*$^{Cre\text{-}FRT}$ (top) and C57Bl6/J wildtype (bottom) female (left) and male (right) mice; scale bars = 100 μm. (B) Quantification of *Rprm* signal intensity within the VMH and ARH in 20 μm coronal sections from *Rprm*$^{Cre\text{-}FRT}$ (lavender circles, *n* = 7-8) and C57Bl6/J wildtype (gray squares, *n* = 6) mice. Statistical analysis was performed using an ordinary two-way ANOVA with the mean ± SEM and data points for each mouse shown. (C) Quantification of *Rprm*$^{+}$ cells in the VMHvl of female *Rprm*$^{Cre\text{-}FRT}$ (*n* = 9) and C57Bl6/J wildtype (*n* = 5) mice. Statistical analysis was performed using an unpaired *t*-test; ns = not significant. VMH = ventromedial nucleus of the hypothalamus; dm = dorsomedial, c = central, & vl = ventrolateral subdivisions, ARH = arcuate nucleus, 3V = third ventricle.

MATERIALS AND METHODS

Mouse models

All procedures were approved by the UCLA Institutional Care and Use Committee (IACUC) in accordance with the National Institutes of Health (NIH) guide for the care and use of laboratory animals and carried out in approved facilities at UCLA. Mice were housed under a 12:12 light-dark cycle (zeitgeber time (ZT) 0 = 7:00 am) under controlled humidity conditions at 22-23 °C ambient temperatures with *ad libitum* access to water and breeder chow (Mouse Diet 9F 5020, 20% protein, 9% fat, LabDiet; St. Louis, MO, USA).

Experiments were performed on gonadally intact adult animals. The sex of a mouse was determined at weaning based on anogenital distance and confirmed postmortem based on the presence of ovaries or testes (Massa et al., 2023). *Rprm*$^{Cre\text{-}FRT}$ founder mice on a C57BL/6J background were generated by the University of California San Diego Transgenic & CRISPR Mouse Core and later bred and maintained in approved conditions at UCLA (Park et al., 2026). The homozygous *Rprm*$^{Cre\text{-}FRT}$ line were maintained using in-crosses. For lineage experiments, *Rprm*$^{Cre\text{-}FRT}$ mice were paired with *Ai14*$^{f/f}$ reporter mice (Jax catalog #007914) (Madisen et al., 2010) to generate offspring that fluoresce tdTomato in tissues expressing *Rprm* (*Rprm*$^{Cre\text{-}FRT}$*; Ai14*$^{f/+}$).

Stereotaxic surgery

Surgeries were performed on adult (10 months of age) *Rprm*$^{Cre\text{-}FRT}$ female mice. Following anesthetization, mice were placed on a stereotaxic device (Kopf Instruments model 1900) with isoflurane maintained at 2-2.5%. Viruses were targeted to the VMHvl of adult mice using the following coordinates: 1.56 mm posterior to bregma, 0.85 mm lateral to the midline, and 5.60 mm below the brain surface. Viruses were delivered at a rate of 5-10 nL/sec using

pulled glass needles connected to Hamilton syringes. The needle was slowly removed from the brain 10 min after infusion to allow for viral diffusion. Viruses were delivered bilaterally into the VMHvl. The Cre-dependent AAV8-hSyn-DIO-hM3D(Gq)-mCherry (Addgene #44361-AAV8) and non-Cre-dependent AAV8-hSyn-EGFP (Addgene #50465-AAV8) were mixed in a 1:1 ratio and a total volume of 500 nL per side was delivered. Mice were administered pain management medications, including buprenorphine (0.01 mg/mL) and carprofen (0.58 mg/mL), on the day of surgery and the following day. Daily body weight and health monitoring was conducted for at least a week after surgery.

Sanger Sequencing

DNA was extracted from ear biopsies using an NaOH-based extraction method (Truett et al., 2000). The Q5 High-Fidelity DNA Polymerase was used for the PCR screen (NEB #M0491) following manufacturer instructions. The following primer pairs were designed for sequencing across the *Rprm*$^{Cre\text{-}FRT}$ transgene:

5' FRT
F: 5'-CCTGTCCACCTTACATCTGC-3'
R: 5'-GCGCTGGCTTGATCACTTG-3'
5' UTR
F: 5'-CAAGTTCCAAGAGCTCCCAG-3'
R: 5'-CATGCCTTCGGACTTGATGAG-3'
Rprm CDS
F: 5'-GTTCCTGGTCAACAGTAGCG-3'
R: 5'-GATCTGCACACAGACAGGAG-3'
iCre first half
F: 5'-GGATGCCACCTCTGATGAAG-3'
R: 5'-CCTGCCAATGTGGATCAGC-3'
iCre second half
F: 5'-CATTGCCTACAACACCCTGC-3'

R: 5’-CCACCAGCCTGCATGATTTC-3’

3’ UTR

F: 5’-CTATGGTGCCAAGGATGACTC-3’

R: 5’-CCTGGTTCATCTCCCAGTATC-3’

3’ UTR second half

F: 5’-CTTCTGGCACCTCCAGTAC-3’

R: 5’-CAAACAGGCCACTAGGACAC-3’

3’ FRT

F: 5’-GCGACCTACTAAGAGAGTG-3’

R: 5’-CAAATCCCTGGGCTCTCTG-3’

3’ FRT second half

F: 5’-GCTCTTGATATCCGTGACACC-3’

R: 5’-CGAGAACCTACCTGACATTCG-3’

Sanger sequencing results were then compared to the theoretical sequence via alignment using the Benchling software.

Genotyping

DNA was extracted from ear biopsies using an NaOH-based extraction method (Truett et al., 2000). The Apex Taq Red Master Mix (Genesee Scientific #42-137) was used for PCR, with amplification achieved using a touchdown PCR strategy (van Veen et al., 2020). The following primers were designed for genotyping *Rprm*$^{Cre\text{-}FRT}$ mice:

F: 5’-CTTCTTCCTTGGCTGCAACCTG-3’

R: 5’-CTCTCTCCCCAGCATCCACATT-3’

WTR: 5’-TCCTGTACAGTCTTGCTTGGGG-3’

Tissue collection and preparation

Mice were deeply anesthetized with IP injection of sodium pentobarbital (15 mg/mL) and confirmed unconscious before proceeding. Mice were transcardially perfused with ice-cold DEPC-treated 1x phosphate-buffered saline (PBS, pH=7.4) until the lungs and liver cleared,

followed by ice-cold 4% paraformaldehyde (PFA) diluted from a 16% stock solution (Electron Microscopy Sciences, Catalog# 15700) in DEPC-treated PBS. Brains were harvested, post-fixed in 4% PFA overnight, and dehydrated in 30% sucrose for 24-48 hours, maintaining RNase-free conditions throughout. Brains were then embedded in optimal cutting temperature (OCT) compound (Fisher Scientific, Catalog# 23-730-571) and stored at –80 °C until cryosectioned. Coronal sections at a thickness of 20-30 μm were collected in 4-8 series using a cryostat (Leica CM1950) and either directly mounted on slides or collected free-floating in PBS and kept in Eppendorf tubes filled with cryoprotectant solution (30% sucrose, 30% ethylene glycol, 1% polyvinylpyrrolidone in 1x PBS) stored at –20 °C until further processing.

Histology

4',6-diamidino-2-phenylindole (DAPI) stain

Validation of stereotaxic targeting was carried out by visualization of mCherry and GFP reporter expression and a DAPI counterstain. Briefly, slide-mounted sections were brought to room temperature, or sections were mounted on slides if stored free-floating, and allowed to fully dry before proceeding. Slides were then rinsed with PBS and incubated with DAPI (1:500-1,000, Thermo Fisher Scientific, Invitrogen™ Catalog# D1306) for 5-15 min. Following 2 quick PBS rinses to wash off excess solution, slides were coverslipped with Fluoromount-G™ mounting medium (Thermo Fisher Scientific, Invitrogen™ Catalog# 00-4958-02), allowed to dry, and stored at 4 °C until imaged. Slides were imaged at 4-10x magnification using a Nikon Eclipse Ti2 inverted microscope.

Fluorescent in situ hybridization

To detect the presence of mRNA transcripts in the brain, coronal sections (20 μm in thickness) were first mounted on Superfrost™ Plus slides (Fisher Scientific, Catalog #12-550-15) using RNase-free technique. Slides were allowed to dry and single molecule *in situ*

hybridization was performed using the RNAscope® Multiplex Fluorescent Detection Kit version 2 (Advanced Cell Diagnostics, Newark, CA, USA) following manufacturer instructions. In brief, slides were fixed in prechilled 10% neutral buffered formalin for 20 min at 4 °C. Slides were then pre-treated with serial ethanol dehydration, hydrogen peroxide incubation, target retrieval using a food-grade steamer (Hamilton Beach Brands Inc, Glen Allen, VA, USA) heated to 99 °C, and protease III incubation (Park et al., 2026). Following pre-treatment steps, slides were incubated with commercially available probes from Bio-Techne targeting *Rprm* (catalog# 466071), *Cre* (catalog# 1058921), and *Esr1* (catalog# 478201) at 40 °C for 2 hours. Signal amplification and fluorescent labeling were carried out using the provided solutions along with fluorophores such as Opal 570 (1:500, Akoya Biosciences, Catalog# NEL744001KT) and Opal 690 (1:500, Akoya Biosciences, Catalog# NEL745001KT). Slides were then counterstained with DAPI, coverslipped using Prolong™ Gold Antifade Mountant (Thermo Fisher Scientific, Catalog# P36930), cured overnight at room temperature, and stored at 4 °C until imaged and analyzed as described below.

QUANTIFICATION AND STATISTICAL ANALYSIS

Image Analysis and Quantification

Peripheral tissues were illuminated using a Leica MZ10F and imaged using a dual MP camera system on an iPhone 13. Brain sections were imaged at 10x magnification using a Nikon Eclipse Ti2 inverted microscope, with images imported into ImageJ (Fiji version 2.1.0/1.53c, NIH). Prior to quantification, sections from comparable bregma distances were selected to ensure a similar rostro-caudal level was analyzed for all mice in each experiment, ranging from bregma -1.455 to -1.755 mm, which we considered the central to caudal VMHvl. Regions of interest (ROIs) and anatomical notations were defined and outlined by referencing the Allen Brain Mouse (v2, 2011) and Paxinos and Franklin (v3, 2008) atlases. Cells were

identified based on co-localization of the fluorescent signal with DAPI. Once images were selected, quantifications were performed manually by a blinded investigator as follows.

Fluorescent in situ hybridization

A cell was considered positive for a gene of interest following *in situ* hybridization if it contained 7 or more transcripts within a DAPI-positive cell (Park et al., 2026), using the cell counter plug-in in ImageJ to track positive cells. When needed, brightness/contrast was adjusted uniformly across images. Area-proportional Venn diagrams, generated using BioVenn (Hulsen et al., 2008), show the mean number of cells expressing *Esr1* only, *Cre* only, or *Esr1* and *Cre* in each brain region. To estimate the proportion of the $Esr1^+$ population that expresses *Cre* (and therefore *Rprm*), the number of $Esr1^+/Cre^+$ cells was divided by the total number of $Esr1^+$ cells ($Esr1^+/Cre^+$ and $Esr1^+/Cre^-$) and multiplied by 100 to obtain a percentage. This proportion was calculated per animal, averaged across the group, and described in the text as an average ± SEM. For the comparison of *Rprm* expression in $Rprm^{Cre\text{-}FRT}$ and C57Bl6/J wildtype mice, *Rprm* signal intensity following *in situ* hybridization was determined using the 'thresholding' function in ImageJ to identify positive cells, along with the 'measure' plug-in to calculate the number pixels above threshold for a given ROI.

Statistical Analysis

Statistical analyses and plots were generated in GraphPad Prism (version 11.0.2). Information on statistical tests used, sample sizes, and significance levels are reported in the figure legends. Comparisons between two groups were tested using unpaired *t*-tests. Comparisons involving multiple factors were conducted via 2-way analyses of variance (ANOVA). All statistical analyses were two-tailed. Data were considered statistically significant when p is less than 0.05.

Chapter 3: Defining the functional and anatomical outputs of the VMHvl^{Rprm} cell population

INTRODUCTION

The ventromedial nucleus of the hypothalamus (VMH) regulates a variety of sex-specific physiologies that range from mating and social behaviors to aspects of metabolism (Kammel and Correa, 2020; Khodai and Luckman, 2021; Krause and Ingraham, 2017). The diversity in VMH functional output may be due to the presence of phenotypically distinct cell populations defined by unique gene expression patterns. For instance, the ventrolateral subdivision of the VMH (VMHvl) in female mice is characterized by rich expression of estrogen receptor alpha (*Esr1* encoding ERα) and is comprised of heterogeneous subpopulations. Studies have elucidated the identity of various ERα$^+$ VMHvl subpopulations involved in the regulation of social and reproductive behaviors. Namely, cholecystokinin A receptor (*Cckar*)-expressing neurons are key regulators of sexual behavior in female (Yin et al., 2022) but not male (X. Xu et al., 2012; Yang et al., 2013) mice. Further, the neuronal nitric oxide synthase (*nNOS*)-expressing population is important for aggression and mate choice in males as well as sexual behavior and social motivation in females (Oliveira et al., 2025). Beyond controlling reproductive and social behaviors, estrogen-sensitive VMHvl neurons are well-known metabolic modulators, regulating two components of energy expenditure, physical activity and thermogenesis in sex-specific ways (Correa et al., 2015; Krause et al., 2021; Martínez de Morentin et al., 2014; Musatov et al., 2007; Park et al., 2026; van Veen et al., 2020; Xu et al., 2011; Ye et al., 2022).

We previously discovered that the p53-regulated gene, Reprimo (*Rprm*), defines another subpopulation of ERα$^+$ neurons in the VMHvl, showing higher expression in females than males, and increasing body temperature when *Rprm* expression is transiently silenced. While these findings identified a potential role for the *Rprm* gene in thermogenesis, the function of a gene does not directly inform us about the function of the cells that express that gene, which likely coordinate their output via the actions of multiple genes.

To better define the functions specifically coordinated by *Rprm*$^{+}$ cells in the VMHvl (referred to as the VMHvl^{Rprm} population), we first used our newly validated *Rprm*$^{Cre\text{-}FRT}$ mouse model to determine whether these neurons are required for thermogenesis. Using a caspase-mediated we approach, we showed that ablation of this population leads to a subtle yet sustained decrease in core body temperature (T_c) in female mice (Park et al., 2026). While this indicates that VMHvl^{Rprm} neurons are required, to some extent, to maintain baseline T_c, this manipulation results in cell death and therefore does not elaborate on the functional output of active living cells.

In the current study, we characterize the VMHvl^{Rprm} population at the cellular and circuit levels by using chemogenetic and circuit-tracing approaches, combined with our *Rprm*$^{Cre\text{-}FRT}$ mouse model, to define the thermoregulatory function and anatomical connectivity, respectively, of VMHvl^{Rprm} neurons. At the cellular level, we find that activating VMHvl^{Rprm} neurons is sufficient to elicit a sustained hyperthermia in male and female mice. Further, these body temperature changes are driven by alterations to heat generating effectors such as BAT thermogenesis and gross motor activity as well as heat retaining effectors like tail skin vasoconstriction. However, VMHvl^{Rprm} neuronal activity is not required for circadian elevations in T_c.

Analysis of the downstream projection targets of VMHvl^{Rprm} neurons identified fibers in the thermoregulatory preoptic area (POA) and amygdalar nodes involved in relying sensory information with social and/or survival relevance. When investigating potential physiological contexts in which VMHvl^{Rprm} neurons may function, analyses of cFOS immunoreactivity did not detect VMHvl involvement during cold- and LPS-mediated thermal challenges. These findings add to the body of literature on the known physiologies controlled by the estrogen-sensitive VMHvl. We show that VMHvl^{Rprm} neurons not only modulate BAT thermogenesis in relation to energy expenditure, as we have previously shown via siRNA-mediated *Rprm* gene knockdown, but are a critical component of the larger thermoregulatory system with an ability to alter gross

motor activity and tail skin blood flow to ultimately modulate T_c, further emphasizing the importance of distinguishing between cellular and gene functions.

RESULTS

Activating VMHvl^{Rprm} neurons is sufficient to elicit a sustained hyperthermia

To assess the thermoregulatory capacity of VMHvl^{Rprm} neurons, we chemogenetically activated them using a Cre-dependent hM3Dq (Armbruster et al., 2007) delivered to the VMHvl of *Rprm*$^{Cre\text{-}FRT}$ female mice along with the selective chemogenetic ligand clozapine-n-oxide (CNO) administered in a randomized and counterbalanced design (**Figure 3.1A, B**). Control mice received stereotaxic injection of a Cre-dependent AAV expressing the enhanced green fluorescent protein (EGFP). CNO administration in hM3Dq-expressing mice led to a pronounced increase in T_c persisting approximately 6 hours compared with vehicle treatment (treatment x time interaction: $F(132, 792) = 27.68$, $p < 0.0001$; **Figure 3.1C**), which was not observed in EGFP-expressing controls (**Figure S3.1A**). hM3Dq-expressing mice showed a greater T_c change (Δ) from baseline after CNO (1.43 °C ± 0.13 °C SEM) than after vehicle (-0.14 °C ± 0.05 °C SEM), while EGFP-expressing controls did not differ (treatment x group interaction: $F(1, 9) = 141.5$, $p < 0.0001$; **Figure 3.1G**).

We next sought to tease apart the contribution of thermoregulatory effectors to this hyperthermic state, so we compared the temperature above BAT (T_{BAT}), gross motor activity (GMA), and the temperature of the tail skin (T_{tail}), with the first two serving as proxies for thermogenesis and the last for heat dissipation. CNO administration in hM3Dq-expressing mice led to a robust 6-hour long increase in T_{BAT} compared with vehicle (treatment x time interaction: $F(132, 792) = 21.22$, $p < 0.0001$; **Figure 3.1D**). CNO induced a greater ΔT_{BAT} (1.55 °C ± 0.15 °C SEM) than vehicle treatment (-0.06 °C ± 0.05°C SEM) in hM3Dq-expressing mice but not controls (treatment x group interaction: $F(1, 9) = 74.97$, $p < 0.0001$; **Figure 3.1H**). Lastly, chemogenetic activation of VMHvl^{Rprm} neurons also induced a pronounced increase in GMA

(treatment x time interaction: F (132, 792) = 5.993, $p < 0.0001$; **Figure 3.1E, I**) and a sharp reduction in T_{tail} (treatment x time interaction: F (132, 792) = 4.423, $p < 0.0001$; **Figure 3.1F, J**) persisting for up to 3 hours. In contrast, CNO administration in control female mice did not affect T_{BAT} (**Figure S3.1B**), GMA (**Figure S3.1C**) nor T_{tail} (**Figure S3.1D**).

As in females, activation of VMHvl^{Rprm} neurons in males (**Figure 3.2A, B**) induced higher T_c (treatment x time interaction: F (132, 656) = 8.278, $p < 0.0001$; **Figure 3.2C, H**), GMA (treatment x time interaction: F (132, 656) = 2.870, $p < 0.0001$; **Figure 3.2D, I**), lower T_{tail} (treatment x time interaction: F (132, 620) = 1.918, $p < 0.0001$; **Figure 3.2E, J**) and higher T_{BAT} ($t_{11} = 4.096$, $p = 0.0018$; **Figure 3.2F, G**). CNO did not alter the thermoregulatory profile of control male mice (**Figure S3.1E-G**). Further, we observed indistinguishable patterns of Cre-mediated mCherry fluorescence in the VMHvl between females and males, indicating similar hM3Dq expression (**Figure S3.1H**). Thus, chemogenetic activation of VMHvl^{Rprm} neurons elicits a robust hyperthermic state by altering heat generating and dissipating effectors in both males and females.

The activity of *Rprm*$^{+}$ neurons is not required for circadian T_c elevations in female mice

One of the hallmark characteristics of T_c is its rhythmicity, the most pronounced and well-defined being that which coincides with circadian light/dark rhythms resulting from the interplay between the circadian and thermoregulatory systems (Refinetti, 2020). In this context, T_c follows a predictable pattern whereby it is lowest during the inactive light cycle and rises shortly after lights off when mice are active (**Figure 3.3A**). Given that VMHvl^{Rprm} neurons can elicit pronounced temperature elevations upon chemogenetic activation, we wondered whether the activity of these neurons is necessary for nocturnal elevations in T_c. To answer this question, we chemogenetically inhibited VMHvl^{Rprm} neurons using a Cre-dependent hM4Di delivered to the VMHvl of *Rprm*$^{Cre\text{-}FRT}$ female mice (**Figure 3.3B**). mCherry fluorescence was identified throughout the mediobasal hypothalamus (MBH), indicating that cells within this broader region

were inhibited, rather than those specific to the VMHvl (**Figure 3.3C**). To minimize the effects of handling stress on T_c, the chemogenetic ligand deschloroclozapine (DCZ) was administered orally via peanut butter at a final concentration of 0.5 mg/kg, which we previously validated in hM3Dq-expressing mice (**Figure S3.2A, B**).

Inhibiting *Rprm*$^+$ neurons in the MBH (MBH^{Rprm} neurons) during lights off (ZT 12) did not affect T_c (treatment x time interaction: F (95, 475) = 0.4714, $p > 0.9999$; **Figure 3.3D**) or ΔT_c (group x treatment interaction: F (1, 11) = 4.474, $p = 0.0581$; **Figure 3.3E)**. We next sought to determine whether any potential hM4Di-mediated T_c effects were dependent on the estrous cycle and therefore went undetected when cycle stage was not accounted for. Analysis of T_c across the 4 estrous cycle stages in hM4Di-expressing mice revealed similar ΔT_c values regardless of cycle stage (treatment x cycle stage interaction: F (3, 7) = 3.323, $p = 0.0864$; **Figure 3.3F**). Thus, irrespective of cycle stage, chemogenetic inhibition of MBH^{Rprm} neurons via DCZ administration fails to alter nocturnal T_c elevations.

Given that chemogenetic inhibition via the oral administration of 0.5 mg/kg DCZ did not induce thermogenic changes, it was possible that this dose and route of administration was insufficient to fully induce neuronal inhibition. To address this concern, mice were also treated via IP injections of CNO at a concentration of 3 mg/kg, a well-established dose known to efficiently induce neuronal inhibition of VMHvl neurons (Feng et al., 2022; Silva et al., 2013; Ye et al., 2022). IP injection of 3 mg/kg CNO failed to alter T_c in hM4Di-expressing mice, inducing comparable ΔT_c values to control mice treated with either CNO or vehicle (group x treatment interaction: F (1, 6) = 0.3701, $p = 0.5653$; **Figure 3.3G**). Thus, chemogenetic inhibition of MBH^{Rprm} neurons, tested via two different administration routes, does not affect nocturnal T_c, indicating that the neuronal activity of this population is not required for circadian T_c elevations.

VMHvl^{Rprm} neurons project across nodes involved in thermoregulation and the processing of social and survival sensory cues

Given the capacity of VMHvl^{Rprm} neuronal activity to modulate T_c, we next defined the anatomical connectivity of this population to elucidate function and context based on circuit structure. We used an anterograde tracing approach to label *Rprm*$^+$ fibers emanating from the VMHvl (Fenno et al., 2020; Fermani et al., 2025; Root et al., 2020) (**Figure 2A, B**). Consistent with projections from the broader VMHvl^{Esr1} population (Hashikawa et al., 2017; Krause et al., 2021; Lo et al., 2019; Wang et al., 2019; Ye et al., 2022), and our temperature findings, we observed ipsilateral *Rprm*$^+$ fibers within subpopulations of the thermoregulatory preoptic area (POA), such as the medial preoptic area (MPO) and anteroventral periventricular nucleus (AVPV). In addition, *Rprm*$^+$ fibers were detected in several nuclei of the amygdala and its extended region, which process sensory cues relevant to social behavior and survival: the bed nuclei of the stria terminalis (BST), central amygdalar nucleus (CEA), the basomedial amygdalar nucleus (BMA), and the basolateral amygdalar nuclei (BLA). As with the expression of Cre-dependent mCherry-hM3Dq reported above, we identified similar viral expression and projection patterns in male and female mice (**Figure 2C, D**). Surprisingly, we did not detect *Rprm*$^+$ fibers in thermoregulatory brainstem regions such as the periaqueductal gray (PAG), dorsal nucleus raphe (DR), and the nucleus raphe pallidus (RPA) (**Figure 2D**). Previous work classified VMHvl^{Esr1} neurons into two distinct populations with minimal overlap based on their projection patterns, one projecting to anterior structures such as the MPO and another projecting to posterior regions like the PAG (Hashikawa et al., 2017; Lo et al., 2019; Wang et al., 2019). Fiber innervation suggests that VMHvl^{Rprm} neurons may represent a subset of the anteriorly-projecting VMHvl^{Esr1} population.

Neither cold- nor sickness-induced thermogenesis are associated with cFOS immunoreactivity in the VMHvl

Given the identification of VMHvl^{Rprm} neuronal projections within the POA, a region known to regulate cold-induced thermogenesis (Morrison et al., 2012; Morrison and Nakamura, 2011; Muñoz Zamora et al., 2025; Nakamura and Morrison, 2008; Tan and Knight, 2018) and

sickness-induced fever (Lazarus et al., 2007; Machado et al., 2025, 2020; Osterhout et al., 2022; Piñol et al., 2021), we used cFOS protein expression (encoded by the *Fos* immediate early gene) as a proxy of cellular activity to assess the activation of VMHvl neurons across these two thermoregulatory contexts (**Figure 3.5A**). To test for a role in cold-mediated cellular responses, mice of both sexes were housed at 23°C or 4°C for 4 hours and processed for cFOS immunoreactivity (**Figure 3.5A**). In males, we identified significant cold-induced cFOS immunoreactivity in the ARH (Šídák's multiple comparisons test following significant interaction, $t_{27} = 2.569$, $p = 0.0474$; **Figure 3.5B, C**) and VMHdm ($t_{27} = 3.330$, $p = 0.0075$) as expected based on prior studies (Deem et al., 2020; Feng et al., 2022; Yang et al., 2021). However, cold exposure did not induce cFOS immunoreactivity in the VMHvl of males ($t_{27} = 0.1807$, $p = 0.9971$; **Figure 3.5B, C**) or females (**Figure 3.5D, E**). In females, only a main effect of hypothalamic nuclei on cFOS immunoreactivity was detected ($F(2, 42) = 8.544$, $p = 0.0008$; **Figure 3.5D, E**), with no significant differences across ambient temperatures. Altogether, cFOS analyses fail to implicate the VMHvl in the cold response. Lipopolysaccharide (LPS)-induced fever represents another extensively studied hyperthermic context, at least in male mice (Lazarus et al., 2007; Machado et al., 2025, 2020; Osterhout et al., 2022; Piñol et al., 2021). To test the involvement of the VMHvl in the fever response in females, mice were treated via IP injection with vehicle or 50 µg/kg LPS (**Figure 3.5A**). Significant LPS-induced cFOS immunoreactivity was identified in the ARH (Šídák's multiple comparisons test following significant interaction, $t_{48} = 10.21$, $p < 0.0001$; **Figure 3.5F, G**) as expected based on previous findings (Hussein et al., 2025; Osterhout et al., 2022; Reis et al., 2015), but not in the VMHdm or VMHvl. Analysis of T_c revealed the successful generation of a low-grade fever (treatment x time interaction: $F(45, 360) = 1.466$, $p = 0.0321$; **Figure 3.5H**), with sickness further verified by a significant reduction in body weight following LPS treatment ($t_{16} = 2.863$, $p = 0.0113$; **Figure 3.5I**). Thus, although VMHvl^{Rprm} neurons are capable of driving hyperthermia, cFOS analyses fail to implicate these neurons in cold- or fever-mediated responses.

DISCUSSION

In this study, we leveraged our novel *Rprm*$^{Cre\text{-}FRT}$ mouse model in combination with chemogenetic, circuit tracing, and *ex vivo* immediate-early gene detection approaches to define the thermoregulatory function, anatomical connectivity, and context-dependent activity, respectively, of VMHvl^{Rprm} neurons. While our previous siRNA studies showed that *Rprm* gene knockdown increases T_c and BAT thermogenesis but does not affect movement, here we uncover a broader thermogenic role for VMHvl^{Rprm} neurons, by which their activity is sufficient to induce a long-lasting arousal state characterized by hyperthermia driven by changes in BAT thermogenesis, tail skin vasoconstriction, and hyperactivity. Further, we discover that the activity of *Rprm*$^{+}$ neurons in the MBH is not required for the circadian elevations in T_c observed at night. Thus, while VMHvl^{Rprm} neurons are capable of inducing pronounced and sustained changes in T_c, their involvement in coordinating thermoregulatory output is likely context dependent. To this end, *ex vivo* histological analysis of cFOS protein expression failed to detect neuronal activation in the VMHvl during cold- and sickness-mediated thermal challenges. Of course, the absence of cFOS immunoreactivity does not exclude its involvement; however, cFOS immunoreactivity was robustly induced in other regions that have been shown to be important for cold- or sickness-induced temperature changes(Deem et al., 2020; Feng et al., 2022; Hussein et al., 2025; Osterhout et al., 2022; Reis et al., 2015; Yang et al., 2021). These analyses of sufficiency, necessity, and connectivity, help establish the functional capacity, requirement, and downstream circuitry of VMHvl^{Rprm} neurons, but do not reveal the physiologically relevant context(s) requiring *Rprm*-mediated thermoregulation, which we aim to elucidate in Chapter 4.

FIGURES

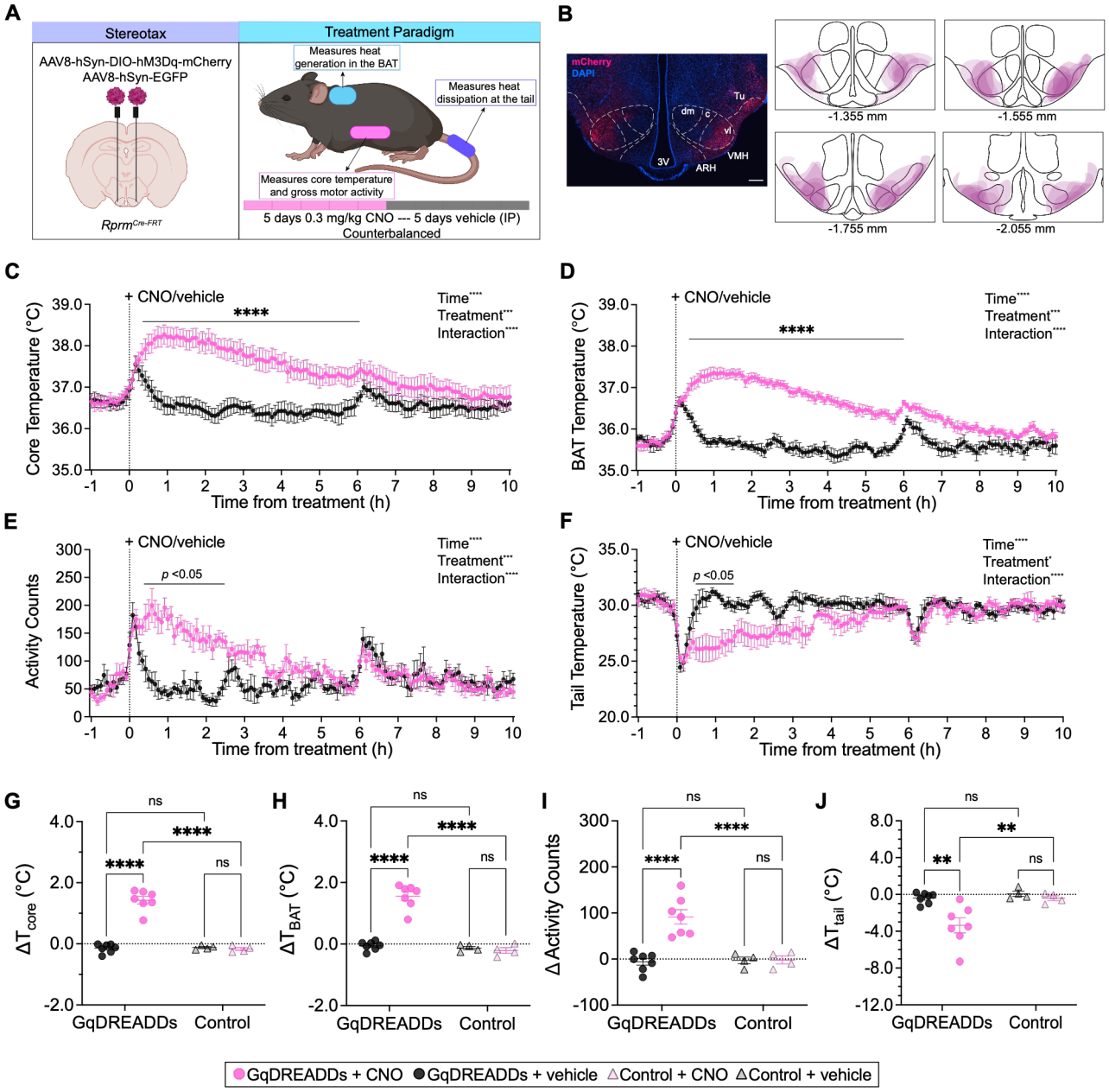


Figure 3.1: Activating VMHvl^{Rprm} neurons is sufficient to elicit a sustained hyperthermia in female mice

(A) Experimental design to activate VMHvl^{Rprm} neurons and measure thermoregulatory responses in adult (8-11 weeks of age) *Rprm*$^{Cre-FRT}$ female mice. (B) Left, representative image of mCherry fluorescence in the VMHvl of an hM3Dq-injected mouse; scale bar = 100 µm. Right,

depiction of mCherry expression across all hM3Dq-expressing mice (*n* = 7) with approximate bregma positions. (C to F) 5-minute (min) continuous recordings for (C) T_c (D) T_{BAT}, (E) GMA, and (F) T_{tail}, plotted beginning the hour prior and up to 10 hours after CNO/vehicle administration in hM3Dq-expressing mice, averaged across 5-days of treatment (CNO in pink, saline in black, *n* = 7). Data are displayed as the mean ± SEM with pairwise comparisons performed using Šídák's multiple comparison test following a significant interaction in a two-way repeated measures (RM) ANOVA. Spikes near the 6-hour mark are due to handling. (G to J) Average change (Δ) in (G) T_c (H) T_{BAT}, (I) GMA, and (J) T_{tail}, from baseline following administration of CNO (pink) or vehicle (black) in hM3Dq-expressing (*n* = 7, circles) and control (*n* = 4, triangles) female mice. Pairwise comparisons were performed using Fisher's uncorrected LSD test following a significant interaction in a two-way RM ANOVA. For all data, **p* < 0.05, ***p* < 0.01, ****p* < 0.001, *****p* < 0.0001, and ns = not significant. VMH = ventromedial nucleus of the hypothalamus; dm = dorsomedial, c = central, & vl = ventrolateral subdivisions, ARH = arcuate nucleus, Tu = tuberal nucleus, 3V = third ventricle.

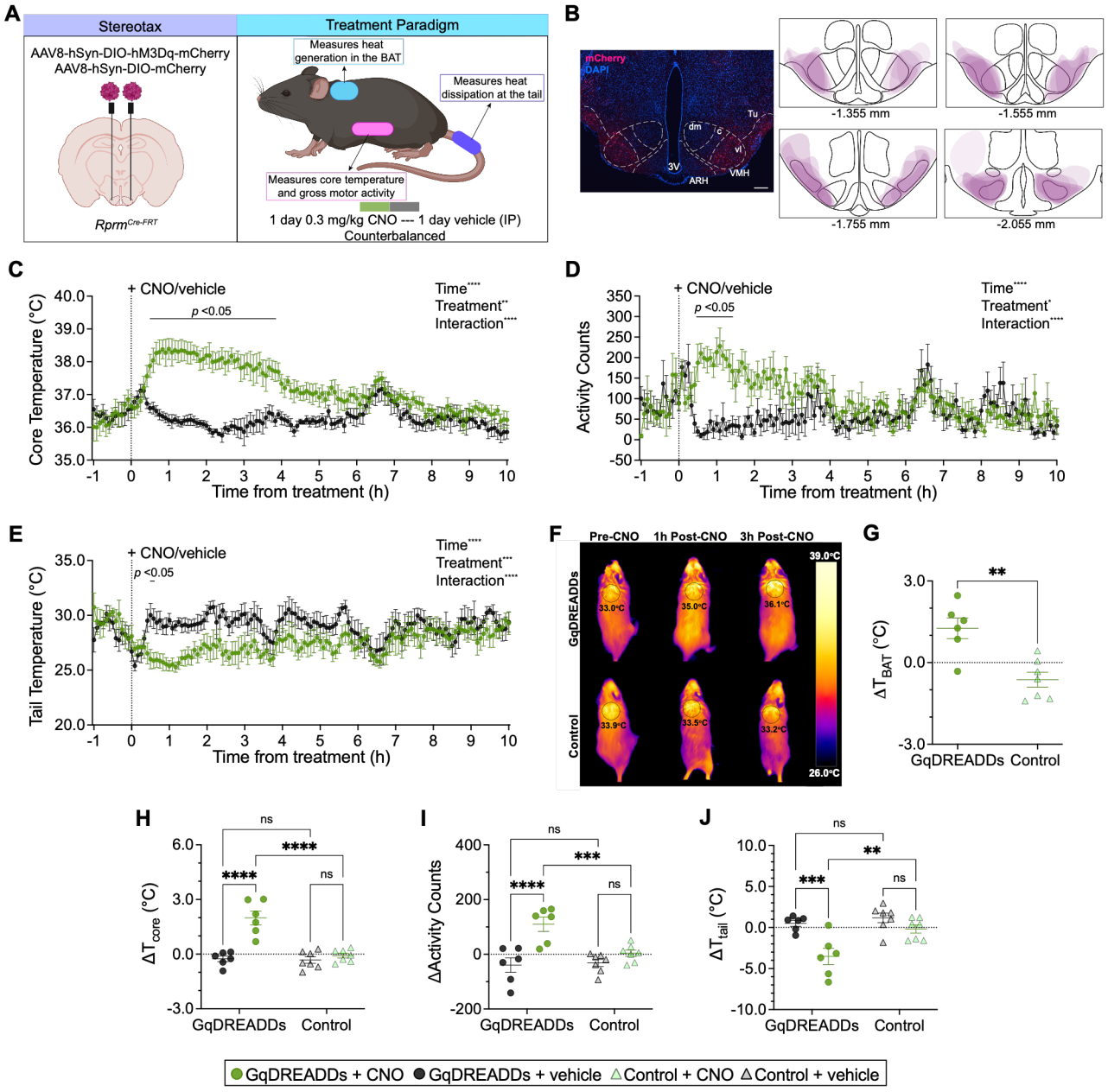


Figure 3.2: Chemogenetic activation of VMHvl^{Rprm} neurons alters the thermoregulatory profile of male mice

(A) Experimental design to activate VMHvl^{Rprm} neurons and measure thermoregulatory responses in adult (11-13 weeks of age) *Rprm*$^{Cre-FRT}$ male mice. (B) Left, representative image of mCherry fluorescence in the VMHvl of an hM3Dq-injected mouse; scale bar = 100 μm. Right, depiction of mCherry expression across all hM3Dq-expressing mice (*n* = 6) with approximate bregma positions. (C to E) 5-min recordings for (C) T_c, (D) GMA, and (E) T_{tail} plotted

continuously beginning the hour prior and up to 10 hours after CNO/vehicle treatment in hM3Dq-expressing males (CNO in green, saline in black, n = 6). Data are displayed as mean ± SEM with statistical analyses performed using a mixed-effects model and Restricted Maximum Likelihood (REML) due to missing values and pairwise comparisons performed using Šídák's multiple comparison test following a significant interaction. (F) Representative infrared images of hM3Dq-expressing (top) and control (bottom) mice taken across 3 different timepoints. Ovals on the back of mice depict the interscapular region used for T_{BAT} analysis with average values shown. (G) ΔT_{BAT} in hM3Dq-expressing (n = 6, circles) and control (n = 7, triangles) mice with mean ± SEM and data points for each mouse; statistical analysis performed using an unpaired t-test. (H to J) Average (H) ΔT_c, (I) ΔGMA, and (J) ΔT_{tail} following administration of CNO (green) or saline (black) in hM3Dq-expressing (n = 6, circles) and control (n = 7, triangles) mice. Pairwise comparisons were performed using Fisher's uncorrected LSD test following a significant interaction in a two-way RM ANOVA. For all data, *p < 0.05, **p < 0.01, ***p < 0.001, ****p < 0.0001, and ns = not significant. VMH = ventromedial nucleus of the hypothalamus; dm = dorsomedial, c = central, & vl = ventrolateral subdivisions, ARH = arcuate nucleus, Tu = tuberal nucleus, 3V = third ventricle.

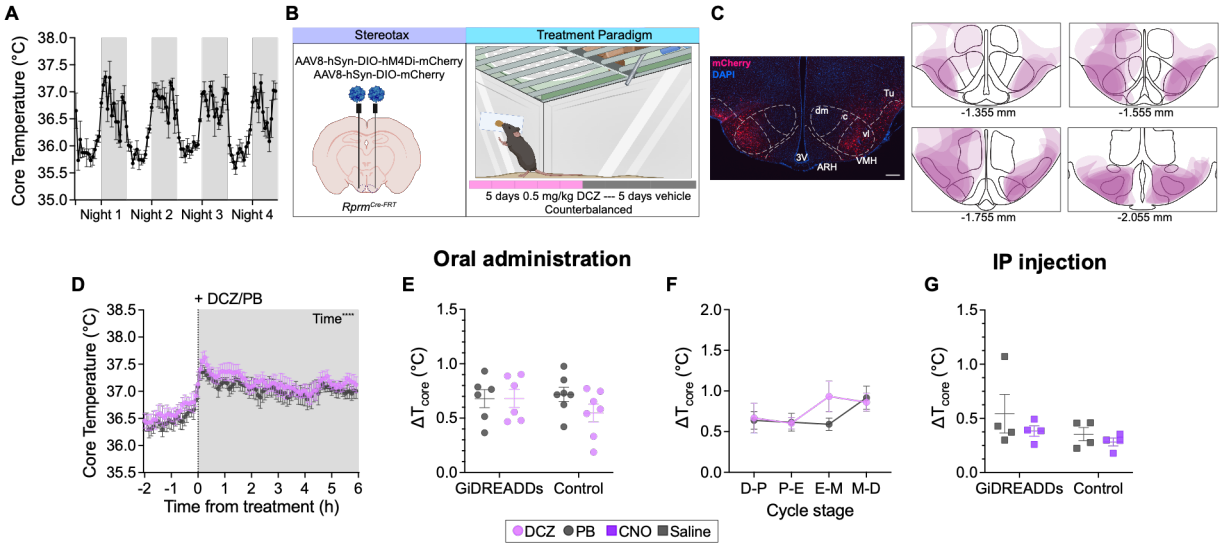


Figure 3.3: The activity of *Rprm*$^{+}$ neurons in the MBH is not required for the circadian elevations in T_c observed at night

(A) Representative T_c trace in *Rprm*$^{Cre\text{-}FRT}$ female mice (*n* = 4) demonstrating expected circadian fluctuations characterized by nocturnal T_c elevations. Alternating shaded and light areas depict the 12h dark and light cycles, respectively. (B) Experimental design to inhibit *Rprm*$^{+}$ neurons and measure thermoregulatory responses in adult (10-13 weeks of age) *Rprm*$^{Cre\text{-}FRT}$ female mice. (C) Left, representative image of mCherry fluorescence in the MBH of an hM4Di-injected mouse; scale bar = 100 µm. Right, depiction of mCherry expression across all hM4Di-expressing mice (*n* = 6) with approximate bregma positions. (D) 5-min continuous T_c recordings plotted beginning 2 hours prior and up to 6 hours after oral DCZ/PB administration in hM4Di-expressing mice (DCZ in pink circles, PB in black circles, *n* = 6). Data are displayed as the mean ± SEM with statistical analysis performed using a two-way RM ANOVA. (E) Average ΔT_c following oral administration of DCZ (pink circles) or PB (black circles) in hM4Di-expressing (*n* = 6) and control (*n* = 7) female mice. Data are displayed as the mean ± SEM and data points for each mouse. Statistical analysis was performed using a two-way RM ANOVA. (F) ΔT_c across estrous cycle stages in hM4Di-expressing mice treated with DCZ/PB (DCZ in pink, PB in black, *n* = 5-6 per stage except E-M with *n* = 3). Data are displayed as the mean ± SEM with statistical

analysis performed using a mixed-effects model and Restricted Maximum Likelihood (REML) due to missing values. (G) Average ΔT_c following IP administration of CNO (purple squares) or saline (black squares) in hM4Di-expressing (n = 4) and control (n = 4) female mice. Data are displayed as the mean ± SEM and data points for each mouse. Statistical analysis was performed using a two-way RM ANOVA. For all data, *p < 0.05, **p < 0.01, ***p < 0.001, ****p < 0.0001, and ns = not significant. VMH = ventromedial nucleus of the hypothalamus; dm = dorsomedial, c = central, & vl = ventrolateral subdivisions, ARH = arcuate nucleus, Tu = tuberal nucleus, 3V = third ventricle.

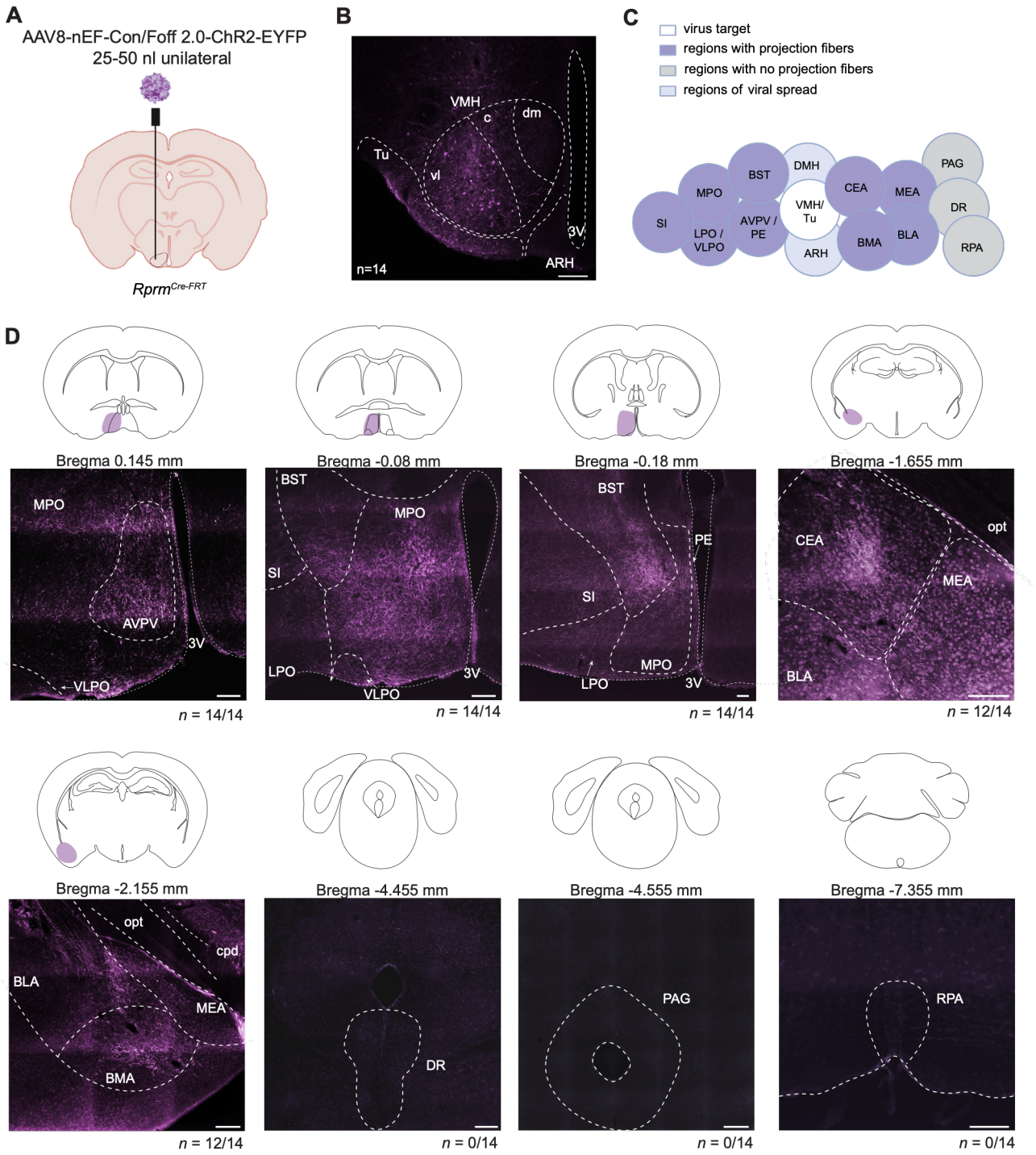

A
AAV8-nEF-Con/Foff 2.0-ChR2-EYFP
25-50 nl unilateral
Rprm Cre-FRT
B
VMH
c
dm
Tu
vl
3V
n=14
ARH
C
virus target
regions with projection fibers
regions with no projection fibers
regions of viral spread
SI
MPO
BST
DMH
VMH/
Tu
AVPV /
PE
LPO /
VLPO
ARH
CEA
MEA
BMA
BLA
PAG
DR
RPA
D
Bregma 0.145 mm
MPO
AVPV
3V
VLPO
n = 14/14
Bregma -0.08 mm
BST
MPO
SI
LPO
3V
VLPO
n = 14/14
Bregma -0.18 mm
BST
PE
SI
MPO
LPO
3V
n = 14/14
Bregma -1.655 mm
CEA
opt
MEA
BLA
n = 12/14
Bregma -2.155 mm
opt
cpd
BLA
MEA
BMA
n = 12/14
Bregma -4.455 mm
DR
n = 0/14
Bregma -4.555 mm
PAG
n = 0/14
Bregma -7.355 mm
RPA
n = 0/14

Figure 3.4: VMHvl^{Rprm} neurons project to nodes involved in thermoregulation and the processing of social and survival sensory cues

(A) Viral strategy for the visualization of VMHvl^{Rprm} neuronal fibers in *Rprm*$^{Cre\text{-}FRT}$ mice (*n* = 14 total, 9 males and 5 females; 9-14 weeks of age). (B) Representative image of the VMHvl with EYFP+ cell bodies (lavender); scale bar = 100 μm. (C) Schematic of brain regions depicting: 1) the VMHvl target region in white, 2) brain regions with visible projection fibers in purple, 3) regions with no detected projection fibers in gray, and 4) regions with viral spread as evidenced by the presence of one/two or more EYFP+ cell bodies in light blue. (D) Representative brain sections with anterior-posterior bregma positions indicated. The number of observations (presence of EYFP+ fibers) out of 14 total mice is indicated below each image; scale bars = 100 μm. For all images, ARH = arcuate nucleus, AVPV = anteroventral periventricular nucleus, BLA = basolateral amygdalar nucleus, BMA = basomedial amygdalar nucleus, BST = bed nuclei of the stria terminalis, CEA = central amygdalar nucleus, DMH = dorsomedial nucleus of the hypothalamus, DR = dorsal nucleus raphe, LPO = lateral preoptic area, MEA = medial amygdalar nucleus, MPO = medial preoptic area, PAG = periaqueductal gray, PE = periventricular hypothalamic nucleus, RPA = nucleus raphe pallidus, SI = substantia innominata, VLPO = ventrolateral preoptic nucleus, VMH = ventromedial nucleus of the hypothalamus, opt = optic tract, Tu = tuberal nucleus, 3V = third ventricle.

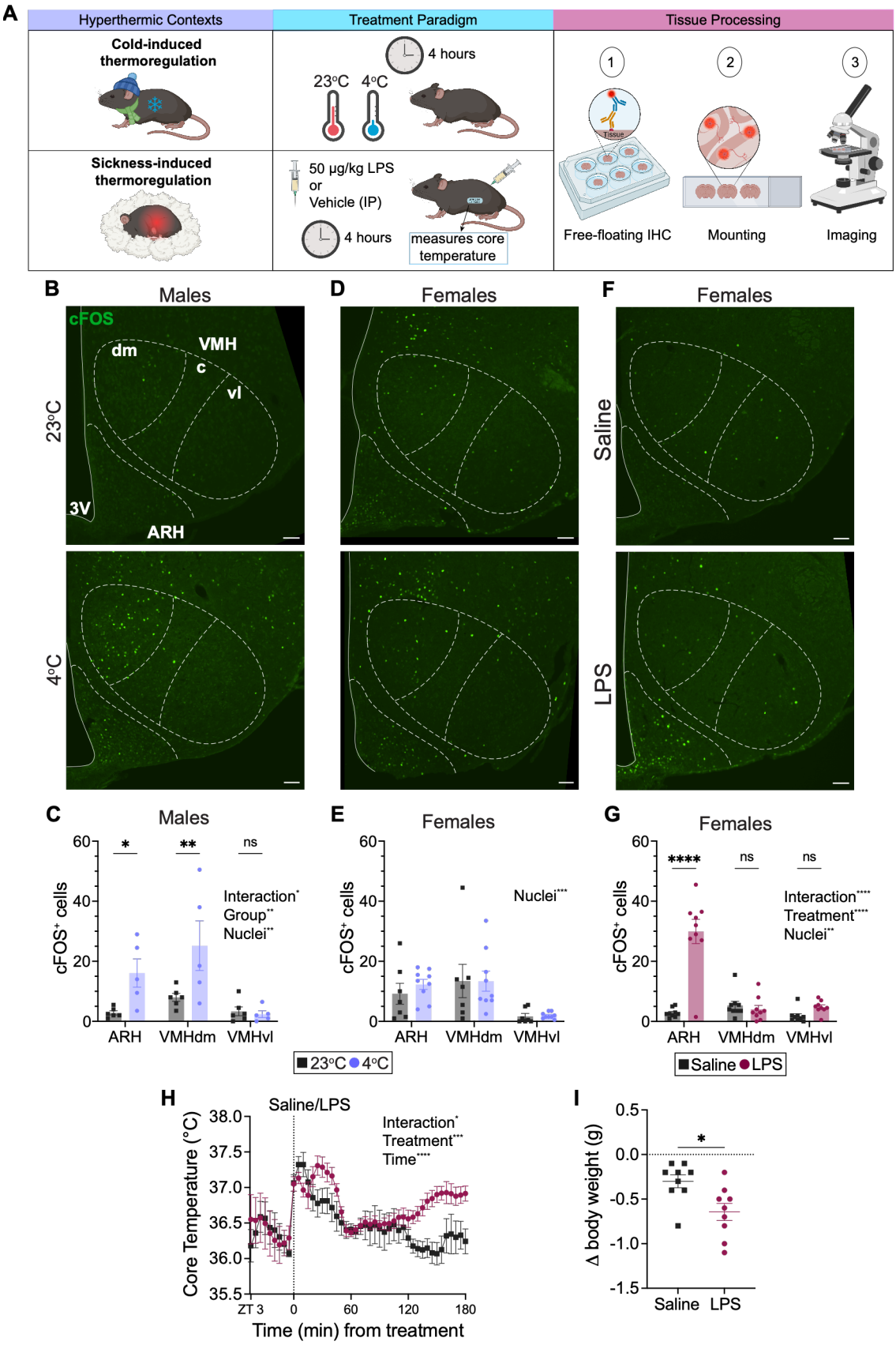

A
Hyperthermic Contexts
Treatment Paradigm
Tissue Processing
Cold-induced thermoregulation
4 hours
23°C
4°C
Sickness-induced thermoregulation
50 µg/kg LPS or Vehicle (IP)
4 hours
measures core temperature
1
2
3
Tissue
Free-floating IHC
Mounting
Imaging
B
Males
cFOS
dm
VMH
c
vl
3V
ARH
23°C
D
Females
F
Females
Saline
LPS
4°C
C
Males
cFOS+ cells
Interaction*
Group**
Nuclei**
ARH
VMHdm
VMHvl
23°C 4°C
E
Females
Nuclei***
G
Females
Interaction****
Treatment****
Nuclei**
Saline LPS
H
Saline/LPS
Interaction*
Treatment***
Time****
Core Temperature (°C)
ZT 3
Time (min) from treatment
I
Δ body weight (g)
Saline
LPS

Figure 3.5: Neither cold- nor sickness-induced thermogenesis are associated with cFOS immunoreactivity in the VMHvl

(A) Experimental design to assess VMHvl activation during cold exposure and LPS fever induction using cFOS immunoreactivity as a proxy of cellular activity. (B) Representative cFOS immunoreactivity (green) in male mice housed at 23 °C (top) or 4 °C (bottom) for 4 hours; scale bars = 100 μm. (C) Quantification of cFOS+ cells in the ARH, VMHdm, and VMHvl in male mice housed for 4 hours at 23 °C (*n* = 6, black squares) or 4 °C (*n* = 5, blue circles). Pairwise comparisons were performed using Šídák's multiple comparison test following a significant interaction in an ordinary two-way ANOVA. (D) Representative cFOS immunoreactivity in 23 °C and 4 °C exposed females as in (B). (E) Quantification of cFOS+ cells in the ARH, VMHdm, and VMHvl in female mice housed for 4 hours at 23 °C (*n* = 7, black squares) or 4 °C (*n* = 9, blue circles). Statistical analysis was performed using an ordinary two-way ANOVA. (F) Representative cFOS immunoreactivity in female mice 4 hours after treatment with vehicle (top) or 50 μg/kg LPS (bottom) presented as in (B). (G) Quantification of cFOS+ cells in the ARH, VMHdm, and VMHvl in females treated with vehicle (*n* = 9, black squares) or 50 μg/kg LPS (*n* = 9, red circles). Pairwise comparisons were performed using Šídák's multiple comparison test following a significant interaction in an ordinary two-way ANOVA. (H) ΔBody weight following treatment (vehicle in black squares, LPS in red circles, *n* = 9). Statistical analysis performed using an unpaired *t*-test with mean ± SEM and data points shown for each mouse. (I) 5-min T_c recordings plotted from baseline and up to 180-min after treatment with vehicle (n=5, black squares) or LPS (n=5, red circles). Baseline represents the morning of the assay before any handling (ZT3), with manipulations occurring at ZT 5-7 and aligned based on time of injection (marked 0 on the x-axis). Statistical analysis was performed using a two-way RM ANOVA. For all data, **p* < 0.05, ***p* < 0.01, ****p* < 0.001, *****p* < 0.0001, and ns = not significant. VMH = ventromedial nucleus of the hypothalamus; dm = dorsomedial, c = central, & vl = ventrolateral subdivisions, ARH = arcuate nucleus, 3V = third ventricle.

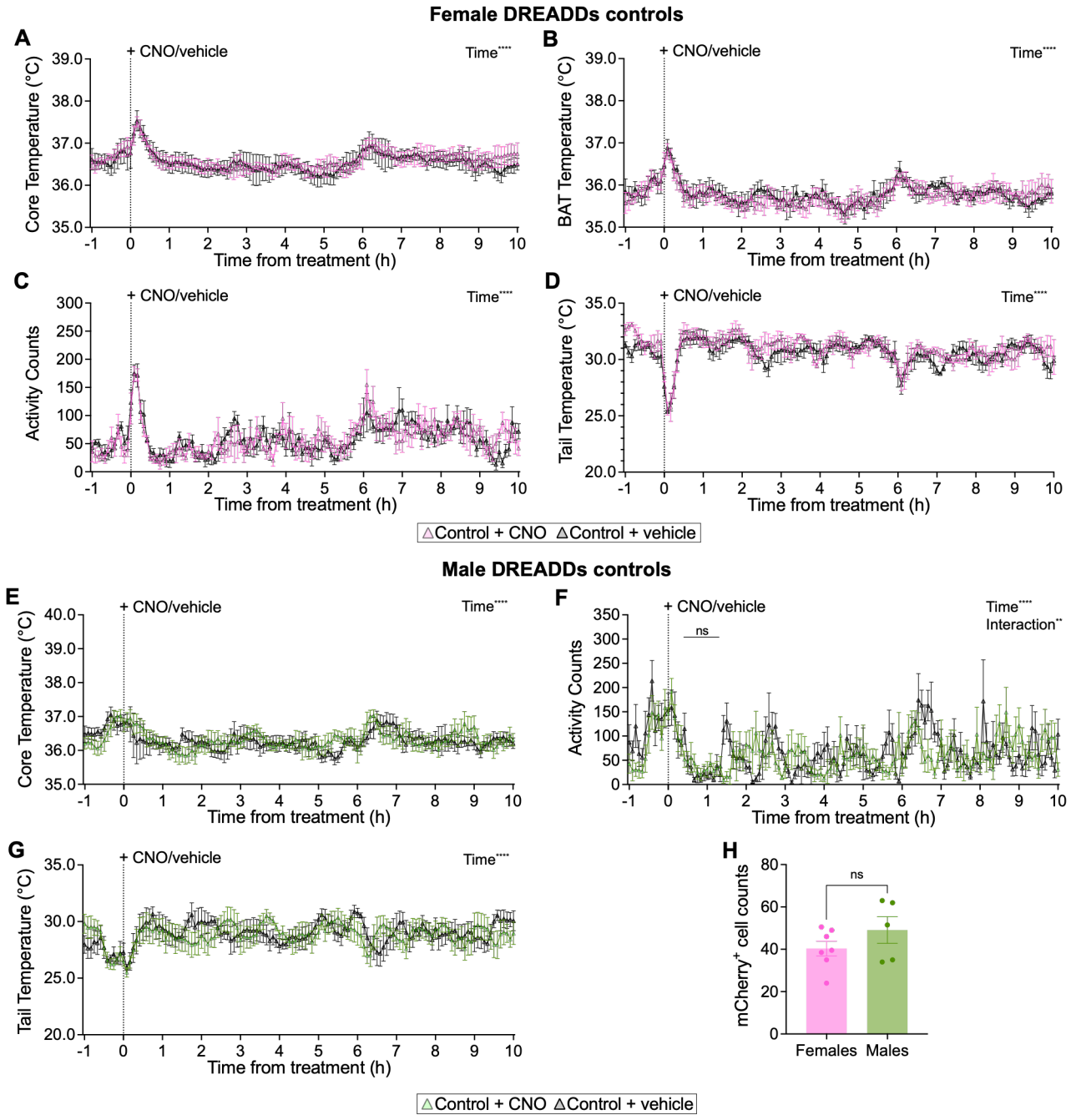


Figure S3.1 related to Figures 3.1 and 3.2: CNO treatment in mice lacking hM3Dq expression does not alter thermoregulation

(A to D) 5-min recordings plotted continuously in *Rprm*$^{Cre\text{-}FRT}$ female mice receiving a viral vector lacking hM3Dq (control mice; CNO in pink, vehicle in black, n = 4) for (A) T_c (B) T_{BAT}, (C) GMA, and (D) T_{tail}. Data were collected, analyzed, and presented as in Figure 1, C to F. (E to G) 5-min

recordings plotted continuously in *Rprm*$^{Cre\text{-}FRT}$ male mice receiving a viral vector lacking hM3Dq (control mice; CNO in green, vehicle in black, $n = 7$) for (E) T_c, (F) GMA, and (G) T_{tail}. Data is displayed as in (A to D). Statistical analyses were performed using a mixed-effects model and Restricted Maximum Likelihood (REML) due to missing values, with pairwise comparisons performed using Šídák's multiple comparison test following a significant interaction. (H) Quantification of mCherry$^+$ cells within the VMHvl of hM3Dq-expressing female ($n = 7$, pink circles) and male ($n = 5$, green circles) mice with mean ± SEM and individual data points shown; statistical analysis performed using an unpaired *t*-test. For all data, *$p < 0.05$, **$p < 0.01$, ***$p < 0.001$, ****$p < 0.0001$, and ns = not significant.

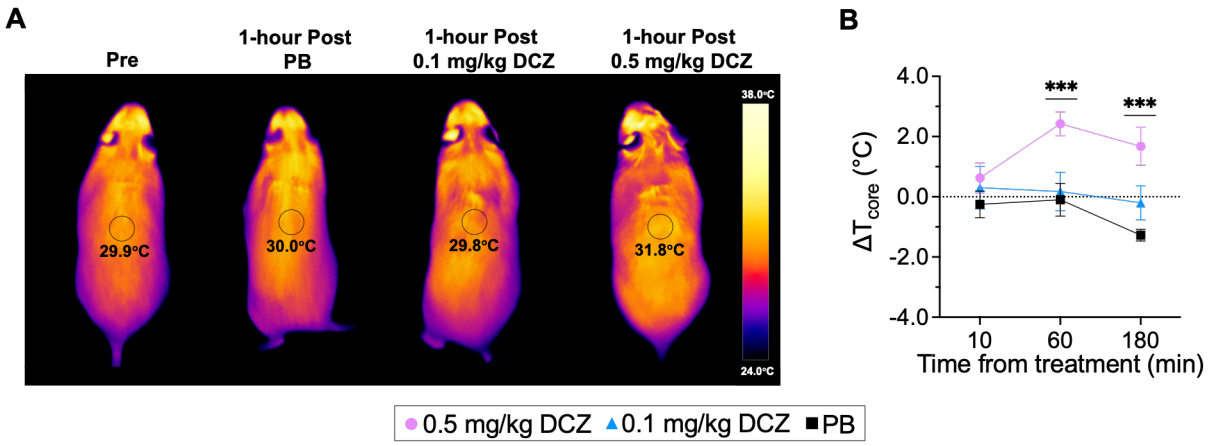


Figure S3.2 related to Figure 3.3: Optimizing the oral administration of DCZ via voluntary ingestion of peanut butter

(A) Representative infrared images of an hM3Dq-expressing *Rprm*$^{Cre\text{-}FRT}$ mouse taken across 4 different timepoints (pre = before treatment, post = after treatment; treatments include PB only, 0.1 mg/kg DCZ, or 0.5 mg/kg DCZ). Ovals on the backs of mice depict the region used for T_c analysis with average values shown. (B) ΔT_c following oral treatment (PB-only in black squares, 0.1 mg/kg DCZ in blue triangles, 0.5 mg/kg DCZ in pink circles, *n* = 4). Pairwise comparisons were performed using Tukey's multiple comparisons test following a significant interaction in a 2-way RM ANOVA.

MATERIALS AND METHODS

Mouse models

All procedures were approved by the UCLA Institutional Care and Use Committee (IACUC) in accordance with the National Institutes of Health (NIH) guide for the care and use of laboratory animals and carried out in approved facilities at UCLA. Mice were housed under a 12:12 light-dark cycle (zeitgeber time (ZT) 0 = 7:00 am) under controlled humidity conditions at 22-23 °C ambient temperatures with *ad libitum* access to water and breeder chow (Mouse Diet 9F 5020, 20% protein, 9% fat, LabDiet; St. Louis, MO, USA).

Experiments were performed on gonadally intact adult animals. The sex of a mouse was determined at weaning based on anogenital distance and confirmed postmortem based on the presence of ovaries or testes (Massa et al., 2023). *Rprm*$^{Cre\text{-}FRT}$ founder mice on a C57BL/6J background were generated by the University of California San Diego Transgenic & CRISPR Mouse Core and later bred and maintained in approved conditions at UCLA (Park et al., 2026). Aside from chemogenetic studies that were conducted in both heterozygous and homozygous mice, all other experiments using *Rprm*$^{Cre\text{-}FRT}$ mice were performed using homozygous adults. The homozygous *Rprm*$^{Cre\text{-}FRT}$ line were maintained using in-crosses. Cold exposure studies were conducted in wildtype littermates from the *Esr1*^{Cre} line and LPS studies were carried out in C57BL/6J mice obtained from Jackson Laboratories (JAX stock no. 000664).

Mouse surgical procedures

For all surgeries, mice were anesthetized with 2-3% isoflurane and administered pain management medications, including buprenorphine (0.01 mg/mL) and carprofen (0.58 mg/mL), on the day of surgery and the following day. Daily body weight and health monitoring was conducted for at least a week after surgery.

Stereotaxic surgery

Surgeries were performed on adult (8-14 weeks of age) *Rprm*$^{Cre\text{-}FRT}$ mice of both sexes. Following anesthetization, mice were placed on a stereotaxic device (Kopf Instruments model 1900) with isoflurane maintained at 2-2.5%. Viruses were targeted to the VMHvl of adult mice using the following coordinates: 1.50 mm posterior to bregma, 0.80-0.85 mm lateral to the midline, and 5.50-5.60 mm below the brain surface. Viruses were delivered at a rate of 5-10 nL/sec using pulled glass needles connected to Hamilton syringes. The needle was slowly removed from the brain 10 min after infusion to allow for viral diffusion. Viruses were delivered bilaterally into the VMHvl except for anterograde tracing studies, where the AAV was unilaterally injected into the left hemisphere. Details on viral titers and injection volumes can be found in **table 1** below. While we targeted the VMHvl for stereotaxic manipulations, viral expression extended to the connecting tuberal nucleus or was observed throughout the broader mediobasal hypothalamus. We include schematics of viral spread and/or quantifications for all experiments.

Experiment	Virus	Depositor and procurement	Titer (vg/mL)	Volume (nL) per hemisphere
Cre-mediated Activating DREADD	AAV8-hSyn-DIO-hM3D(Gq)-mCherry	Bryan Roth, Addgene viral prep # 44361-AAV8	≥ 4×10^{12}	150
Cre-mediated Anterograde tracing	AAV8-nEF-Con/Foff 2.0-ChR2-EYFP	Karl Deisseroth, INTRSECT 2.0 Project, Addgene viral prep # 137163-AAV8	≥ 1×10^{13}	25-50
Fluorescent EGFP control	AAV8-hSyn-EGFP	Bryan Roth, Addgene viral prep # 50465-AAV8, pseudotyped at UCLA Vector Core	~1×10^{9} - 1×10^{10}	Matching volume to experimental animals
Fluorescent mCherry control	AAV8-hSyn-DIO-mCherry	Bryan Roth, Addgene viral prep # 50459-AAV8	≥ 1×10^{13}	Matching volume to experimental animals

Passive and continuous tracking of core body temperature (T_c)

Implantation of thermo-loggers occurred either on the same day as stereotaxis or one week before/after, depending on availability. In either case, mice were allowed to recover for at

least 2-weeks following surgery before experiments were conducted. For all experiments detailed below, mice were singly housed with *ad libitum* access to food and water for the duration of telemetry recordings, which all occurred in the home cage.

Short-range telemetry was collected via G2 E-Mitters and the ER4000/4500 receiver pads (Starr Life Sciences; Oakmont, PA, USA). This permits the continuous monitoring of T_c and gross motor activity (GMA), defined as movements carried out in the x, y, and z axis including running, walking, rearing, and side-to-side displacements. DST nano-T thermo-loggers (Star-Oddi; Garðabær, Iceland) were also employed for continuous T_c recordings. Both the G2 E-Mitters and nano-T thermo-loggers were implanted intraperitoneally following sterilization with Metricide^{TM}28 Glutaraldehyde High-Level Disinfectant (Metrex Research; Orange, CA, USA) as described in (Raam et al., 2026).

To record the temperature of the BAT, DST nano-T or CubiSens^{TM} TS100/TS110 (CubeWorks; Ann Arbor, MI, USA) thermo-loggers were implanted subcutaneously above the interscapular BAT using 3D-printed custom sleeves attached to the skin above the depot (Park et al., 2026). To record tail skin temperature, thermo-loggers were attached to the base of the tail using 3D-printed sleeves and Loctite 454 instant adhesive (Henkel; Düsseldorf, Germany). Given the size of the thermo-loggers (~17 x 6 mm), implantation over the BAT was only done for short (less than 2 week-long) experiments to avoid skin lesions. At the end of experiments, raw data from G2 E-Mitters, DST nano-T, and CubiSens thermo-loggers was extracted using VitalView (version 5.1 & 6.0, Starr Life Sciences), CubiSens^{TM} TS Interface (version 3.3, CubeWorks), and Mercury (version v6.69, Star-Oddi) data acquisition software, respectively.

Infrared thermography

Infrared images were captured in awake animals using an e60bx camera (FLIR systems; Wilsonville, OR, USA). Images were taken from a constant distance above each mouse and

later analyzed using the FLIR Tools software (Version 6.4, FLIR systems). The average temperature of a circular area centered over the scapulae or the midline of the body was used to then calculate ΔT_{BAT} or ΔT_c respectively.

Estrous cycle staging

For mice undergoing chemogenetic inhibition, daily vaginal lavages with 0.9% saline were performed at ZT 1-3. Estrous staging was assessed via light microscopy using a Leica DM1000 microscope (Leica Microsystems Inc, Deerfield, IL, USA) and based on the relative proportion of leukocytes and nucleated vs cornified epithelial cells (Byers et al., 2012; Massa et al., 2023).

Acute cold exposure

Adult (8-14 weeks of age) mice were placed into clean cages singly housed with the standard 2-nestlets for bedding and *ad libitum* food and water the day before cold exposure. A Precision Model 818 Incubator (Thermo Scientific) was set to an ambient temperature of 4 °C with humidity monitored and maintained within 30%. Once ambient temperature stabilized at 4 °C, mice were placed in the incubator for 4 hours, with controls moved to a holding room at 23 °C. Mice were euthanized at the 4-hour time point, with brains collected and processed as described below.

Drug treatments

Clozapine-N-oxide (CNO)

Stock solutions of CNO (Sigma-Aldrich C0832) at a concentration of 20 mg/mL in DMSO were stored at –20 °C. For chemogenetic activation of *Rprm*$^+$ neurons, a final concentration of 0.3 mg/kg CNO or 0.15% DMSO in saline was administered via IP injection, with treatments occurring during the inactive light phase of the light-dark cycle, between ZT 1-2 for females and ZT 2-6 for males. For chemogenetic inhibition studies, a final concentration of 3 mg/kg CNO or

1.5% DMSO in saline was administered via IP injection based on prior literature (Feng et al., 2022; Silva et al., 2013; Ye et al., 2022) with treatments occurring at ZT 12.

Deschloroclozapine (DCZ)

DCZ solid powder (MCE® HY-42110) was mixed into peanut butter paste (SKIPPY® creamy peanut butter, PB) and fully dissolved by placing on a hot plate for 1-2 hours at 30°C to create stock concentrations of 0.2-0.4 mg DCZ/g PB, stored at 4°C for up to a week. A final concentration of 0.5 mg/kg DCZ or PB alone was administered.

Mice were weighed daily between ZT 9-10 to determine drug dose, with administrations occurring at lights off (ZT 12). A small bolus of PB +/- DCZ (~25-65 mg based on body weight and DCZ stock concentration) was placed on a piece of tape and adhered to the home cage wall, with the tape removed shortly after mice consumed the bolus. Mice were habituated to this manipulation (cage lid opening, placement of PB on tape) for 3 days prior to the beginning of the experiment. This habituation period was successful, with most mice eating the entire PB bolus within 5 minutes.

Lipopolysaccharides (LPS)

Sickness-mediated fever was induced by IP injection of LPS from *Escherichia coli* 0111:B4 (Sigma-Aldrich L2630) at a dose of 50 μg/kg with control mice receiving vehicle (saline)(Osterhout et al., 2022). Mice were singly housed and acclimated to handling 3-4 days before treatment. To ensure mice achieved hyperthermia while housed in standard vivarium ambient temperatures (22-23 °C), they were provided with external sources of warmth including 4 nestlets for nest building and a Shepard shack. Injections took place between ZT 5-7. Mice were euthanized 4-hours after treatment and brains processed for immunohistochemistry and analyzed as described below.

T_c analysis

DREADDs-mediated chemogenetics

For chemogenetic activation studies, adult (8-11 weeks of age) female mice underwent consecutive 5-day treatments (5 days CNO, 2 days off, 5 days saline) via IP injections in a randomized and counterbalanced design. Adult (11-13 weeks of age) male mice underwent a 1-day treatment paradigm (1-day CNO, 1-day saline, randomized and counterbalanced). Infrared thermography was assessed on a second CNO dosing day. For chemogenetic activation, a dose of 0.3mg/kg CNO was used.

To analyze telemetry data for chemogenetic activation studies, data is presented in one of two ways: 1) Plotted continuously beginning the hour prior and up to 10 hours after treatment in 5-min recording intervals, with temperature and activity counts averaged across the 5-day treatment in females. 2) Averaged over a 1-hour pre-treatment window and a 2-hour post-treatment window, with recordings 10-30-min prior and 1-hour after IP injection omitted to minimize the effects of handling stress. This was then used to plot the average change (Δ) following treatments, calculated as the difference between ‘pre’ and ‘post’ values.

For chemogenetic inhibition studies, adult (10-13 weeks of age) female mice received 0.5 mg/kg DCZ orally (5 days DCZ, 2 days off, 5 days PB) or IP injections of 3mg/kg CNO (5 days CNO, 2 days off, 5 days saline) in a randomized and counterbalanced design. To analyze telemetry data for chemogenetic inhibition studies, data is presented in one of two ways: 1) Plotted continuously beginning 2 hours prior and up to 6 hours after treatment in 5-min recording intervals, with temperature averaged across the 5-day treatment in females. 2) Averaged over a 1-hour pre-treatment window and a 1-hour post-treatment window from ingestion of the ligand/vehicle. This was then used to plot the average change (Δ) following treatments, calculated as the difference between ‘pre’ and ‘post’ values. To determine whether thermoregulatory effects varied across the estrous cycle, vaginal cytology was collected (see

above), analyzed, and used to divide and categorize temperature across each of the 4 cycle stages.

LPS fever-induced thermoregulation

Adult female mice (18-19 weeks of age) were treated via IP injection of vehicle (saline) or 50 μg/kg LPS and 5-min T_c recordings plotted from baseline and up to 180-min after treatment. Baseline represents the morning of the assay before any handling (ZT3), with manipulations occurring at ~ZT 5-7 and aligned based on time of injection (marked 0 on the x-axis).

Tissue collection and preparation

Mice were deeply anesthetized with IP injection of sodium pentobarbital (15 mg/mL) and confirmed unconscious before proceeding. Mice were transcardially perfused with ice-cold DEPC-treated 1x phosphate-buffered saline (PBS, pH=7.4) until the lungs and liver cleared, followed by ice-cold 4% paraformaldehyde (PFA) diluted from a 16% stock solution (Electron Microscopy Sciences, Catalog# 15700) in DEPC-treated PBS. Brains were harvested, post-fixed in 4% PFA overnight, and dehydrated in 30% sucrose for 24-48 hours, maintaining RNase-free conditions throughout. Brains were then embedded in optimal cutting temperature (OCT) compound (Fisher Scientific, Catalog# 23-730-571) and stored at –80 °C until cryosectioned. Coronal sections at a thickness of 20-30 μm were collected in 4-8 series using a cryostat (Leica CM1950) and either directly mounted on slides or collected free-floating in PBS and kept in Eppendorf tubes filled with cryoprotectant solution (30% sucrose, 30% ethylene glycol, 1% polyvinylpyrrolidone in 1x PBS) stored at –20 °C until further processing.

Histology

4',6-diamidino-2-phenylindole (DAPI) stain

Validation of stereotaxic targeting for chemogenetic studies was carried out by visualization of mCherry reporter expression and a DAPI counterstain. Briefly, slide-mounted sections were brought to room temperature, or sections were mounted on slides if stored free-floating, and allowed to fully dry before proceeding. Slides were then rinsed with PBS and incubated with DAPI (1:500-1,000, Thermo Fisher Scientific, Invitrogen™ Catalog# D1306) for 5-15 min. Following 2 quick PBS rinses to wash off excess solution, slides were coverslipped with Fluoromount-G™ mounting medium (Thermo Fisher Scientific, Invitrogen™ Catalog# 00-4958-02), allowed to dry, and stored at 4 °C until imaged. Slides were imaged at 4-10x magnification using a Nikon Eclipse Ti2 inverted microscope. For chemogenetic activation, mice with unilateral and bilateral targeting had indistinguishable responses and were therefore both used for analysis, as in (Correa et al., 2015). For chemogenetic inhibition studies, only mice with bilateral targeting were included for analysis.

cFOS immunohistochemistry (IHC)

To visualize cFOS expression as a marker of cellular activity, coronal sections (20 μm in thickness) underwent free-floating IHC with a protocol adapted from (Lee et al., 2021). Tissues were first rinsed with PBS (2x5 min) and 0.01% PBS-T (PBS with 0.01% Triton X-100, 2x10 min) to wash off residual cryoprotectant. Sections were then blocked for 1 hour in 5% normal goat serum (Thermo Fisher Scientific, Invitrogen™ Catalog# 01-6201) plus 5% bovine serum albumin (BSA, Fisher Scientific, Catalog# BP9706100) with 0.3-3% Triton X-100 in PBS at room temperature and then incubated overnight at 4 °C with a monoclonal antibody, rabbit-anti-cFos (1:1,000, Cell Signaling Technology, Catalog# 2250) with 1% BSA plus 0.3-3% Triton X-100 in PBS. The following day, sections were rinsed with 0.01% PBS-T (4x10 min) and incubated with goat anti-rabbit Alexa Fluor 546 (1:500, Thermo Fisher Scientific, Catalog# A-11035) or Alexa Fluor 647 (1:500, Jackson ImmunoResearch, Catalog# 111-606-003) and DAPI (1:500-1,000) in 0.01% PBS-T for 2 hours at room temperature. Sections were then rinsed with 0.01% PBS-T

(3x10 min) and PBS (3x10 min) before mounting on slides with 0.1% gelatin in PBS. Once slides were dry, they were coverslipped with Fluoromount-G mounting medium, allowed to dry, and stored at 4 °C until imaged and analyzed as described below.

Rprm$^+$ projection mapping

A 6-7-week recovery period post-stereotaxis was allowed for viral transduction, recombination, and propagation along axons to occur prior to mice being transcardially perfused as described above. To visualize EYFP fluorescence, 30 μm coronal sections spanning the whole brain were collected and stained using a free-floating IHC technique. Briefly, sections were rinsed with PBS (3x10 min) and blocked for 1 hour in 5% NGS with 0.2% PBS-T (PBS with 0.2% Triton X-100) at 4 °C before being incubated with a polyclonal antibody, chicken-anti-GFP (1:1,000, Aves Labs Inc, catalog# 1020) in 0.2% PBS-T for 3 days at 4 °C. Sections were then rinsed with 0.2% PBS-T (1x15 min and 2x30 min) and then incubated with goat-anti-chicken Alexa Fluor 647 (1:1,000, Thermo Fisher Scientific, Catalog# A-21449) and DAPI (1:500-1,000) in 0.2% PBS-T for 24-hours at 4 °C. Sections were then rinsed with 0.2% PBS-T (1x15 min and 2x30 min) before mounting on slides. Once slides dried, they were coverslipped with Fluoromount-G mounting medium, allowed to dry further, and stored at 4 °C until imaged.

QUANTIFICATION AND STATISTICAL ANALYSIS

Image Analysis and Quantification

Brain sections were imaged at 10x magnification using a Nikon Eclipse Ti2 inverted microscope, with images imported into ImageJ (Fiji version 2.1.0/1.53c, NIH). Prior to quantification, sections from comparable bregma distances were selected to ensure a similar rostro-caudal level was analyzed for all mice in each experiment, ranging from bregma -1.455 to -1.755 mm, which we considered the central to caudal VMHvl. Regions of interest (ROIs) and anatomical notations were defined and outlined by referencing the Allen Brain Mouse (v2, 2011)

and Paxinos and Franklin (v3, 2008) atlases. Cells were identified based on co-localization of the fluorescent signal with DAPI. Once images were selected, quantifications were performed manually by a blinded investigator as follows.

cFOS immunohistochemistry (IHC)

To count the number of cFOS+ cells following immunohistochemistry, the cell counter plug-in in ImageJ was used. Brightness/contrast was adjusted uniformly across all images to minimize nonspecific background fluorescence and ensure detection of signal above background, adapted from (Deem et al., 2020; Faber et al., 2018; Jovanovic et al., 2023). Cell counts were obtained for both brain hemispheres and reported here as the average per mouse. In the case that damage to one side prevented accurate counting and averaging, counts from the intact side were reported.

$Rprm^{+}$ projection mapping

To identify brain regions containing downstream $VMHvl^{Rprm}$ fibers, proper targeting of the VMHvl was first confirmed by identifying the presence of EYFP+ cell bodies. Mice that did not have correct targeting were excluded from subsequent analysis. Proper targeting was confirmed for 14 mice. Next, a thorough scan across the brain was conducted to decipher downstream projections. After noting the areas with prominent fluorescent signal during this initial scan, sections containing EYFP+ fibers were then imaged at 20x magnification. We also assessed the presence of $Rprm^{+}$ fibers in various thermoregulatory ROIs, including the periaqueductal gray (PAG), dorsal nucleus raphe (DR), and nucleus raphe pallidus (RPA). An ROI was considered positive for $Rprm^{+}$ projections based on the presence of EYFP+ fibers with fluorescence above background. Gross quantification was assessed and reported as the number of mice out of the 14 correctly targeted ones in which EYFP+ signal was identified for a given ROI. The presence of $Rprm^{+}$ fibers was assessed in both males (n = 9) and females (n = 5), with similar projection

patterns identified. Of note, in some instances, EYFP+ cell bodies (one/two or more) were identified in the Tu, ARH and DMH, but projection patterns did not differ between these mice and those with cell bodies restricted to the VMHvl. The AAV was delivered at doses of 25-50 nL with similar projection patterns observed across doses. Projection intensities were not quantified given the variability in AAV dose.

Statistical Analysis

Statistical analyses and plots were generated in GraphPad Prism (version 11.0.2). Information on statistical tests used, sample sizes, and significance levels are reported in the figure legends. Comparisons between two groups were tested using unpaired *t*-tests. Comparisons involving multiple factors were conducted via 2-way analyses of variance (ANOVA), or in the case data was missing, a mixed effects model, with either repeated measures (RM) or independent factors. Pairwise comparisons were performed following a significant interaction using Šídák's multiple comparison test. Fisher's LSD test was used to compare hM3Dq-expressing and control mice in 2x2 analyses of variance. Simple linear regression analyses were used to calculate rate of change for activity levels. All statistical analyses were two-tailed. Data were considered statistically significant when p is less than 0.05.

Chapter 4: Temporally and spatially distinct approaches to knockout *Rprm* expression in the brain reveal context-dependent roles

INTRODUCTION

Hypothalamic neuronal populations and the gene markers defining them are often treated as interchangeable, but they do not always serve the same functions. Decades of work using lesion studies, hormone replacement, hormone receptor ablation, and more recently, systems neuroscience approaches, have established the VMHvl as a critical node for the control of reproduction, metabolism, thermoregulation, and social behaviors. Whether these diverse VMHvl functions arise from the activity of specific neuronal subpopulations or the genes defining them, remains unknown. More recently, advances in genetic and molecular tools have enabled increasingly precise interrogation of VMHvl cellular diversity, allowing investigators to manipulate genetically defined neuronal populations and determine their contributions to specific aspects of VMHvl-mediated physiology and behavior (Correa et al., 2015; Kim et al., 2019; Krause et al., 2021; Oliveira et al., 2025; van Veen et al., 2020; Yin et al., 2022). Beyond assigning function to distinct cell populations, these approaches provide an opportunity to test whether the genes that define individual VMHvl cell types serve functional roles themselves, rather than acting solely as molecular markers. Such studies can reveal how specific genes contribute to the unique physiological properties of each population and help determine which components of VMHvl function arise from the molecular programs that distinguish one cell type from another.

While the behavioral and metabolic functions of the VMHvl are often studied independently, they are inextricably linked, offering an opportunity to develop a more integrated understanding of the crosstalk between energy balance and behavior. In the previous chapter, we demonstrated that the chemogenetic activation of VMHvl^{Rprm} neurons is sufficient to induce a long-lasting arousal state characterized by hyperthermia and hyperactivity. In this study, we leverage the expression of Flippase recognition target (FRT) sites in our *Rprm*$^{Cre\text{-}FRT}$ mouse model combined with breeding schemes and viral tools, to specifically assess the contribution of

the *Rprm* gene in modulating this arousal state and identify thermoregulatory contexts that it regulates. To do so, we knocked out *Rprm* expression using two approaches differing in developmental timing (embryonic vs. adult) and spatial specificity (whole CNS vs VMHvl) and assess the downstream thermoregulatory processes affected.

We find that knocking out *Rprm* gene expression in glutamatergic (*Vglut2*-expressing) neurons throughout the CNS beginning in embryonic development does not affect the metabolic profiles of adult female mice as determined via measures of body weight, body composition, and food intake at thermoneutrality (29-30 °C), standard housing conditions (22-23 °C), and a substantial cold challenge (15 °C). Further, these mice display a mild attenuation of core body temperature (T_c) only in standard ambient temperatures but not during a substantial cold challenge or at thermoneutrality. Mice that instead carry a VMHvl-specific *Rprm* knockout in adulthood have intact T_c and activity levels at standard housing conditions but display a context-dependent hyperthermia characterized by hyperactivity and impaired habituation that uniquely arises during the presentation of a novel object but not during acute confinement, social interactions, or at baseline. These studies demonstrate the power of dissecting the physiological contributions of neuronal populations and the genes that define them to understand how molecular diversity shapes hypothalamic circuits, their function, and animal behavior.

RESULTS

Knocking out *Rprm* in *Vglut2*$^+$ cells subtly alters T_c in female mice

Given the known role of brain-wide vesicular glutamate transporter 2 (*Vglut2*)-expressing neurons in T_c regulation (Abbott and Saper, 2017; Machado et al., 2018; Yu et al., 2016), our first knockout approach aimed to broadly assess whether *Rprm* influences the thermoregulatory capacity of *Vglut2*$^+$ neurons. To do so, we generated *Rprm*$^{Vglut2\text{-}FlpO}$ mice using mouse genetics and breeding schemes (**Figure S4.1, top**). During mouse brain development, *Rprm* expression

peaks before birth (embryonic day 18.5), at which point *Vglut2* expression is also detectable (Allen Institute for Brain Science developing mouse brain, ISH data, entrez ID: 140919; Thompson et al., 2014). Thus, with this approach, *Rprm* KO occurs in embryonic development in *Vglut2*$^{+}$ neurons throughout the CNS. We then utilized ISH to detect, quantify, and validate the efficacy of this knockout approach. Compared to controls, *Rprm*$^{Vglut2\text{-}FlpO}$ females displayed a significant reduction of approximately 79% in the number of *Rprm*$^{+}$ cells within the VMHvl (Šídák's multiple comparisons test following significant interaction, $t_{20} = 16.23$, $p < 0.0001$; **Figure 4.1A, B**) but not the ARH ($t_{20} = 0.4807$, $p = 0.8675$), in line with the VMHvl being predominantly glutamatergic (Cheung et al., 2015; Hashikawa et al., 2017; Krause and Ingraham, 2017; Tong et al., 2007; van Veen et al., 2020). While these two regions were chosen to validate *Vglut2*-specific *Rprm* gene knockout, they do not represent the full extent of the knockout, which is expected to impact all *Vglut2*-expressing cells that co-express *Rprm*. With the knockout validated, we next assessed whether these mice had altered thermoregulatory profiles.

When single-housed at standard ambient temperature conditions (22-23 °C) from weaning age, adult *Rprm*$^{Vglut2\text{-}FlpO}$ females displayed minor changes in energy expenditure with a mild yet sustained reduction in T_c (main effect of group: $F(1, 17) = 4.973$, $p = 0.0395$; **Figure 4.1C-E**), and no effects on gross motor activity (GMA) (**Figure 4.1F-H**). Assessment of body weight revealed a subtle reduction in *Rprm*$^{Vglut2\text{-}FlpO}$ females compared with *Rprm*$^{FRT/FRT}$ control mice (group x age interaction: $F(14,287) = 1.771$, $p = 0.0424$; **Figure 4.1I**). However, no differences in fat and lean mass percentage (**Figure 4.1J, K**) or food intake (**Figure 4.1L**) were detected.

Mice that are single housed at standard temperatures are chronically cold stressed, needing to expend anywhere from 1.6-3.1 times their basal metabolic rate on non-shivering thermogenesis to maintain body temperature (Cannon and Nedergaard, 2011; Hylander et al.,

2023; Robbins et al., 2018). Thus, given the subtle differences in T_c we detected at standard temperatures, we wondered whether these mildly cold ambient temperatures (22-23 °C) could be masking any metabolic effects of the *Rprm* KO model. To address this concern, metabolic profiles were assessed in mice housed at thermoneutrality (29-30 °C), the ambient temperature at which mice do not need to expend extra energy to maintain T_c (Škop et al., 2020). When housed at thermoneutrality for 2 weeks, no significant differences in T_c (**Figure 4.2A-C**), GMA (**Figure 4.2D-F**), body weight (**Figure 4.2G**), body composition (**Figure 4.2H, I**) or food intake (**Figure 4.2J**) were detected between $Rprm^{Vglut2\text{-}FlpO}$ knockout and $Rprm^{FRT/FRT}$ control mice.

Lastly, we aimed to decipher whether the T_c reductions observed at standard ambient temperatures became exacerbated during a more pronounced cold exposure. To test this, female mice were housed at 15 °C for one week, representing a substantial and sustained cold challenge in single-housed mice. While statistically significant differences in T_c between $Rprm^{Vglut2\text{-}FlpO}$ knockout and $Rprm^{FRT/FRT}$ control mice were detected (group x time interaction: $F(170,1020) = 1.399$, $p = 0.0013$; **Figure 4.3A-C**), the effects of the knockout at 15 °C were much more subtle than those seen at 22-23 °C. Further, GMA (**Figure 4.3D-F**), body weight (**Figure 4.3G**), and the change (Δ) in body weight following a week of cold exposure (Figure S4.1H) were indistinguishable between $Rprm^{Vglut2\text{-}FlpO}$ knockout and $Rprm^{FRT/FRT}$ control mice.

Thermoregulation is unaffected in $Rprm^{AAV\text{-}FlpO}$ knockout female mice at standard housing conditions

The use of breeding schemes to generate mice harboring a gene knockout beginning in embryonic development carries with it limitations that must be considered when interpreting results. For instance, eliminating *Rprm* early in an animal's life can cause compensatory mechanisms to step in, making it difficult to decipher whether any observed mild T_c effects are due to the absence of the gene itself or the activity of the compensatory circuit. Furthermore, given the expression pattern of *Rprm*, this specific approach results in the elimination of *Rprm* throughout the CNS, hindering our ability to pinpoint the effects to a specific node. To address

these limitations, we turned to a second *Rprm* knockout strategy. For this approach, we gained temporal and spatial specificity using stereotaxic delivery of AAV-FlpO to knock out *Rprm* in adult $Rprm^{Cre\text{-}FRT}$ mice within the VMHvl (generating $Rprm^{AAV\text{-}FlpO}$ mice, **Figure S4.1, bottom**). $Rprm^{AAV\text{-}FlpO}$ females showed significant reductions (approximately 91% averaged across both hemispheres) in the number of $Rprm^{+}$ cells within the VMHvl (Šídák's multiple comparisons test following significant interaction: $t_{42} = 12.62$, $p < 0.0001$, left hemisphere; $t_{42} = 16.86$, $p < 0.0001$, right hemisphere; **Figure 4.4A, B**) and the adjacent tuberal nucleus (Tu) (Šídák's multiple comparisons test: $t_{42} = 4.358$, $p = 0.0002$, left hemisphere; $t_{42} = 4.523$, $p = 0.0001$, right hemisphere), but not the ARH (Šídák's multiple comparisons test: $t_{42} = 0.1351$, $p = 0.9988$, left hemisphere; $t_{42} = 1.340$, $p = 0.4634$, right hemisphere). Thus, $Rprm^{AAV\text{-}FlpO}$ mice carry an adult-specific *Rprm* knockout that is spatially restricted, enabling us to specifically assess *Rprm* function within the VMHvl thermoregulatory node. With the knockout validated, we next investigated whether these mice had altered thermoregulatory profiles.

At standard housing conditions, $Rprm^{AAV\text{-}FlpO}$ females displayed unaltered T_c (group x time interaction: $F (23, 322) = 0.9031$, $p = 0.5947$; **Figure 4.4C, D**) and GMA (group x time interaction: $F (23, 322) = 0.8118$, $p = 0.7165$; **Figure 4.4E, F**), indicating that adult expression of $VMHvl^{Rprm}$ is largely dispensable for thermoregulation at standard ambient temperatures. The different thermal profiles induced in $Rprm^{Vglut2\text{-}FlpO}$ vs $Rprm^{AAV\text{-}FlpO}$ knockout females at standard housing conditions may point to a potential, but mild, thermoregulatory role for *Rprm* beyond the VMHvl and/or in the development of thermoregulatory circuits.

Female $Rprm^{AAV\text{-}FlpO}$ knockout mice display an enhanced hyperthermia in response to novel object presentation

The lack of thermoregulatory effects in $Rprm^{AAV\text{-}FlpO}$ mice at standard housing conditions pointed to the idea that the effects of eliminating *Rprm* expression may be context dependent. The amygdala is a central node involved in the processing of sensory, social, and environmental cues critical for survival, it is often linked with the induction of a stress response (Aukema et al.,

2025; Dalooei et al., 2016; Phelps and LeDoux, 2005; Roozendaal et al., 2009; Sajdyk et al., 2008) and an associated hyperthermic state (Sajdyk et al., 2008; Vinkers et al., 2010) often termed psychogenic fever or stress-induced hyperthermia (SIH) (Adriaan Bouwknecht et al., 2007; Nakamura, 2015; Oka, 2018, 2015; Vinkers et al., 2009b; Zethof et al., 1994). Prominent VMHvl^{Rprm} neuronal projections throughout the amygdala and extended amygdala (Chapter 3, **Figure 3.4**) led us to investigate the potential contribution of VMHvl^{Rprm} gene function in the SIH response. To do so, *Rprm*$^{AAV\text{-}FlpO}$ knockout and *Rprm*$^{FRT/FRT}$ control females were subjected to behavioral assays where they were exposed to a series of social and environmental stimuli (**Figure 4.5A**). The selected SIH assays include: 1) novel object presentation, 2) social interaction with a conspecific female or male, and 3) confinement (Adriaan Bouwknecht et al., 2007; Harshaw et al., 2021; McGivern et al., 2009; Oka, 2018, 2015). To accurately assess and interpret alterations in T_c and GMA that are specifically mediated by these stimuli, and to distinguish from changes induced by handling stress, mice were thoroughly habituated by mimicking assay conditions minus the stimuli (**Figure S4.2A-D**). Further, all manipulations were done in the home cage to minimize perturbations that occur when transferring mice to behavioral testing chambers.

While both *Rprm*$^{AAV\text{-}FlpO}$ and control mice displayed a hyperthermic response in all assays (**Figure 4.5B-E**), notable differences in the magnitude of the hyperthermia were identified during novel object presentation. *Rprm*$^{AAV\text{-}FlpO}$ mice maintained higher T_c compared with controls throughout the assay (group x time interaction: $F(39,546) = 2.278$, $p < 0.0001$; **Figure 4.5B**). These differences are further highlighted when comparing ΔT_c from baseline ($t_{14} = 2.486$, $p = 0.0262$; **Figure 4.5J**). We also assessed GMA to determine whether this enhanced hyperthermia was associated with increased locomotor reactivity to novelty, which is interpreted as increased exploratory behavior (Lustberg et al., 2020). We similarly found that *Rprm*$^{AAV\text{-}FlpO}$ mice were more active throughout the assay when compared with controls (group x time

interaction: F (39, 546) = 1.896, p = 0.0011; **Figure 4.5F**) and showed higher ΔGMA (t_{14} = 3.275, p = 0.0055; **Figure 4.5K**). Simple linear regression analysis of activity counts over time (**Figure 4.5L**) revealed that variation in GMA was more strongly predicted time in control mice (R^2 = 0.4352) than in *Rprm*$^{AAV\text{-}FlpO}$ mice (R^2 = 0.1249). Fit lines from *Rprm*$^{AAV\text{-}FlpO}$ mice had a flatter slope (F (1,140) = 4.192, p = 0.0425), indicating slower habituation to novelty (Lustberg et al., 2020). Corroborating this, *Rprm*$^{AAV\text{-}FlpO}$ mice showed a lower rate of decline from peak to basal levels (t_{14} = 2.920, p = 0.0112; **Figure 4.5M**). While both groups showed similar initial responses to novelty, as indicated by comparable peak GMA levels during the first 5-min of the assay (t_{14} = 0.1382, p = 0.8920; **Figure 4.5N**), *Rprm*$^{AAV\text{-}FlpO}$ mice maintained higher activity levels than controls by the end of the assay (t_{14} = 3.055, p = 0.0086; **Figure 4.5O**). Behaviorally, following the initial presentation of the object, control mice appeared to return to a resting state whereas *Rprm*$^{AAV\text{-}FlpO}$ mice continued to move around the cage until the object was removed (**Figure 4.5P**). No differences in T_c or activity were identified across the other SIH paradigms tested (**Figure 4.5G-I**). These results reveal a role for *Rprm* in novelty-induced hyperthermia, characterized by heightened gross motor activity and blunted habituation to a novel object, that may be modulated independently to the hyperthermia elicited by social interaction and canonical restraint stress. This establishes a previously unknown role for the estrogen-sensitive VMHvl that links well-known effects on thermogenesis and movement to behavioral states.

DISCUSSION

Developmental *Rprm* knockout in *Vglut2* lineage cells

Here, we leverage the expression of Flippase recognition target (FRT) sites in our *Rprm*$^{Cre\text{-}FRT}$ mouse model combined with breeding schemes and mouse genetics to specifically eliminate *Rprm* expression in excitatory *Vglut2*$^+$ cells. The thermoregulatory role of *Vglut2*$^+$ cells in the brain has been well established, with the ability of certain populations in the preoptic area to induce hypothermia (Abbott and Saper, 2017; Yu et al., 2016), and others in the dorsal

hypothalamic area to induce hyperthermia (Machado et al., 2018). Thus, we aimed to specifically assess the contribution of the *Rprm* gene in modulating the thermoregulatory capacity of *Vglut2*$^{+}$ neurons in the brain.

We find that under both ambient conditions of minimal thermogenic demand (29-30 °C) and a substantial cold challenge (15 °C), *Rprm* is largely dispensable for T_c regulation. However, under mild cold conditions (22-23 °C), *Rprm*$^{Vglut2\text{-}FlpO}$ knockout mice display a subtle blunting of T_c compared to controls. These results may point to a potential mechanistic model in which rather than setting basal thermogenic capacity (at thermoneutrality) or near-maximal cold-defense output (during a cold challenge), *Rprm* in *Vglut2*-lineage cells may function as part of a fine central thermoregulatory system that becomes important under conditions of moderate sustained thermogenic demand (standard housing) to maintain T_c. More detailed study is required to test this possibility under conditions of developmental knockout.

Adult-specific *Rprm* knockout in the VMHvl

While *Rprm* is expressed in healthy tissues in mice (Park et al., 2026), most reports on *Rprm* function have focused on its pathophysiological function in cancerous tissues, emphasizing its tumor-suppressing abilities as a p53 target gene (Li et al., 2022; Ohki et al., 2000; Takikawa and Ohki, 2025; Ye et al., 2023; Zhang et al., 2022). Here, we interrogate *Rprm* in the healthy brain, specifically within the VMHvl, to assess its thermoregulatory role and identify the contexts critically regulated by this population. We find that *Rprm* expression in the VMHvl of adult female mice is dispensable for T_c regulation at standard housing conditions, with *Rprm*$^{AAV\text{-}FlpO}$ knockout and control mice having indistinguishable temperature profiles. This prompted us to investigate whether the functions of *Rprm* were context dependent. The identification of *Rprm*$^{+}$ fibers within various amygdalar nuclei (Chapter 3) led us to examine the potential contribution of VMHvl^{Rprm} gene function in the SIH response.

In rodents, adaptive behavioral and physiological responses to novelty, which may represent a potential threat or an attractive opportunity, often include an initial anxiety-like behavior, referred to as neophobia that manifests as freezing, avoidance, and hesitant movement, that is then followed by intense exploration and increased activity levels, referred to as neophilia, that gradually subsides to basal levels as the mice habituate to novelty (Lustberg et al., 2020). Our sequence of behavioral assays identified an unexpected role for VMHvl^{Rprm} gene expression in the regulation of these responses to novelty, characterized by novelty-induced changes in GMA, habituation, and T_c. This finding extends previous work showing that female mice lacking glutamatergic signaling in the VMH display heightened novelty-associated locomotion and reduced levels of anxiety-like behaviors (Cheung et al., 2015), identifying a novel link between the behavioral roles of the VMH and thermoregulation.

Female-specific *Rprm* expression within VMHvl suggests that novelty-induced hyperthermia may also have sex-specific functions. Interestingly, C57BL/6 females display higher locomotor responses to novelty than males (Archer, 1975; Seney et al., 2012; Van Swearingen et al., 2013). Additionally, this sex difference is influenced by both organizational and activational effects of hormones (Seney et al., 2012), similar to how sex differences in *Rprm* expression are established by estrogen signaling early in life (van Veen et al., 2020). Our findings suggest that *Rprm* limits the magnitude of novelty-induced physiological responses in females. However, this does not imply males with little to no *Rprm* in the VMHvl should phenocopy *Rprm*-deficient females. We have previously shown that *Rprm* gene knockdown in males does not affect T_c or GMA, thus we favor a model in which ERα signaling establishes a sex-specific molecular program in VMHvl neurons that includes female-specific *Rprm* expression (van Veen et al., 2020). In adults, *Rprm* does not determine the existence of novelty-responsive circuitry, as evidenced by the capacity for hyperthermia when activating *Rprm*$^+$ cells

in both sexes, but instead constrains the magnitude and persistence of the response in females, as demonstrated by *Rprm* KO in adult females.

Here we show that loss of *Rprm* gene expression in the VMHvl of females leads to an enhanced hyperthermia arising from heightened gross motor activity and diminished habituation in response to novel object presentation. This finding suggests the intriguing possibility that the role of *Rprm* in responses to novelty is related to the long-established roles of the VMHvl in females in regulating glucose (Hirschberg et al., 2020; Su et al., 2025; Tu et al., 2022), promoting arousal (Devidze et al., 2006; Krause et al., 2021), suppressing anxiety (Cheung et al., 2015; Mccarthy et al., 1996), and mediating interactions with threats (Hashikawa et al., 2017; Silva et al., 2013). Recent work also shows that this arousal includes the suppression of excretions (Cabrera-Zapata et al., 2026), suggesting that the arousal state comprises multiple components that may be driven by distinct aspects of cellular or circuit function. Indeed, the increase in physical activity is driven by the *Mc4r* gene (Krause et al., 2021), the suppression of secretions by neural projections to a micturition center (Cabrera-Zapata et al., 2026), and the suppression of physiological responses to novelty by the *Rprm* gene.

More broadly, these findings define the specific context-dependent contributions of *Rprm* gene function and place them within the broader thermoregulatory and behavioral functions of the VMHvl. Such studies are imperative to fully understand how molecularly diverse populations coordinate function.

FIGURES

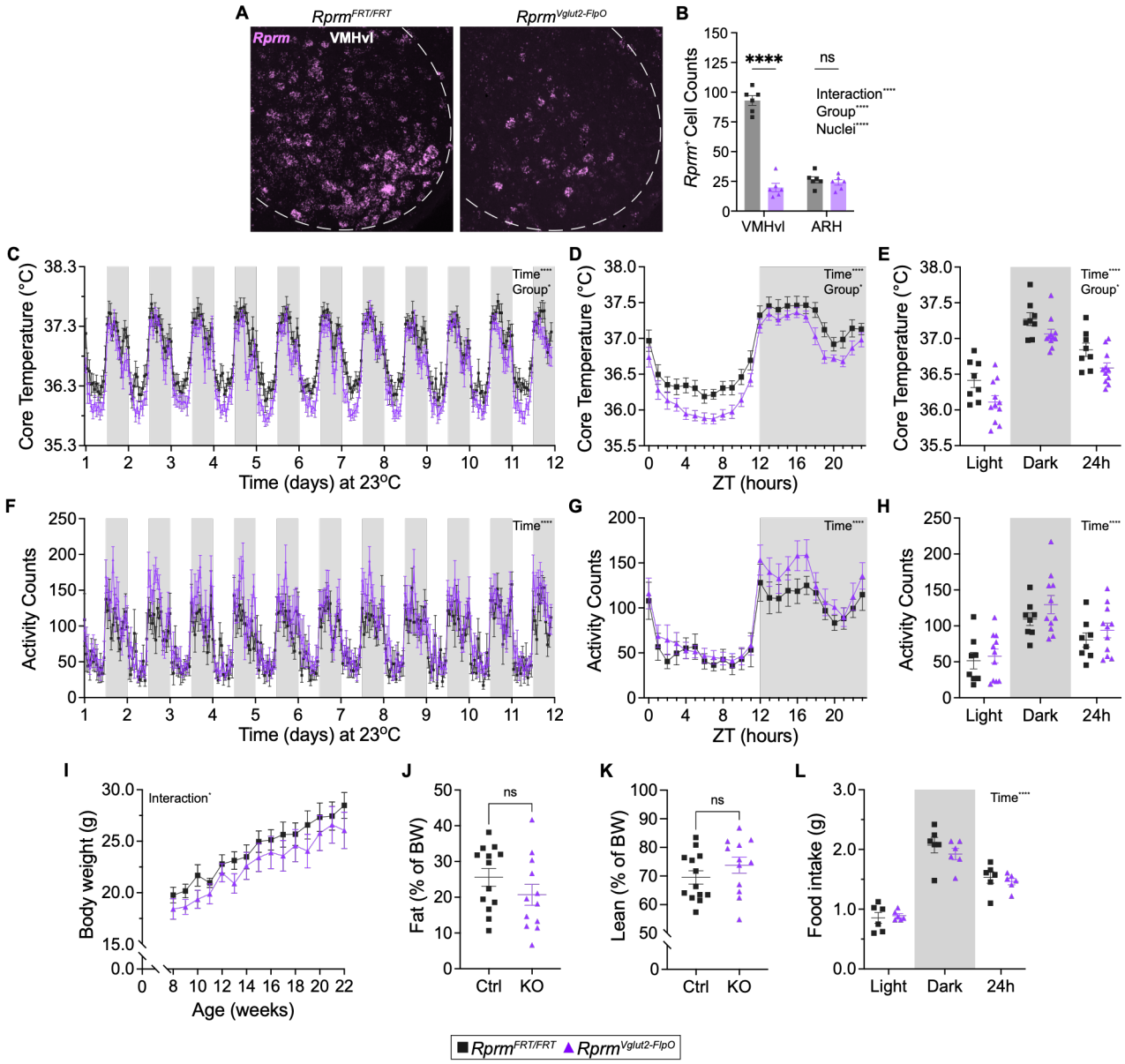


Figure 4.1: Female mice harboring a *Rprm* KO in *Vglut2*-lineage cells display mild alterations to T_c when housed in standard ambient temperatures (22-23 °C)

(A) Representative images of the VMHvl following single molecule *in situ* hybridization to label *Rprm* (lavender) in *Rprm*$^{FRT/FRT}$ control and *Rprm*$^{Vglut2\text{-}FlpO}$ knockout female mice; scale bars = 100 μm. (B) Quantification of *Rprm*$^{+}$ cells in 20 μm coronal sections from *Rprm*$^{FRT/FRT}$ control (black squares, *n* = 6) and *Rprm*$^{Vglut2\text{-}FlpO}$ knockout (purple triangles, *n* = 6) female mice. Pairwise comparisons were performed using Šídák's multiple comparison test following a

significant interaction in an ordinary two-way ANOVA. (C) Hourly T_c recordings throughout the 11-day session in adult (9-19 weeks of age) *Rprm*$^{FRT/FRT}$ control (black squares, *n* = 8) and *Rprm*$^{Vglut2\text{-}FlpO}$ knockout (purple triangles, *n* = 11) female mice with mean ± SEM. (D) Average 24-hour T_c trace for the 11-day session for mice in (C) with mean ± SEM. (E) 12- and 24-hour T_c averages from (C) with mean ± SEM and data points for each mouse. (F) Hourly GMA recordings throughout the 11-day session presented with mean ± SEM for mice in (C). (G) Average GMA from (F) across an 11-day recording session presented with mean ± SEM. (H) 12- and 24-hour GMA averages from (F) presented with mean ± SEM and data points for each mouse. Statistical analyses for (C to H) performed using a two-way RM ANOVA. (I) Body weight was tracked weekly from 8 to 22 weeks of age (*Rprm*$^{FRT/FRT}$ control mice in black squares, *Rprm*$^{Vglut2\text{-}FlpO}$ knockout mice in purple triangles; *n* = 7-14 at each age) and displayed with mean ± SEM. Statistical analysis performed using a mixed effects model with Restricted Maximum Likelihood (REML) due to missing values and pairwise comparisons performed using Šídák's multiple comparison test following a significant interaction. (J) fat mass and (K) lean mass as percentages of total body weight were calculated in adult (22-weeks of age) female mice (*Rprm*$^{FRT/FRT}$ control mice, *n* = 13; *Rprm*$^{Vglut2\text{-}FlpO}$ knockout mice, *n* = 12). Statistical analyses were performed using unpaired *t*-tests and displayed with mean ± SEM and data points for each mouse. (L) Average food intake in adult female mice (15-23 weeks of age; *Rprm*$^{FRT/FRT}$ control mice in black squares, *Rprm*$^{Vglut2\text{-}FlpO}$ knockout mice in purple triangles; *n* = 6 per group) presented with mean ± SEM and data points for each mouse. Statistical analysis was performed using a two-way RM ANOVA. For all data, **p* < 0.05, ***p* < 0.01, ****p* < 0.001, *****p* < 0.0001, and ns = not significant. VMHvl = ventrolateral subdivision of the ventromedial nucleus of the hypothalamus.

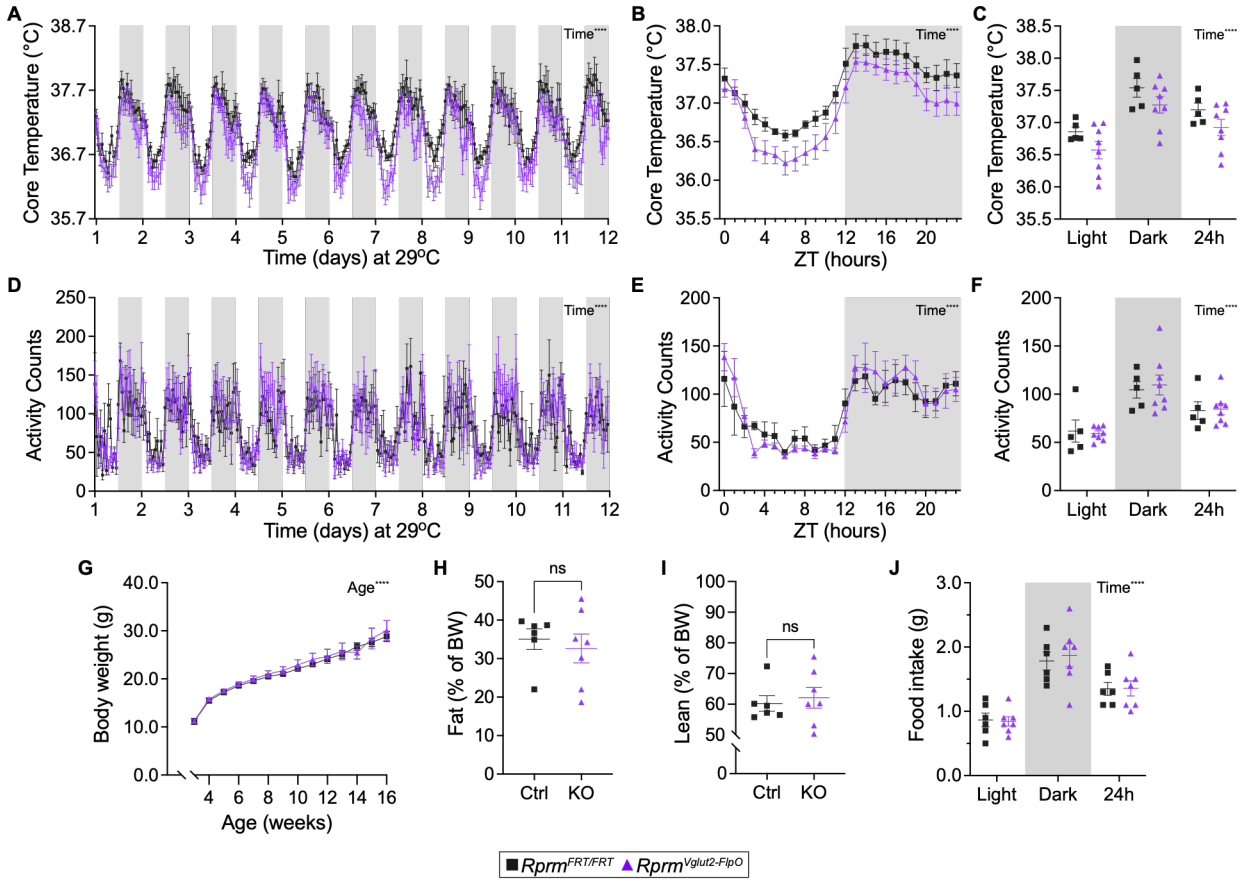


Figure 4.2: Female mice harboring a *Rprm* KO in *Vglut2*-lineage cells have unaltered T_c when housed at thermoneutrality (29-30 °C)

(A) Hourly T_c recordings throughout the 11-day session in adult (21-27 weeks of age) *Rprm*$^{FRT/FRT}$ control (black squares, *n* = 5) and *Rprm*$^{Vglut2\text{-}FlpO}$ knockout (purple triangles, *n* = 8) female mice with mean ± SEM. (B) Average 24-hour T_c trace for the 11-day session for mice in (A) with mean ± SEM. (C) 12- and 24-hour T_c averages from (A) with mean ± SEM and data points for each mouse. (D) Hourly GMA recordings throughout the 11-day session presented with mean ± SEM for mice in (A). (E) Average GMA from (D) across an 11-day recording session presented with mean ± SEM. (F) 12- and 24-hour GMA averages from (D) presented with mean ± SEM and data points for each mouse. Statistical analyses for (A to F) performed using a two-way RM ANOVA. (I) Body weight was tracked weekly from 3 to 16 weeks of age (*Rprm*$^{FRT/FRT}$ control mice in black squares, *Rprm*$^{Vglut2\text{-}FlpO}$ knockout mice in purple triangles; *n* =

7-8 at each age) and displayed with mean ± SEM. Statistical analysis performed using a mixed effects model with Restricted Maximum Likelihood (REML) due to missing values. (J) fat mass and (K) lean mass as percentages of total body weight were calculated in adult (18-23 weeks of age) female mice (*Rprm*$^{FRT/FRT}$ control mice, $n = 6$; *Rprm*$^{Vglut2\text{-}FlpO}$ knockout mice, $n = 7$). Statistical analyses were performed using unpaired *t*-tests and displayed with mean ± SEM and data points for each mouse. (L) Average food intake in mice from (J, K) presented with mean ± SEM and data points for each mouse. Statistical analysis was performed using a two-way RM ANOVA. For all data, *$p < 0.05$, **$p < 0.01$, ***$p < 0.001$, ****$p < 0.0001$, and ns = not significant.

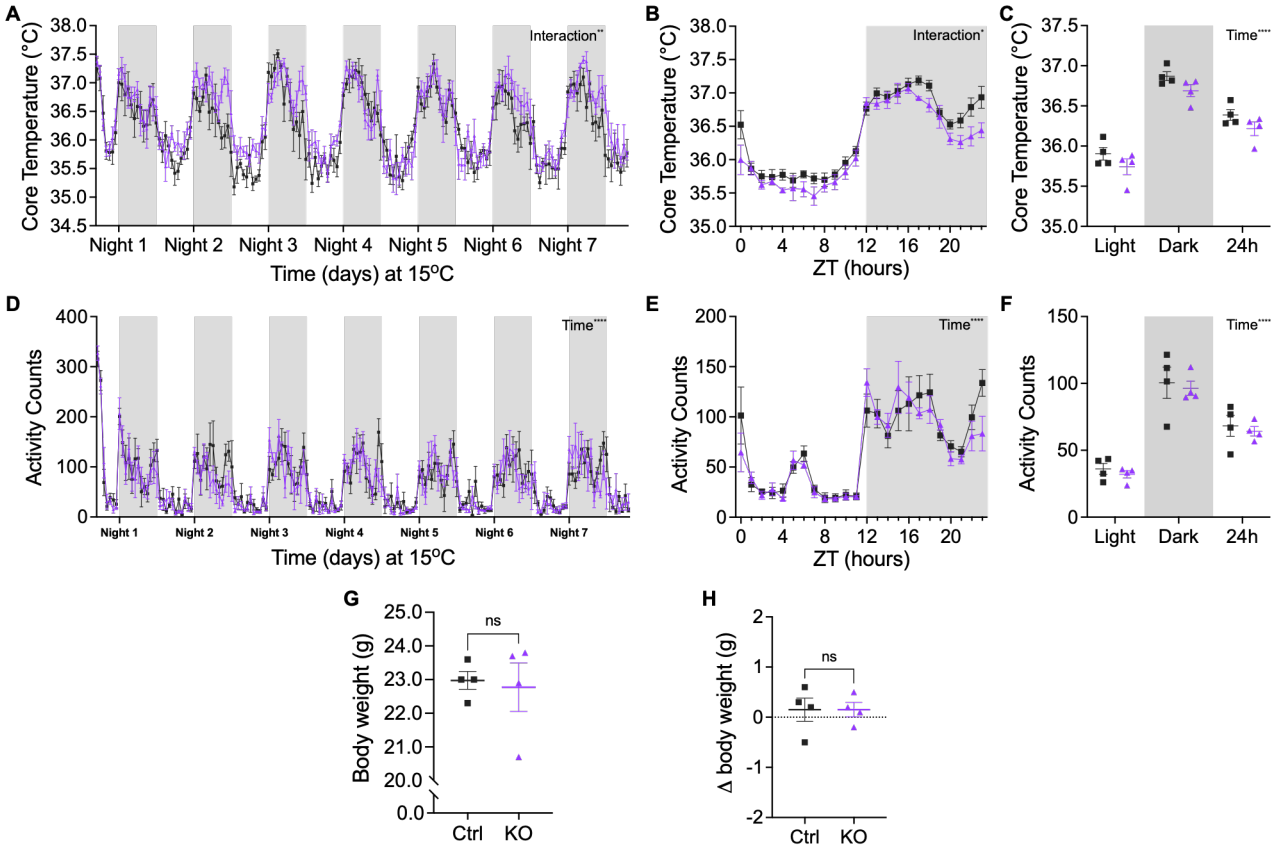


Figure 4.3. Female mice harboring a *Rprm* KO in *Vglut2*-lineage cells have unaltered T_c when exposed to a substantial cold challenge (15 °C)

(A) Hourly T_c recordings throughout the 7-day session in adult (11-15 weeks of age) $Rprm^{FRT/FRT}$ control (black squares, n = 4) and $Rprm^{Vglut2\text{-}FlpO}$ knockout (purple triangles, n = 4) female mice with mean ± SEM. (B) Average 24-hour T_c trace for the 7-day session for mice in (A) with mean ± SEM. (C) 12- and 24-hour T_c averages from (A) with mean ± SEM and data points for each mouse. (D) Hourly GMA recordings presented with mean ± SEM for mice in (A). (E) 7-day average GMA from (D) presented with mean ± SEM. (F) 12- and 24-hour GMA averages from (D) presented with mean ± SEM and data points for each mouse. Statistical analyses for (A to F) performed using a two-way RM ANOVA. (G) Final body weight and (H) change (Δ) in body weight from baseline after 15 °C exposure. Statistical analysis performed using unpaired *t*-tests and displayed with mean ± SEM and data points for each mouse. For all data, *p < 0.05, **p < 0.01, ***p < 0.001, ****p < 0.0001, and ns = not significant.

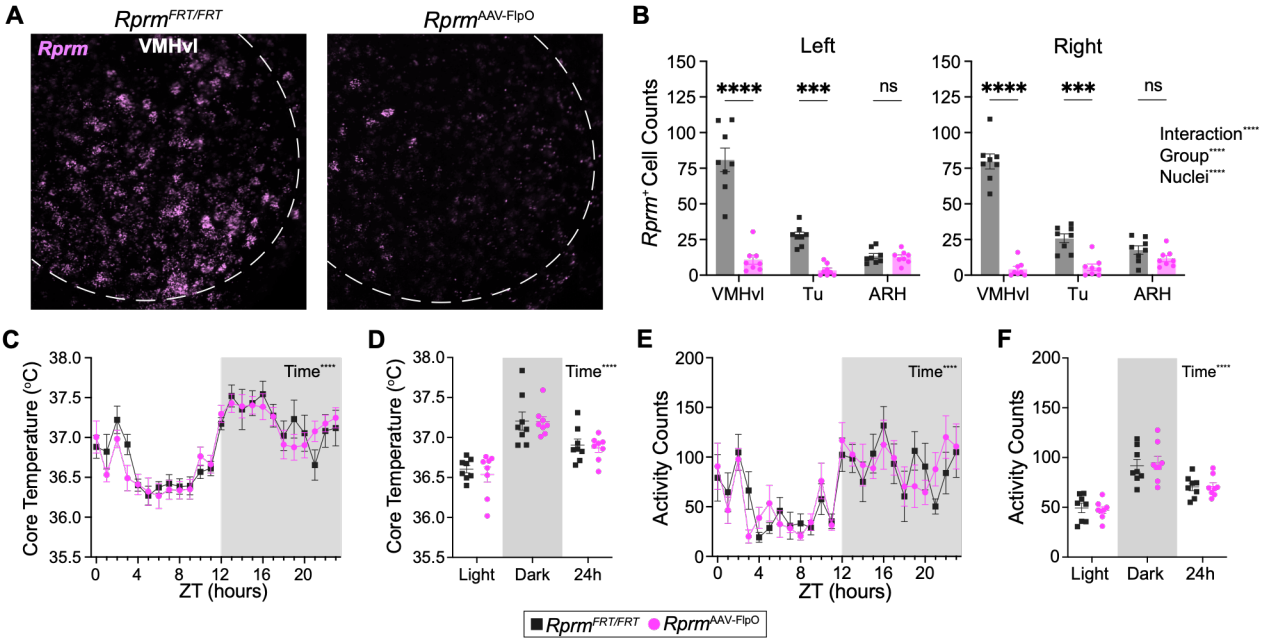


Figure 4.4: Female mice harboring an adult-specific *Rprm* KO in the VMHvl have unaltered T_c at standard ambient temperatures (22-23 °C)

(A) Representative images of the VMHvl following single molecule *in situ* hybridization labeling *Rprm* (lavender) in *Rprm*$^{FRT/FRT}$ control and *Rprm*$^{AAV\text{-}FlpO}$ knockout female mice; scale bars = 100 μm. (B) Quantification of *Rprm*$^{+}$ cells in 20 μm coronal sections from *Rprm*$^{FRT/FRT}$ control (black squares, n = 8) and *Rprm*$^{AAV\text{-}FlpO}$ knockout (pink circles, n = 8) female mice. Pairwise comparisons were performed using Šídák's multiple comparison test following a significant interaction in an ordinary two-way ANOVA. (C) T_c recorded across a 24-hour period presented as mean ± SEM in adult (14-18 weeks of age) *Rprm*$^{FRT/FRT}$ control (black squares, n = 8) and *Rprm*$^{AAV\text{-}FlpO}$ knockout (pink circles, n = 8) female mice. Spikes in T_c near ZT 2 are due to handling. (D) 12- and 24-hour T_c averages from (C) with mean ± SEM and data points for each mouse. (E) GMA recorded across a 24-hour period and presented as in (C). (F) 12- and 24-hour GMA averages from (E) presented as in (D). Statistical analyses for (C to F) performed via a two-way RM ANOVA. For all data, *p < 0.05, **p < 0.01, ***p < 0.001, ****p < 0.0001, and ns = not significant. VMHvl = ventrolateral subdivision of the ventromedial nucleus of the hypothalamus.

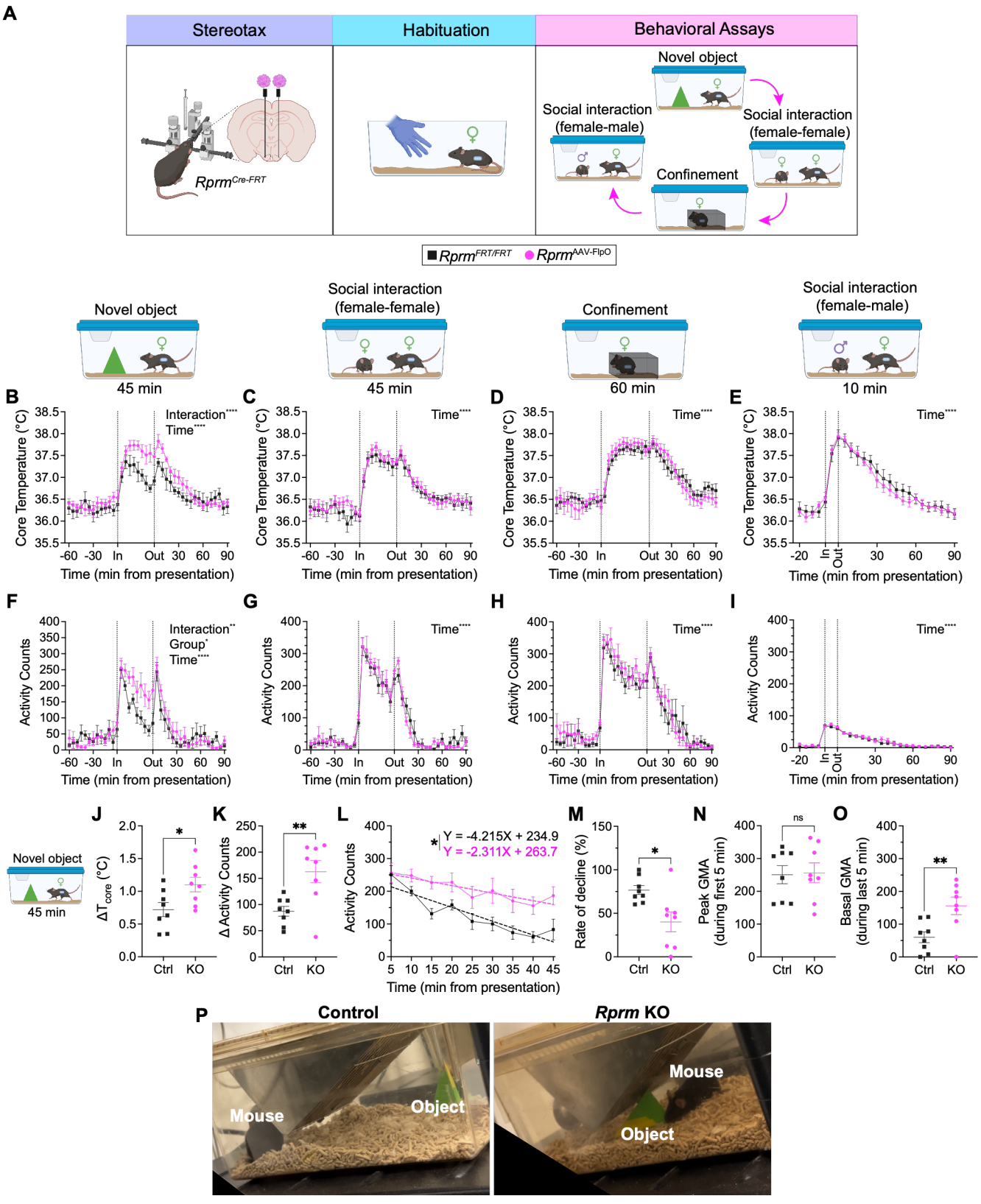

A
Stereotax
Habituation
Behavioral Assays
Rprm Cre-FRT
Novel object
Social interaction (female-male)
Social interaction (female-female)
Confinement
Rprm FRT/FRT
Rprm AAV-FlpO
Novel object
45 min
Social interaction (female-female)
45 min
Confinement
60 min
Social interaction (female-male)
10 min
B
C
D
E
Core Temperature (°C)
Time (min from presentation)
Interaction****
Time****
F
G
H
I
Activity Counts
Interaction**
Group*
Time****
J
K
L
M
N
O
ΔTcore (°C)
Δ Activity Counts
Y = -4.215X + 234.9
Y = -2.311X + 263.7
Rate of decline (%)
Peak GMA (during first 5 min)
Basal GMA (during last 5 min)
ns
Ctrl
KO
P
Control
Rprm KO
Mouse
Object

Figure 4.5: Female mice harboring an adult-specific *Rprm* KO in the VMHvl display an enhanced hyperthermia in response to novel object presentation

(A) Experimental design to decipher the role of VMHvl^{Rprm} gene expression across an array of behavioral assays. (B to E) 5-min T_c recordings in adult (14-18 weeks of age) *Rprm*$^{FRT/FRT}$ control (black squares, n = 8) and *Rprm*$^{AAV\text{-}FlpO}$ knockout (pink circles, n = 8) female mice across behavioral assays including: (B) novel object presentation, (C) female-female social interaction, (D) confinement, and (E) female-male social interaction. Dashed vertical lines indicate the start and end of each assay. Data are displayed as the mean ± SEM with statistical analysis performed using a two-way RM ANOVA. (F to I) 5-min GMA counts across assays presented and analyzed as in (B to E). (J and K) Assessment of (J) ΔT_c and (K) ΔGMA comparing average values the hour before (baseline) vs average values during the novel object presentation assay. Statistical analyses were performed using unpaired *t*-tests with mean ± SEM and data points shown for each mouse. (L) Simple linear regression analysis assessing the rate of change in novelty-induced GMA across the 45-min assay. (M) Rate of GMA decline from peak to basal levels calculated as ((GMA during the initial 5-min – GMA during the last 5-min) / GMA during the initial 5-min) * 100. Statistical analysis was performed using an unpaired *t*-test with mean ± SEM and data points shown for each mouse. (N) Peak activity levels during the first 5-min of the assay. Statistical analysis performed using an unpaired *t*-test with mean ± SEM and data points shown for each mouse. (O) Basal activity levels during the last 5-min of the assay. Statistical analysis performed using an unpaired *t*-test with mean ± SEM and data points shown for each mouse. (P) Representative photographs taken of a control (left) and *Rprm*$^{AAV\text{-}FlpO}$ knockout (right) female mouse during the novel object presentation assay. For all data, *p < 0.05, **p < 0.01, ***p < 0.001, ****p < 0.0001, and ns = not significant.

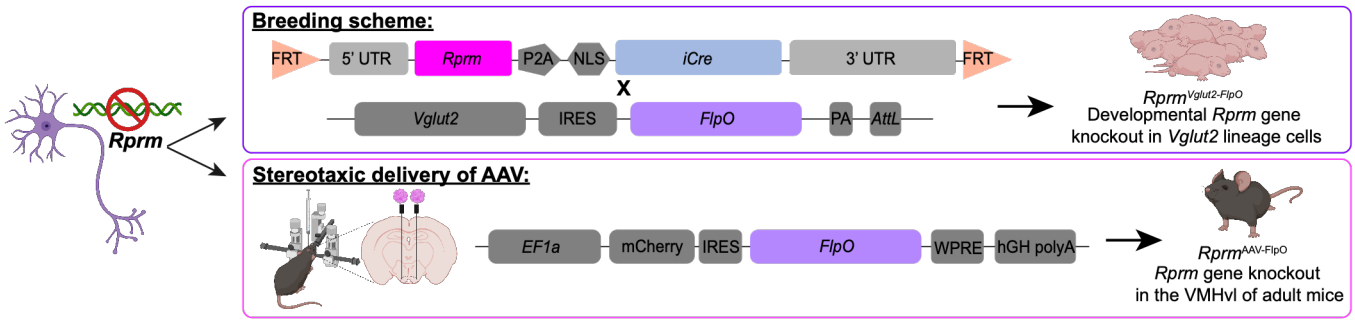


Figure S4.1 related to Figures 4.1-4.5: Schematic of the two approaches used to generate *Rprm* KO mice

Top, breeding schemes and mouse genetics were used to generate *Rprm*$^{Vglut2\text{-}FlpO}$ mice harboring a *Rprm* knockout in *Vglut2* lineage cells throughout the CNS from embryonic development. Bottom, stereotaxic delivery of an AAV-FlpO virus was used to specifically knock out *Rprm* in the VMHvl of adult female mice.

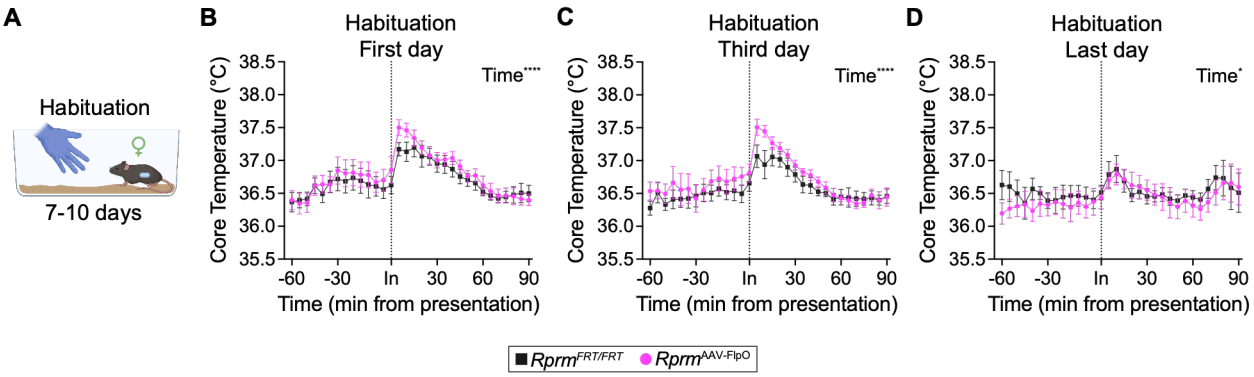


Figure S4.2 related to Figure 4.5: Week-long daily habituation is sufficient to reduce T_c spikes for the assessment of stress-induced hyperthermia

(A) Schematic of habituation approach. Mice were habituated to assay conditions (cage lid and food hopper removal, experimenter, hand in cage mimicking placement of stimulus) for 7-10 days. (B to D) 5-min T_c recordings in adult (14-18 weeks of age) *Rprm*$^{FRT/FRT}$ control (black squares, n=8) and *Rprm*$^{AAV\text{-}FlpO}$ knockout (pink circles, *n* = 8) female mice on the (B) first, (C) third, and (D) last day of habituation. Data are displayed as the mean ± SEM with statistical analysis performed using a two-way RM ANOVA. For all data, **p* < 0.05, ***p* < 0.01, ****p* < 0.001, *****p* < 0.0001, and ns = not significant.

MATERIALS AND METHODS

Mouse models

All procedures were approved by the UCLA Institutional Care and Use Committee (IACUC) in accordance with the National Institutes of Health (NIH) guide for the care and use of laboratory animals and carried out in approved facilities at UCLA. Mice were housed under a 12:12 light-dark cycle (zeitgeber time (ZT) 0 = 7:00 am) under controlled humidity conditions at 22-23 °C ambient temperatures with *ad libitum* access to water and breeder chow (Mouse Diet 9F 5020, 20% protein, 9% fat, LabDiet; St. Louis, MO, USA).

Experiments were performed on gonadally intact adult animals. The sex of a mouse was determined at weaning based on anogenital distance and confirmed postmortem based on the presence of ovaries or testes (Massa et al., 2023). *Rprm*$^{Cre\text{-}FRT}$ founder mice on a C57BL/6J background were bred and maintained in approved conditions at UCLA (Park et al., 2026).

To produce *Rprm*$^{Vglut2\text{-}FlpO}$ mice, a 2-generation breeding scheme was used. First, *Rprm*$^{Cre\text{-}FRT}$ homozygous mice (referred to here as *Rprm*$^{FRT/FRT}$) were bred with *Vglut2*$^{Flpo/+}$ mice (JAX stock no. 030212, B6;129S-*Slc17a6*$^{tm1.1(flpo)Hze}$*/J*) to generate heterozygote carriers of FRT sites and optimized flippase recombinase (Flpo). These mice were then bred with *Rprm*$^{FRT/FRT}$ mice to ultimately generate mice homozygous for FRT sites and heterozygous for Flpo that harbored a developmental *Rprm* knockout in *Vglut2* lineage cells, referred to here as *Rprm*$^{Vglut2\text{-}FlpO}$ mice. This line was maintained via crosses with *Rprm*$^{FRT/FRT}$ mice from the *Rprm*$^{Cre\text{-}FRT}$ colony.

Mouse surgical procedures

For all surgeries, mice were anesthetized with 2-3% isoflurane and administered pain management medications, including buprenorphine (0.01 mg/mL) and carprofen (0.58 mg/mL),

on the day of surgery and the following day. Daily body weight and health monitoring was conducted for at least a week after surgery.

Stereotaxic surgery

Surgeries were performed on adult (8-13 weeks of age) *Rprm*$^{Cre\text{-}FRT}$ female mice. Following anesthetization, mice were placed on a stereotaxic device (Kopf Instruments model 1900) with isoflurane maintained at 2-2.5%. Viruses were targeted to the VMHvl of adult mice using the following coordinates: 1.50 mm posterior to bregma, 0.80-0.85 mm lateral to the midline, and 5.50-5.60 mm below the brain surface. Viruses were delivered at a rate of 5-10 nL/sec using pulled glass needles connected to Hamilton syringes. The needle was slowly removed from the brain 10 min after infusion to allow for viral diffusion. Viruses were delivered bilaterally into the VMHvl except for anterograde tracing studies, where the AAV was unilaterally injected into the left hemisphere. Details on viral titers and injection volumes can be found in **table 1** below. While we targeted the VMHvl for stereotaxic manipulations, viral expression extended to the connecting tuberal nucleus; we include schematics of viral spread and/or quantifications for these experiments.

Experiment	Virus	Depositor and procurement	Titer (vg/mL)	Volume (nL) per hemisphere
Flippase recombinase-mediated *Rprm* KO	AAV1-EF1a-mCherry-IRES-Flpo	Karl Deisseroth, Addgene viral prep # 55634-AAV1	7×10^{12}	75
Fluorescent mCherry control	AAV8-hSyn-DIO-mCherry	Bryan Roth, Addgene viral prep # 50459-AAV8	$\geq 1\times10^{13}$	75

Passive and continuous tracking of core body temperature (T_c)

Implantation of thermo-loggers occurred either on the same day as stereotaxis or one week before/after, depending on availability. In either case, mice were allowed to recover for at

least 2-weeks following surgery before experiments were conducted. For all experiments detailed below, mice were singly housed with *ad libitum* access to food and water for the duration of telemetry recordings, which all occurred in the home cage.

Short-range telemetry was collected via G2 E-Mitters and the ER4000/4500 receiver pads (Starr Life Sciences; Oakmont, PA, USA). This permits the continuous monitoring of T_c and gross motor activity (GMA), defined as movements carried out in the x, y, and z axis including running, walking, rearing, and side-to-side displacements. DST nano-T thermo-loggers (Star-Oddi; Garðabær, Iceland) were also employed for continuous T_c recordings. Both the G2 E-Mitters and nano-T thermo-loggers were implanted intraperitoneally following sterilization with Metricide^{TM}28 Glutaraldehyde High-Level Disinfectant (Metrex Research; Orange, CA, USA) as described in (Raam et al., 2026). At the end of experiments, raw data from G2 E-Mitters and DST nano-T thermo-loggers was extracted using VitalView (version 5.1 & 6.0, Starr Life Sciences) and Mercury (version v6.69, Star-Oddi) data acquisition software, respectively.

T_c analysis

T_c in *Rprm*$^{Vglut2\text{-}FlpO}$ females across various ambient temperatures

Continuous telemetry recordings are presented in one of three ways: 1) 1-hour intervals across the multi-day experiment (11 days for 23 °C and 29 °C, 8 days for 15 °C), 2) averaged across the multi-day recording session at each hour interval and presented as a 24-hour T_c trace or 3) further binned into 12-hour intervals in the light and dark phase and into a 24-hour average.

T_c in *Rprm*$^{AAV\text{-}FlpO}$ females

Following stereotaxic surgery and a 2-week recovery period, mice were subjected to a 7-10-day habituation paradigm before behavioral assays, acclimating them to experimental

conditions and minimizing confounders for T_c analysis. Habituations included removing the cage lid and food hopper, gently introducing the investigator's hand into the cage to mimic the placement of a stimulus, and placing the food hopper and lid back on. All manipulations and telemetry recordings were carried out in the home cage to minimize T_c and GMA perturbations that occur when transferring mice to behavioral testing chambers.

Novelty-induced hyperthermia

3D-printed pyramids (4 x 4 x 6 cm) were made from polylactic acid (PLA) filaments and printed using the Creality Ender-3 V2 3D printer (Inayat et al., 2021). Pyramids were wrapped with bright green and yellow tape (fisherbrand Cat. No. 159015R) to ensure easy visibility and were sanitized prior to and in between each run with Sani-Plex 128 and 70% ethanol. Mice were allowed to freely interact with the object during the 45-min assay.

Social hyperthermia

Sexually naïve conspecific adult (9–10-week-old females & 10–14-week-old males) mice were used as the stimuli. For the female-female social hyperthermia paradigm, mice were allowed to freely interact during the 45-min assay. For the female-male paradigm, mice were allowed to freely interact during the 10-min assay; a shorter duration was chosen to prevent mating.

Confinement stress-induced hyperthermia

A small (12 cm x 8 cm) ventilated opaque plastic box was placed over each experimental mouse during the 60-min confinement assay. This permitted constant airflow and enough space for postural adjustments. A small weight was placed on top of the box to prevent mice from tilting it over and escaping. The confinement boxes were sanitized prior to and in between each test with Sani-Plex 128 and 70% ethanol. Confinement was chosen over restraint, the most

severe form of confinement stress, given previous work establishing confinement as a potent hyperthermic stressor in rodents (McGivern et al., 2009).

Metabolic phenotyping

Body composition was assessed via an EchoMRI^{TM}-100 analyzer (Houstin, TX, USA) that tracks fat and lean mass. Values here are presented as percentages of total body weight. Food intake was assessed by giving single-housed mice a pre-measured amount of food at approximately ZT 11.5. The remaining food was weighed at ZT 0.5 and ZT 11.5 every day for 5 consecutive days to assess day/night food intake variations, accounting for the presence of crumbs in the bedding. Values here are presented as daily averages across the 5-days.

Tissue collection and preparation

Mice were deeply anesthetized with IP injection of sodium pentobarbital (15 mg/mL) and confirmed unconscious before proceeding. Mice were transcardially perfused with ice-cold DEPC-treated 1x phosphate-buffered saline (PBS, pH=7.4) until the lungs and liver cleared, followed by ice-cold 4% paraformaldehyde (PFA) diluted from a 16% stock solution (Electron Microscopy Sciences, Catalog# 15700) in DEPC-treated PBS. Brains were harvested, post-fixed in 4% PFA overnight, and dehydrated in 30% sucrose for 24-48 hours, maintaining RNase-free conditions throughout. Brains were then embedded in optimal cutting temperature (OCT) compound (Fisher Scientific, Catalog# 23-730-571) and stored at –80 °C until cryosectioned. Coronal sections at a thickness of 20-30 μm were collected in 4-8 series using a cryostat (Leica CM1950) and either directly mounted on slides or collected free-floating in PBS and kept in Eppendorf tubes filled with cryoprotectant solution (30% sucrose, 30% ethylene glycol, 1% polyvinylpyrrolidone in 1x PBS) stored at –20 °C until further processing.

Histology

Fluorescent in situ hybridization

To detect the presence of mRNA transcripts in the brain, coronal sections (20 μm in thickness) were first mounted on Superfrost™ Plus slides (Fisher Scientific, Catalog# 12-550-15) using RNase-free technique. Slides were allowed to dry and single molecule *in situ* hybridization was performed using the RNAscope® Multiplex Fluorescent Detection Kit version 2 (Advanced Cell Diagnostics, Newark, CA, USA) following manufacturer instructions. In brief, slides were fixed in prechilled 10% neutral buffered formalin for 20 min at 4 °C. Slides were then pre-treated with serial ethanol dehydration, hydrogen peroxide incubation, target retrieval using a food-grade steamer (Hamilton Beach Brands Inc, Glen Allen, VA, USA) heated to 99 °C, and protease III incubation (Park et al., 2026). Following pre-treatment steps, slides were incubated with a commercially available probe targeting *Rprm* (Bio-Techne, Catalog# 466071) at 40 °C for 2 hours. Signal amplification and fluorescent labeling were carried out using the provided solutions along with fluorophores such as Opal 570 (1:500, Akoya Biosciences, Catalog# NEL744001KT) and Opal 690 (1:500, Akoya Biosciences, Catalog# NEL745001KT). Slides were then counterstained with DAPI, coverslipped using Prolong™ Gold Antifade Mountant (Thermo Fisher Scientific, Catalog# P36930), cured overnight at room temperature, and stored at 4 °C until imaged and analyzed as described below.

QUANTIFICATION AND STATISTICAL ANALYSIS

Image Analysis and Quantification

Brain sections were imaged at 10x magnification using a Nikon Eclipse Ti2 inverted microscope, with images imported into ImageJ (Fiji version 2.1.0/1.53c, NIH). Prior to quantification, sections from comparable bregma distances were selected to ensure a similar rostro-caudal level was analyzed for all mice in each experiment, ranging from bregma -1.455 to -1.755 mm, which we considered the central to caudal VMHvl. Regions of interest (ROIs) and anatomical notations were defined and outlined by referencing the Allen Brain Mouse (v2, 2011)

and Paxinos and Franklin (v3, 2008) atlases. Cells were identified based on co-localization of the fluorescent signal with DAPI. Once images were selected, quantifications were performed manually by a blinded investigator as follows.

Fluorescent in situ hybridization

A cell was considered positive for a gene of interest following *in situ* hybridization if it contained 7 or more transcripts within a DAPI-positive cell (Park et al., 2026), using the cell counter plug-in in ImageJ to track positive cells. When needed, brightness/contrast was adjusted uniformly across images. For the validation of *Rprm*$^{Vglut2\text{-}FlpO}$ knockout mice, quantification was performed on one brain hemisphere per mouse. For the validation of *Rprm*$^{AAV\text{-}FlpO}$ knockout mice, both hemispheres were quantified and reported separately since stereotaxis can introduce variability in the degree of bilateral AAV delivery. Only mice that were confirmed to have successful bilateral targeting were included in the analysis.

Statistical Analysis

Statistical analyses and plots were generated in GraphPad Prism (version 11.0.2). Information on statistical tests used, sample sizes, and significance levels are reported in the figure legends. Comparisons between two groups were tested using unpaired *t*-tests. Comparisons involving multiple factors were conducted via 2-way analyses of variance (ANOVA), or in the case data was missing, a mixed effects model, with either repeated measures (RM) or independent factors. Pairwise comparisons were performed following a significant interaction using Šídák's multiple comparison test. Simple linear regression analyses were used to calculate rate of change for activity levels. All statistical analyses were two-tailed. Data were considered statistically significant when p is less than 0.05.

REFERENCES

Abbott, S.B.G., Saper, C.B., 2017. Median preoptic glutamatergic neurons promote thermoregulatory heat loss and water consumption in mice. The Journal of Physiology 595, 6569–6583. https://doi.org/10.1113/JP274667

Adriaan Bouwknecht, J., Olivier, B., Paylor, R.E., 2007. The stress-induced hyperthermia paradigm as a physiological animal model for anxiety: A review of pharmacological and genetic studies in the mouse. Neuroscience & Biobehavioral Reviews, Neurogentics and Behavior 31, 41–59. https://doi.org/10.1016/j.neubiorev.2006.02.002

Amigo, J.D., Opazo, J.C., Jorquera, R., Wichmann, I.A., Garcia-Bloj, B.A., Alarcon, M.A., Owen, G.I., Corvalán, A.H., 2018. The Reprimo Gene Family: A Novel Gene Lineage in Gastric Cancer with Tumor Suppressive Properties. Int J Mol Sci 19, 1862. https://doi.org/10.3390/ijms19071862

Archer, J., 1975. Rodent sex differences in emotional and related behavior. Behavioral Biology 14, 451–479. https://doi.org/10.1016/S0091-6773(75)90636-7

Archer, T., Ogren, S.-O., Ross, S.B., 1981. N-2-chloroethyl-N-ethyl-2-bromobenzylamine hydrochloride (DSP4), a new selective noradrenaline neurotoxin, and taste neophobia in the rat. Psychobiology 9, 197–202. https://doi.org/10.3758/BF03332923

Armbruster, B.N., Li, X., Pausch, M.H., Herlitze, S., Roth, B.L., 2007. Evolving the lock to fit the key to create a family of G protein-coupled receptors potently activated by an inert ligand. Proc Natl Acad Sci U S A 104, 5163–5168. https://doi.org/10.1073/pnas.0700293104

Aukema, R.J., Petrie, G.N., Lau, B.K., Seabrook, L.T., Baglot, S.L., Christianson, J.P., Bains, J.S., Morena, M., Borgland, S.L., Hill, M.N., 2025. A network of basolateral amygdala

projection neurons contributes to stress-induced activation of the hypothalamic-pituitary-adrenal axis. Science Advances 11, eadv3737. https://doi.org/10.1126/sciadv.adv3737

Belin, D., Berson, N., Balado, E., Piazza, P.V., Deroche-Gamonet, V., 2011. High-novelty-preference rats are predisposed to compulsive cocaine self-administration. Neuropsychopharmacology 36, 569–579. https://doi.org/10.1038/npp.2010.188

Buchegger, K., Riquelme, I., Viscarra, T., Ili, C., Brebi, P., Huang, T.H.-M., Roa, J.C., 2017. Reprimo, a Potential p53-Dependent Tumor Suppressor Gene, Is Frequently Hypermethylated in Estrogen Receptor α-Positive Breast Cancer. International Journal of Molecular Sciences 18, 1525. https://doi.org/10.3390/ijms18081525

Byers, S.L., Wiles, M.V., Dunn, S.L., Taft, R.A., 2012. Mouse Estrous Cycle Identification Tool and Images. PLOS ONE 7, e35538. https://doi.org/10.1371/journal.pone.0035538

Cabrera-Zapata, L.E., Venkataraman, A., Harrington, A.M., Hu, J., Castro-Navarro, F., Galatsis, K., Duan, X., Brierley, S.M., Stietz, K.K., Ingraham, H.A., 2026. A Neuroendocrine Circuit That Suppresses Excretion and Pelvic Pain During Activity. https://doi.org/10.64898/2026.07.23.736864

Cain, M.E., Saucier, D.A., Bardo, M.T., 2005. Novelty seeking and drug use: contribution of an animal model. Exp Clin Psychopharmacol 13, 367–375. https://doi.org/10.1037/1064-1297.13.4.367

Calvo, N., Cecchi, M., Kabbaj, M., Watson, S.J., Akil, H., 2011. Differential effects of social defeat in rats with high and low locomotor response to novelty. Neuroscience 183, 81–89. https://doi.org/10.1016/j.neuroscience.2011.03.046

Cannon, B., Nedergaard, J., 2011. Nonshivering thermogenesis and its adequate measurement in metabolic studies. J Exp Biol 214, 242–253. https://doi.org/10.1242/jeb.050989

Catalano, P.N., Bonaventura, M.M., Silveyra, P., Bettler, B., Libertun, C., Lux-Lantos, V.A., 2005. GABA(B1) knockout mice reveal alterations in prolactin levels, gonadotropic axis, and reproductive function. Neuroendocrinology 82, 294–305. https://doi.org/10.1159/000093128

Catalano, P.N., Di Giorgio, N., Bonaventura, M.M., Bettler, B., Libertun, C., Lux-Lantos, V.A., 2010. Lack of functional GABA(B) receptors alters GnRH physiology and sexual dimorphic expression of GnRH and GAD-67 in the brain. Am J Physiol Endocrinol Metab 298, E683-696. https://doi.org/10.1152/ajpendo.00532.2009

Cheung, C.C., Krause, W.C., Edwards, R.H., Yang, C.F., Shah, N.M., Hnasko, T.S., Ingraham, H.A., 2015. Sex-dependent changes in metabolism and behavior, as well as reduced anxiety after eliminating ventromedial hypothalamus excitatory output. Molecular Metabolism 4, 857–866. https://doi.org/10.1016/j.molmet.2015.09.001

Chowen, J.A., Argente, J., Vician, L., Clifton, D.K., Steiner, R.A., 1990. Pro-opiomelanocortin messenger RNA in hypothalamic neurons is increased by testosterone through aromatization to estradiol. Neuroendocrinology 52, 581–588. https://doi.org/10.1159/000125647

Correa, S.M., Newstrom, D.W., Warne, J.P., Flandin, P., Cheung, C.C., Lin-Moore, A.T., Pierce, A.A., Xu, A.W., Rubenstein, J.L., Ingraham, H.A., 2015. An Estrogen-Responsive Module in the Ventromedial Hypothalamus Selectively Drives Sex-Specific Activity in Females. Cell Reports 10, 62–74. https://doi.org/10.1016/j.celrep.2014.12.011

Dalooei, J.R., Sahraei, H., Meftahi, G.H., Khosravi, M., Bahari, Z., Hatef, B., Mohammadi, A., Nicaeili, F., Eftekhari, F., Ghamari, F., Hadipour, M., Kaka, G., 2016. Temporary amygdala inhibition reduces stress effects in female mice. J Adv Res 7, 643–649. https://doi.org/10.1016/j.jare.2016.06.008

Davis, B.A., Clinton, S.M., Akil, H., Becker, J.B., 2008. The effects of novelty-seeking phenotypes and sex differences on acquisition of cocaine self-administration in selectively bred High-Responder and Low-Responder rats. Pharmacol Biochem Behav 90, 331–338. https://doi.org/10.1016/j.pbb.2008.03.008

Deem, J.D., Faber, C.L., Pedersen, C., Phan, B.A., Larsen, S.A., Ogimoto, K., Nelson, J.T., Damian, V., Tran, M.A., Palmiter, R.D., Kaiyala, K.J., Scarlett, J.M., Bruchas, M.R., Schwartz, M.W., Morton, G.J., 2020. Cold-induced hyperphagia requires AgRP neuron activation in mice. eLife 9, e58764. https://doi.org/10.7554/eLife.58764

Delini-Stula, A., Mogilnicka, E., Hunn, C., Dooley, D.J., 1984. Novelty-oriented behavior in the rat after selective damage of locus coeruleus projections by DSP-4, a new noradrenergic neurotoxin. Pharmacol Biochem Behav 20, 613–618. https://doi.org/10.1016/0091-3057(84)90312-5

Dellu, F., Piazza, P.V., Mayo, W., Le Moal, M., Simon, H., 1996. Novelty-seeking in rats--biobehavioral characteristics and possible relationship with the sensation-seeking trait in man. Neuropsychobiology 34, 136–145. https://doi.org/10.1159/000119305

Devidze, N., Lee, A.W., Zhou, J., Pfaff, D.W., 2006. CNS arousal mechanisms bearing on sex and other biologically regulated behaviors. Physiology & Behavior, Proceedings from the 2005 Meeting of the Society for the Study of Ingestive Behavior 88, 283–293. https://doi.org/10.1016/j.physbeh.2006.05.030

Faber, C.L., Matsen, M.E., Velasco, K.R., Damian, V., Phan, B.A., Adam, D., Therattil, A., Schwartz, M.W., Morton, G.J., 2018. Distinct Neuronal Projections From the Hypothalamic Ventromedial Nucleus Mediate Glycemic and Behavioral Effects. Diabetes 67, 2518–2529. https://doi.org/10.2337/db18-0380

Feng, C., Wang, Y., Zha, X., Cao, H., Huang, S., Cao, D., Zhang, K., Xie, T., Xu, X., Liang, Z., Zhang, Z., 2022. Cold-sensitive ventromedial hypothalamic neurons control homeostatic thermogenesis and social interaction-associated hyperthermia. Cell Metabolism 34, 888-901.e5. https://doi.org/10.1016/j.cmet.2022.05.002

Fenno, L.E., Ramakrishnan, C., Kim, Y.S., Evans, K.E., Lo, M., Vesuna, S., Inoue, M., Cheung, K.Y.M., Yuen, E., Pichamoorthy, N., Hong, A.S.O., Deisseroth, K., 2020. Comprehensive Dual- and Triple-Feature Intersectional Single-Vector Delivery of Diverse Functional Payloads to Cells of Behaving Mammals. Neuron 107, 836-853.e11. https://doi.org/10.1016/j.neuron.2020.06.003

Fermani, F., Chang, S., Mastrodicasa, Y., Peters, C., Gaitanos, L., Alcala Morales, P.L., Ramakrishnan, C., Deisseroth, K., Klein, R., 2025. Food and water intake are regulated by distinct central amygdala circuits revealed using intersectional genetics. Nat Commun 16, 3072. https://doi.org/10.1038/s41467-025-58144-3

Flagel, S.B., Waselus, M., Clinton, S.M., Watson, S.J., Akil, H., 2014. Antecedents and consequences of drug abuse in rats selectively bred for high and low response to novelty. Neuropharmacology 76 Pt B, 425–436. https://doi.org/10.1016/j.neuropharm.2013.04.033

Gancarz, A.M., Robble, M.A., Kausch, M.A., Lloyd, D.R., Richards, J.B., 2012. Association between locomotor response to novelty and light reinforcement: sensory reinforcement as a rodent model of sensation seeking. Behav Brain Res 230, 380–388. https://doi.org/10.1016/j.bbr.2012.02.028

Gene Detail :: Allen Brain Atlas: Developing Mouse Brain [WWW Document], n.d. URL https://developingmouse.brain-map.org/gene/show/43717 (accessed 11.25.25a).

Gene Detail :: Allen Brain Atlas: Developing Mouse Brain [WWW Document], n.d. URL https://developingmouse.brain-map.org/gene/show/80230 (accessed 5.5.26b).

Harro, J., Oreland, L., Vasar, E., Bradwejn, J., 1995. Impaired exploratory behaviour after DSP-4 treatment in rats: implications for the increased anxiety after noradrenergic denervation. Eur Neuropsychopharmacol 5, 447–455. https://doi.org/10.1016/0924-977x(95)00015-h

Harshaw, C., Lanzkowsky, J., Tran, A.-Q.D., Bradley, A.R., Jaime, M., 2021. Oxytocin and 'social hyperthermia': Interaction with β3-adrenergic receptor-mediated thermogenesis and significance for the expression of social behavior in male and female mice. Hormones and Behavior 131, 104981. https://doi.org/10.1016/j.yhbeh.2021.104981

Hashikawa, K., Hashikawa, Y., Tremblay, R., Zhang, J., Feng, J.E., Sabol, A., Piper, W.T., Lee, H., Rudy, B., Lin, D., 2017. Esr1 + cells in the ventromedial hypothalamus control female aggression. Nature Neuroscience 20, 1580–1590. https://doi.org/10.1038/nn.4644

He, Y., Xu, P., Wang, C., Xia, Y., Yu, M., Yang, Y., Yu, K., Cai, X., Qu, N., Saito, K., Wang, J., Hyseni, I., Robertson, M., Piyarathna, B., Gao, M., Khan, S.A., Liu, F., Chen, R., Coarfa, C., Zhao, Z., Tong, Q., Sun, Z., Xu, Y., 2020. Estrogen receptor-α expressing neurons in the ventrolateral VMH regulate glucose balance. Nature Communications 11, 2165. https://doi.org/10.1038/s41467-020-15982-7

Hirschberg, P.R., Sarkar, P., Teegala, S.B., Routh, V.H., 2020. Ventromedial hypothalamus glucose-inhibited neurones: A role in glucose and energy homeostasis? J Neuroendocrinol 32, e12773. https://doi.org/10.1111/jne.12773

Hooks, M.S., Juncos, J.L., Justice, J.B., Meiergerd, S.M., Povlock, S.L., Schenk, J.O., Kalivas, P.W., 1994. Individual locomotor response to novelty predicts selective alterations in D1

and D2 receptors and mRNAs. J Neurosci 14, 6144–6152. https://doi.org/10.1523/JNEUROSCI.14-10-06144.1994

Hulsen, T., de Vlieg, J., Alkema, W., 2008. BioVenn – a web application for the comparison and visualization of biological lists using area-proportional Venn diagrams. BMC Genomics 9, 488. https://doi.org/10.1186/1471-2164-9-488

Hussein, M.N., Alotaibi, K.S., Althobaiti, S.A., Albattal, S.B., Ke, X., Dai, J., Cao, G., Soliman, M.M., 2025. LPS mediated neuronal c-Fos activation: whole-brain mapping, site and time effect in intoxicated mice. Toxicol Res 14, tfaf131. https://doi.org/10.1093/toxres/tfaf131

Hylander, B.L., Qiao, G., Gomez, E.C., Singh, P., Repasky, E.A., 2023. Housing temperature plays a critical role in determining gut microbiome composition in research mice: Implications for experimental reproducibility. Biochimie 210, 71–81. https://doi.org/10.1016/j.biochi.2023.01.016

Inayat, M., Cruz-Sanchez, A., Thorpe, H.H.A., Frie, J.A., Richards, B.A., Khokhar, J.Y., Arruda-Carvalho, M., 2021. Promoting and Optimizing the Use of 3D-Printed Objects in Spontaneous Recognition Memory Tasks in Rodents: A Method for Improving Rigor and Reproducibility. eNeuro 8. https://doi.org/10.1523/ENEURO.0319-21.2021

Jovanovic, P., Pool, A.-H., Morones, N., Wang, Y., Novinbakht, E., Keshishian, N., Jang, K., Oka, Y., Riera, C.E., 2023. A sex-specific thermogenic neurocircuit induced by predator smell recruiting cholecystokinin neurons in the dorsomedial hypothalamus. Nat Commun 14, 4937. https://doi.org/10.1038/s41467-023-40484-7

Kammel, L., 2019. Sexually Differentiated Neuron Populations in the Ventromedial Hypothalamus Contribute to Sex-Specific Regulation of Energy Balance. UCLA.

Kammel, L.G., Correa, S.M., 2020. Selective sexual differentiation of neurone populations may contribute to sex-specific outputs of the ventromedial nucleus of the hypothalamus. J Neuroendocrinol 32. https://doi.org/10.1111/jne.12801

Khodai, T., Luckman, S.M., 2021. Ventromedial Nucleus of the Hypothalamus Neurons Under the Magnifying Glass. Endocrinology 162, bqab141. https://doi.org/10.1210/endocr/bqab141

Kim, D.-W., Yao, Z., Graybuck, L.T., Kim, T.K., Nguyen, T.N., Smith, K.A., Fong, O., Yi, L., Koulena, N., Pierson, N., Shah, S., Lo, L., Pool, A.-H., Oka, Y., Pachter, L., Cai, L., Tasic, B., Zeng, H., Anderson, D.J., 2019. Multimodal Analysis of Cell Types in a Hypothalamic Node Controlling Social Behavior. Cell 179, 713-728.e17. https://doi.org/10.1016/j.cell.2019.09.020

Kim, J.H., Lee, S.-R., Li, L.-H., Park, H.-J., Park, J.-H., Lee, K.Y., Kim, M.-K., Shin, B.A., Choi, S.-Y., 2011. High Cleavage Efficiency of a 2A Peptide Derived from Porcine Teschovirus-1 in Human Cell Lines, Zebrafish and Mice. PLOS ONE 6, e18556. https://doi.org/10.1371/journal.pone.0018556

Kirschmann, E.K., Smith, T.T., Shold, J.N., Donny, E.C., Sved, A.F., Thiels, E., 2025. Locomotor Response to Novelty: What Does It Tell Us? Dev Psychobiol 67, e70024. https://doi.org/10.1002/dev.70024

Krause, W.C., Ingraham, H.A., 2017. Origins and Functions of the Ventrolateral VMH: A Complex Neuronal Cluster Orchestrating Sex Differences in Metabolism and Behavior, in: Mauvais-Jarvis, F. (Ed.), Sex and Gender Factors Affecting Metabolic Homeostasis, Diabetes and Obesity, Advances in Experimental Medicine and Biology. Springer International Publishing, Cham, pp. 199–213. https://doi.org/10.1007/978-3-319-70178-3_10

Krause, W.C., Rodriguez, R., Gegenhuber, B., Matharu, N., Rodriguez, A.N., Padilla-Roger, A.M., Toma, K., Herber, C.B., Correa, S.M., Duan, X., Ahituv, N., Tollkuhn, J., Ingraham, H.A., 2021. Oestrogen engages brain MC4R signalling to drive physical activity in female mice. Nature 599, 131–135. https://doi.org/10.1038/s41586-021-04010-3

Kunwar, P.S., Zelikowsky, M., Remedios, R., Cai, H., Yilmaz, M., Meister, M., Anderson, D.J., 2015. Ventromedial hypothalamic neurons control a defensive emotion state. eLife 4, e06633. https://doi.org/10.7554/eLife.06633

Lazarus, M., Yoshida, K., Coppari, R., Bass, C.E., Mochizuki, T., Lowell, B.B., Saper, C.B., 2007. EP3 prostaglandin receptors in the median preoptic nucleus are critical for fever responses. Nat Neurosci 10, 1131–1133. https://doi.org/10.1038/nn1949

Lee, H., Kim, D.-W., Remedios, R., Anthony, T.E., Chang, A., Madisen, L., Zeng, H., Anderson, D.J., 2014. Scalable control of mounting and attack by Esr1 + neurons in the ventromedial hypothalamus. Nature 509, 627–632. https://doi.org/10.1038/nature13169

Lee, S.-H., Meilandt, W.J., Xie, L., Gandham, V.D., Ngu, H., Barck, K.H., Rezzonico, M.G., Imperio, J., Lalehzadeh, G., Huntley, M.A., Stark, K.L., Foreman, O., Carano, R.A.D., Friedman, B.A., Sheng, M., Easton, A., Bohlen, C.J., Hansen, D.V., 2021. Trem2 restrains the enhancement of tau accumulation and neurodegeneration by β-amyloid pathology. Neuron 109, 1283-1301.e6. https://doi.org/10.1016/j.neuron.2021.02.010

Li, Yidan, Li, Yue, Zhang, X., Li, Ying, Liu, Y., Xu, H., 2023. CaMKIIa Neurons of the Ventromedial Hypothalamus Mediate Wakefulness and Anxiety-like Behavior. Neurochem Res 48, 2463–2475. https://doi.org/10.1007/s11064-023-03925-9

Li, Z., Zhou, Z., Tian, S., Zhang, K., An, G., Zhang, Y., Ma, R., Sheng, B., Wang, T., Yang, H., Yang, L., 2022. RPRM deletion preserves hematopoietic regeneration by promoting

EGFR-dependent DNA repair and hematopoietic stem cell proliferation post ionizing radiation. Cell Biol Int 46, 2158–2172. https://doi.org/10.1002/cbin.11900

Lo, L., Yao, S., Kim, D.-W., Cetin, A., Harris, J., Zeng, H., Anderson, D.J., Weissbourd, B., 2019. Connectional architecture of a mouse hypothalamic circuit node controlling social behavior. Proc. Natl. Acad. Sci. U.S.A. 116, 7503–7512. https://doi.org/10.1073/pnas.1817503116

Lustberg, D., Tillage, R.P., Bai, Y., Pruitt, M., Liles, L.C., Weinshenker, D., 2020. Noradrenergic circuits in the forebrain control affective responses to novelty. Psychopharmacology 237, 3337–3355. https://doi.org/10.1007/s00213-020-05615-8

Mabrouk, O.S., Han, J.L., Wong, J.-M.T., Akil, H., Kennedy, R.T., Flagel, S.B., 2018. The in Vivo Neurochemical Profile of Selectively Bred High-Responder and Low-Responder Rats Reveals Baseline, Cocaine-Evoked, and Novelty-Evoked Differences in Monoaminergic Systems. ACS Chem Neurosci 9, 715–724. https://doi.org/10.1021/acschemneuro.7b00294

Machado, N.L.S., Abbott, S.B.G., Resch, J.M., Zhu, L., Arrigoni, E., Lowell, B.B., Fuller, P.M., Fontes, M.A.P., Saper, C.B., 2018. A Glutamatergic Hypothalamomedullary Circuit Mediates Thermogenesis, but Not Heat Conservation, during Stress-Induced Hyperthermia. Current Biology 28, 2291-2301.e5. https://doi.org/10.1016/j.cub.2018.05.064

Machado, N.L.S., Bandaru, S.S., Abbott, S.B.G., Saper, C.B., 2020. EP3R-Expressing Glutamatergic Preoptic Neurons Mediate Inflammatory Fever. J Neurosci 40, 2573–2588. https://doi.org/10.1523/JNEUROSCI.2887-19.2020

Machado, N.L.S., Lynch, N., Costa, L.H.A., Melville, D., Kucukdereli, H., Kaur, S., Banks, A.S., Raffin, F., Ramirez-Plascencia, O.D., Aten, S., Lima, J.D., Bandaru, S.S., Palmiter, R.D.,

Saper, C.B., 2025. Preoptic EP3R neurons constitute a two-way switch for fever and torpor. Nature. https://doi.org/10.1038/s41586-025-09056-1

Madisen, L., Zwingman, T.A., Sunkin, S.M., Oh, S.W., Zariwala, H.A., Gu, H., Ng, L.L., Palmiter, R.D., Hawrylycz, M.J., Jones, A.R., Lein, E.S., Zeng, H., 2010. A robust and high-throughput Cre reporting and characterization system for the whole mouse brain. Nat Neurosci 13, 133–140. https://doi.org/10.1038/nn.2467

Malik, S., Jiang, S., Garee, J.P., Verdin, E., Lee, A.V., O'Malley, B.W., Zhang, M., Belaguli, N.S., Oesterreich, S., 2010. Histone Deacetylase 7 and FoxA1 in Estrogen-Mediated Repression of RPRM. Molecular and Cellular Biology 30, 399–412. https://doi.org/10.1128/MCB.00907-09

Marinelli, M., White, F.J., 2000. Enhanced vulnerability to cocaine self-administration is associated with elevated impulse activity of midbrain dopamine neurons. J Neurosci 20, 8876–8885. https://doi.org/10.1523/JNEUROSCI.20-23-08876.2000

Martínez de Morentin, P.B., González-García, I., Martins, L., Lage, R., Fernández-Mallo, D., Martínez-Sánchez, N., Ruíz-Pino, F., Liu, J., Morgan, D.A., Pinilla, L., Gallego, R., Saha, A.K., Kalsbeek, A., Fliers, E., Bisschop, P.H., Diéguez, C., Nogueiras, R., Rahmouni, K., Tena-Sempere, M., López, M., 2014. Estradiol Regulates Brown Adipose Tissue Thermogenesis via Hypothalamic AMPK. Cell Metab 20, 41–53. https://doi.org/10.1016/j.cmet.2014.03.031

Massa, M.G., Scott, R.L., Cara, A.L., Cortes, L.R., Vander, P.B., Sandoval, N.P., Park, J.W., Ali, S.L., Velez, L.M., Wang, H.-B., Ati, S.S., Tesfaye, B., Reue, K., van Veen, J.E., Seldin, M.M., Correa, S.M., 2023. Feeding neurons integrate metabolic and reproductive states in mice. iScience 26, 107918. https://doi.org/10.1016/j.isci.2023.107918

Mccarthy, M.M., Mcdonald, C.H., Brooks, P.J., Goldman, D., 1996. An Anxiolytic Action of Oxytocin is Enhanced by Estrogen in the Mouse. Physiology & Behavior 60, 1209–1215. https://doi.org/10.1016/S0031-9384(96)00212-0

McGivern, R.F., Zuloaga, D.G., Handa, R.J., 2009. Sex differences in stress-induced hyperthermia in rats: Restraint versus confinement. Physiology & Behavior 98, 416–420. https://doi.org/10.1016/j.physbeh.2009.07.004

Morrison, S.F., Madden, C.J., Tupone, D., 2012. Central Control of Brown Adipose Tissue Thermogenesis. Front Endocrinol (Lausanne) 3, 5. https://doi.org/10.3389/fendo.2012.00005

Morrison, S.F., Nakamura, K., 2011. Central neural pathways for thermoregulation. Front Biosci 16, 74–104. https://doi.org/10.2741/3677

Muñoz Zamora, A., Douglas, A., Conway, P.B., Urrieta, E., Moniz, T., O'Leary, J.D., Marks, L., Denny, C.A., Ortega-de San Luis, C., Lynch, L., Ryan, T.J., 2025. Cold memories control whole-body thermoregulatory responses. Nature 641, 942–951. https://doi.org/10.1038/s41586-025-08902-6

Musatov, S., Chen, W., Pfaff, D.W., Mobbs, C.V., Yang, X.-J., Clegg, D.J., Kaplitt, M.G., Ogawa, S., 2007. Silencing of estrogen receptor α in the ventromedial nucleus of hypothalamus leads to metabolic syndrome. PNAS 104, 2501–2506. https://doi.org/10.1073/pnas.0610787104

Nakamura, K., 2015. Neural circuit for psychological stress-induced hyperthermia. Temperature (Austin) 2, 352–361. https://doi.org/10.1080/23328940.2015.1070944

Nakamura, K., Morrison, S.F., 2008. Preoptic mechanism for cold-defensive responses to skin cooling. J Physiol 586, 2611–2620. https://doi.org/10.1113/jphysiol.2008.152686

Neophytou, S.I., Aspley, S., Butler, S., Beckett, S., Marsden, C.A., 2001. Effects of lesioning noradrenergic neurones in the locus coeruleus on conditioned and unconditioned aversive behaviour in the rat. Prog Neuropsychopharmacol Biol Psychiatry 25, 1307–1321. https://doi.org/10.1016/s0278-5846(01)00181-6

Nyssen, L., Brabant, C., Didone, V., Quertemont, E., 2016. Response to novelty and cocaine stimulant effects: lack of stability across environments in female Swiss mice. Psychopharmacology (Berl) 233, 691–700. https://doi.org/10.1007/s00213-015-4146-0

Ohki, R., Nemoto, J., Murasawa, H., Oda, E., Inazawa, J., Tanaka, N., Taniguchi, T., 2000. Reprimo, a New Candidate Mediator of the p53-mediated Cell Cycle Arrest at the G2 Phase. J. Biol. Chem. 275, 22627–22630. https://doi.org/10.1074/jbc.C000235200

Oka, T., 2018. Chapter 35 - Stress-induced hyperthermia and hypothermia, in: Romanovsky, A.A. (Ed.), Handbook of Clinical Neurology, Thermoregulation: From Basic Neuroscience to Clinical Neurology, Part II. Elsevier, pp. 599–621. https://doi.org/10.1016/B978-0-444-64074-1.00035-5

Oka, T., 2015. Psychogenic fever: how psychological stress affects body temperature in the clinical population. Temperature 2, 368–378. https://doi.org/10.1080/23328940.2015.1056907

Oliveira, V.E. de M., Bodea, I., Bakker, J., 2025. Ventromedial hypothalamus (VMHvl) nNOS neurons regulate social behaviors in a sex-specific manner. Commun Biol 8, 1732. https://doi.org/10.1038/s42003-025-09279-y

Olivier, B., Zethof, T., Pattij, T., van Boogaert, M., van Oorschot, R., Leahy, C., Oosting, R., Bouwknecht, A., Veening, J., van der Gugten, J., Groenink, L., 2003. Stress-induced hyperthermia and anxiety: pharmacological validation. European Journal of

Pharmacology, Animal Models of Anxiety Disorders 463, 117–132. https://doi.org/10.1016/S0014-2999(03)01326-8

Ooki, A., Yamashita, K., Yamaguchi, K., Mondal, A., Nishimiya, H., Watanabe, M., 2013. DNA damage-inducible gene, reprimo functions as a tumor suppressor and is suppressed by promoter methylation in gastric cancer. Mol Cancer Res 11, 1362–1374. https://doi.org/10.1158/1541-7786.MCR-13-0091

Osterhout, J.A., Kapoor, V., Eichhorn, S.W., Vaughn, E., Moore, J.D., Liu, D., Lee, D., DeNardo, L.A., Luo, L., Zhuang, X., Dulac, C., 2022. A preoptic neuronal population controls fever and appetite during sickness. Nature 606, 937–944. https://doi.org/10.1038/s41586-022-04793-z

Park, J.W., Cortes, L.R., Sandoval, N.P., Vree, A.R., Baron, A.G., Vranich, K., Fideles, H.J., Martinez, R.M., Dilday, E.A., Hansen, M.R., Budek, W., Lopez, J.I., Kammel, L.G., van Veen, J.E., Correa, S.M., 2026. Sex-Specific Thermoregulatory Effects of Estrogen Signaling in Reprimo Lineage Cells. Endocrinology 167, bqaf177. https://doi.org/10.1210/endocr/bqaf177

Phelps, E.A., LeDoux, J.E., 2005. Contributions of the Amygdala to Emotion Processing: From Animal Models to Human Behavior. Neuron 48, 175–187. https://doi.org/10.1016/j.neuron.2005.09.025

Piazza, P.V., Deminière, J.M., Le Moal, M., Simon, H., 1989. Factors that predict individual vulnerability to amphetamine self-administration. Science 245, 1511–1513. https://doi.org/10.1126/science.2781295

Piazza, P.V., Maccari, S., Deminière, J.M., Le Moal, M., Mormède, P., Simon, H., 1991. Corticosterone levels determine individual vulnerability to amphetamine self-

administration. Proc Natl Acad Sci U S A 88, 2088–2092. https://doi.org/10.1073/pnas.88.6.2088

Piñol, R.A., Mogul, A.S., Hadley, C.K., Saha, A., Li, C., Škop, V., Province, H.S., Xiao, C., Gavrilova, O., Krashes, M.J., Reitman, M.L., 2021. Preoptic BRS3 neurons increase body temperature and heart rate via multiple pathways. Cell Metabolism 33, 1389-1403.e6. https://doi.org/10.1016/j.cmet.2021.05.001

Raam, T., Li, Q., Gu, L., Elagio, G.M., Lim, K.Y., Taimish, J.Y., Zhang, X., Sandoval, N.P., Correa, S.M., Hong, W., 2026. Cortical regulation of collective social dynamics during environmental challenge. Nat Neurosci 29, 901–914. https://doi.org/10.1038/s41593-026-02224-0

Redolat, R., Pérez-Martínez, A., Carrasco, M.C., Mesa, P., 2009. Individual differences in novelty-seeking and behavioral responses to nicotine: a review of animal studies. Curr Drug Abuse Rev 2, 230–242. https://doi.org/10.2174/1874473710902030230

Refinetti, R., 2020. Circadian rhythmicity of body temperature and metabolism. Temperature (Austin) 7, 321–362. https://doi.org/10.1080/23328940.2020.1743605

Reis, W.L., Yi, C.-X., Gao, Y., Tschöp, M.H., Stern, J.E., 2015. Brain Innate Immunity Regulates Hypothalamic Arcuate Neuronal Activity and Feeding Behavior. Endocrinology 156, 1303–1315. https://doi.org/10.1210/en.2014-1849

Robbins, A., Tom, C.A., Cosman, M.N., Moursi, C., Shipp, L., Spencer, T.M., Brash, T., Devlin, M.J., 2018. Low temperature decreases bone mass in mice: implications for humans. Am J Phys Anthropol 167, 557–568. https://doi.org/10.1002/ajpa.23684

Root, D.H., Barker, D.J., Estrin, D.J., Miranda-Barrientos, J.A., Liu, B., Zhang, S., Wang, H.-L., Vautier, F., Ramakrishnan, C., Kim, Y.S., Fenno, L., Deisseroth, K., Morales, M., 2020.

Distinct Signaling by Ventral Tegmental Area Glutamate, GABA, and Combinatorial Glutamate-GABA Neurons in Motivated Behavior. Cell Reports 32, 108094. https://doi.org/10.1016/j.celrep.2020.108094

Roozendaal, B., McEwen, B.S., Chattarji, S., 2009. Stress, memory and the amygdala. Nat Rev Neurosci 10, 423–433. https://doi.org/10.1038/nrn2651

Routh, V.H., 2010. Glucose Sensing Neurons in the Ventromedial Hypothalamus. Sensors (Basel) 10, 9002–9025. https://doi.org/10.3390/s101009002

Sajdyk, T.J., Johnson, P.L., Leitermann, R.J., Fitz, S.D., Dietrich, A., Morin, M., Gehlert, D.R., Urban, J.H., Shekhar, A., 2008. Neuropeptide Y in the Amygdala Induces Long-Term Resilience to Stress-Induced Reductions in Social Responses But Not Hypothalamic–Adrenal–Pituitary Axis Activity or Hyperthermia. J. Neurosci. 28, 893–903. https://doi.org/10.1523/JNEUROSCI.0659-07.2008

Sara, S.J., Dyon-Laurent, C., Hervé, A., 1995. Novelty seeking behavior in the rat is dependent upon the integrity of the noradrenergic system. Cognitive Brain Research 2, 181–187. https://doi.org/10.1016/0926-6410(95)90007-1

Sato, N., Fukushima, N., Hruban, R.H., Goggins, M., 2008. CpG island methylation profile of pancreatic intraepithelial neoplasia. Mod Pathol 21, 238–244. https://doi.org/10.1038/modpathol.3800991

Sato, N., Fukushima, N., Maitra, A., Matsubayashi, H., Yeo, C.J., Cameron, J.L., Hruban, R.H., Goggins, M., 2003. Discovery of Novel Targets for Aberrant Methylation in Pancreatic Carcinoma Using High-Throughput Microarrays1. Cancer Res 63, 3735–3742.

Schuler, V., Lüscher, C., Blanchet, C., Klix, N., Sansig, G., Klebs, K., Schmutz, M., Heid, J., Gentry, C., Urban, L., Fox, A., Spooren, W., Jaton, A.L., Vigouret, J., Pozza, M., Kelly,

P.H., Mosbacher, J., Froestl, W., Käslin, E., Korn, R., Bischoff, S., Kaupmann, K., van der Putten, H., Bettler, B., 2001. Epilepsy, hyperalgesia, impaired memory, and loss of pre- and postsynaptic GABA(B) responses in mice lacking GABA(B(1)). Neuron 31, 47–58. https://doi.org/10.1016/s0896-6273(01)00345-2

Seney, M.L., Walsh, C., Stolakis, R., Sibille, E., 2012. Neonatal testosterone partially organizes sex differences in stress-induced emotionality in mice. Neurobiol Dis 46, 486–496. https://doi.org/10.1016/j.nbd.2012.02.014

Shao, J., Chen, Y., Gao, D., Liu, Y., Hu, N., Yin, L., Zhang, X., Yang, F., 2023. Ventromedial hypothalamus relays chronic stress inputs and exerts bidirectional regulation on anxiety state and related sympathetic activity. Front Cell Neurosci 17, 1281919. https://doi.org/10.3389/fncel.2023.1281919

Shao, J., Gao, D.-S., Liu, Y.-H., Chen, S.-P., Liu, N., Zhang, L., Zhou, X.-Y., Xiao, Q., Wang, L.-P., Hu, H.-L., Yang, F., 2022. Cav3.1-driven bursting firing in ventromedial hypothalamic neurons exerts dual control of anxiety-like behavior and energy expenditure. Mol Psychiatry 27, 2901–2913. https://doi.org/10.1038/s41380-022-01513-x

Shimosato, K., Watanabe, S., 2003. Concurrent evaluation of locomotor response to novelty and propensity toward cocaine conditioned place preference in mice. Journal of Neuroscience Methods 128, 103–110. https://doi.org/10.1016/S0165-0270(03)00153-5

Silva, B.A., Mattucci, C., Krzywkowski, P., Murana, E., Illarionova, A., Grinevich, V., Canteras, N.S., Ragozzino, D., Gross, C.T., 2013. Independent hypothalamic circuits for social and predator fear. Nat Neurosci 16, 1731–1733. https://doi.org/10.1038/nn.3573

Škop, V., Guo, J., Liu, N., Xiao, C., Hall, K.D., Gavrilova, O., Reitman, M.L., 2020. Mouse Thermoregulation: Introducing the Concept of the Thermoneutral Point. Cell Reports 31, 107501. https://doi.org/10.1016/j.celrep.2020.03.065

Steyn, F.J., Wan, Y., Clarkson, J., Veldhuis, J.D., Herbison, A.E., Chen, C., 2013. Development of a methodology for and assessment of pulsatile luteinizing hormone secretion in juvenile and adult male mice. Endocrinology 154, 4939–4945. https://doi.org/10.1210/en.2013-1502

Stone, E.A., Zhang, Y., Rosengarten, H., Yeretsian, J., Quartermain, D., 1999. Brain alpha 1-adrenergic neurotransmission is necessary for behavioral activation to environmental change in mice. Neuroscience 94, 1245–1252. https://doi.org/10.1016/s0306-4522(99)00394-2

Su, J., Hashsham, A., Kodur, N., Burton, C., Mancuso, A., Singer, A., Wloszek, J., Tomlinson, A.J., Yacawych, W.T., Flak, J.N., Lewis, K.T., Oles, L.R., Mori, H., Bozadjieva-Kramer, N., Turcu, A.F., MacDougald, O.A., Myers, M.G., Affinati, A.H., 2025. Control of physiologic glucose homeostasis via hypothalamic modulation of gluconeogenic substrate availability. Molecular Metabolism 99, 102216. https://doi.org/10.1016/j.molmet.2025.102216

Suto, N., Austin, J.D., Vezina, P., 2001. Locomotor response to novelty predicts a rat's propensity to self-administer nicotine. Psychopharmacology (Berl) 158, 175–180. https://doi.org/10.1007/s002130100867

Takikawa, M., Nakano, A., Krishnaraj, J., Tabata, Y., Watanabe, Y., Okabe, A., Sakaguchi, Y., Fujiki, R., Mochizuki, A., Tajima, T., Sada, A., Matsushita, S., Wakabayashi, Y., Araki, K., Kaneda, A., Ishikawa, F., Sadaie, M., Ohki, R., 2025. Extrinsic induction of apoptosis and tumor suppression via the p53-Reprimo-Hippo-YAP/TAZ-p73 pathway. Proc Natl Acad Sci U S A 122, e2413126122. https://doi.org/10.1073/pnas.2413126122

Takikawa, M., Ohki, R., 2025. Reprimo (RPRM): A Tumor Suppressor That Induces Extrinsic Apoptosis via YAP Signaling. Cancer Science 116, 3266–3273. https://doi.org/10.1111/cas.70215

Tan, C.L., Knight, Z.A., 2018. Regulation of Body Temperature by the Nervous System. Neuron 98, 31–48. https://doi.org/10.1016/j.neuron.2018.02.022

The UniProt Consortium, Bateman, A., Martin, M.-J., Orchard, S., Magrane, M., Adesina, A., Ahmad, S., Bowler-Barnett, E.H., Bye-A-Jee, H., Carpentier, D., Denny, P., Fan, J., Garmiri, P., Gonzales, L.J.D.C., Hussein, A., Ignatchenko, A., Insana, G., Ishtiaq, R., Joshi, V., Jyothi, D., Kandasaamy, S., Lock, A., Luciani, A., Luo, J., Lussi, Y., Marin, J.S.M., Raposo, P., Rice, D.L., Santos, R., Speretta, E., Stephenson, J., Totoo, P., Tyagi, N., Urakova, N., Vasudev, P., Warner, K., Wijerathne, S., Yu, C.W.-H., Zaru, R., Bridge, A.J., Aimo, L., Argoud-Puy, G., Auchincloss, A.H., Axelsen, K.B., Bansal, P., Baratin, D., Batista Neto, T.M., Blatter, M.-C., Bolleman, J.T., Boutet, E., Breuza, L., Gil, B.C., Casals-Casas, C., Echioukh, K.C., Coudert, E., Cuche, B., De Castro, E., Estreicher, A., Famiglietti, M.L., Feuermann, M., Gasteiger, E., Gaudet, P., Gehant, S., Gerritsen, V., Gos, A., Gruaz, N., Hulo, C., Hyka-Nouspikel, N., Jungo, F., Kerhornou, A., Mercier, P.L., Lieberherr, D., Masson, P., Morgat, A., Paesano, S., Pedruzzi, I., Pilbout, S., Pourcel, L., Poux, S., Pozzato, M., Pruess, M., Redaschi, N., Rivoire, C., Sigrist, C.J.A., Sonesson, K., Sundaram, S., Sveshnikova, A., Wu, C.H., Arighi, C.N., Chen, C., Chen, Y., Huang, H., Laiho, K., Lehvaslaiho, M., McGarvey, P., Natale, D.A., Ross, K., Vinayaka, C.R., Wang, Y., Zhang, J., 2025. UniProt: the Universal Protein Knowledgebase in 2025. Nucleic Acids Research 53, D609–D617. https://doi.org/10.1093/nar/gkae1010

Thompson, C.L., Ng, L., Menon, V., Martinez, S., Lee, C.-K., Glattfelder, K., Sunkin, S.M., Henry, A., Lau, C., Dang, C., Garcia-Lopez, R., Martinez-Ferre, A., Pombero, A.,

Rubenstein, J.L.R., Wakeman, W.B., Hohmann, J., Dee, N., Sodt, A.J., Young, R., Smith, K., Nguyen, T.-N., Kidney, J., Kuan, L., Jeromin, A., Kaykas, A., Miller, J., Page, D., Orta, G., Bernard, A., Riley, Z., Smith, S., Wohnoutka, P., Hawrylycz, M.J., Puelles, L., Jones, A.R., 2014a. A High-Resolution Spatiotemporal Atlas of Gene Expression of the Developing Mouse Brain. Neuron 83, 309–323. https://doi.org/10.1016/j.neuron.2014.05.033

Thompson, C.L., Ng, L., Menon, V., Martinez, S., Lee, C.-K., Glattfelder, K., Sunkin, S.M., Henry, A., Lau, C., Dang, C., Garcia-Lopez, R., Martinez-Ferre, A., Pombero, A., Rubenstein, J.L.R., Wakeman, W.B., Hohmann, J., Dee, N., Sodt, A.J., Young, R., Smith, K., Nguyen, T.-N., Kidney, J., Kuan, L., Jeromin, A., Kaykas, A., Miller, J., Page, D., Orta, G., Bernard, A., Riley, Z., Smith, S., Wohnoutka, P., Hawrylycz, M.J., Puelles, L., Jones, A.R., 2014b. A High-Resolution Spatiotemporal Atlas of Gene Expression of the Developing Mouse Brain. Neuron 83, 309–323. https://doi.org/10.1016/j.neuron.2014.05.033

Tong, Q., Ye, C., McCrimmon, R.J., Dhillon, H., Choi, B., Kramer, M.D., Yu, J., Yang, Z., Christiansen, L.M., Lee, C.E., Choi, C.S., Zigman, J.M., Shulman, G.I., Sherwin, R.S., Elmquist, J.K., Lowell, B.B., 2007. Synaptic Glutamate Release by Ventromedial Hypothalamic (VMH) Neurons Is Part of the Neurocircuitry that Prevents Hypoglycemia. Cell Metab 5, 383–393. https://doi.org/10.1016/j.cmet.2007.04.001

Truett, G.E., Heeger, P., Mynatt, R.L., Truett, A.A., Walker, J.A., Warman, M.L., 2000. Preparation of PCR-quality mouse genomic DNA with hot sodium hydroxide and tris (HotSHOT). Biotechniques 29, 52, 54. https://doi.org/10.2144/00291bm09

Tu, L., Fukuda, M., Tong, Q., Xu, Y., 2022. The ventromedial hypothalamic nucleus: watchdog of whole-body glucose homeostasis. Cell Biosci 12, 71. https://doi.org/10.1186/s13578-022-00799-2

Uhlén, M., Fagerberg, L., Hallström, B.M., Lindskog, C., Oksvold, P., Mardinoglu, A., Sivertsson, Å., Kampf, C., Sjöstedt, E., Asplund, A., Olsson, I., Edlund, K., Lundberg, E., Navani, S., Szigyarto, C.A.-K., Odeberg, J., Djureinovic, D., Takanen, J.O., Hober, S., Alm, T., Edqvist, P.-H., Berling, H., Tegel, H., Mulder, J., Rockberg, J., Nilsson, P., Schwenk, J.M., Hamsten, M., von Feilitzen, K., Forsberg, M., Persson, L., Johansson, F., Zwahlen, M., von Heijne, G., Nielsen, J., Pontén, F., 2015. Tissue-based map of the human proteome. Science 347, 1260419. https://doi.org/10.1126/science.1260419

Van Swearingen, A.E.D., Walker, Q.D., Kuhn, C.M., 2013. Sex differences in novelty- and psychostimulant-induced behaviors of C57BL/6 mice. Psychopharmacology (Berl) 225, 707–718. https://doi.org/10.1007/s00213-012-2860-4

van Veen, J.E., Kammel, L.G., Bunda, P.C., Shum, M., Reid, M.S., Massa, M.G., Arneson, D.V., Park, J.W., Zhang, Z., Joseph, A.M., Hrncir, H., Liesa, M., Arnold, A.P., Yang, X., Correa, S.M., 2020. Hypothalamic oestrogen receptor alpha establishes a sexually dimorphic regulatory node of energy expenditure. Nat Metab 2, 351–363. https://doi.org/10.1038/s42255-020-0189-6

Veening, J.G., Bouwknecht, J.A., Joosten, H.J.J., Dederen, P.J., Zethof, T.J.J., Groenink, L., van der Gugten, J., Olivier, B., 2004. Stress-induced hyperthermia in the mouse: c-*fos* expression, corticosterone and temperature changes. Progress in Neuro-Psychopharmacology and Biological Psychiatry 28, 699–707. https://doi.org/10.1016/j.pnpbp.2004.05.007

Vidal-Infer, A., Arenas, M.C., Daza-Losada, M., Aguilar, M.A., Miñarro, J., Rodríguez-Arias, M., 2012. High novelty-seeking predicts greater sensitivity to the conditioned rewarding effects of cocaine. Pharmacol Biochem Behav 102, 124–132. https://doi.org/10.1016/j.pbb.2012.03.031

Vinkers, C.H., Bijlsma, E.Y., Houtepen, L.C., Westphal, K.G.C., Veening, J.G., Groenink, L., Olivier, B., 2010. Medial amygdala lesions differentially influence stress responsivity and sensorimotor gating in rats. Physiology & Behavior 99, 395–401. https://doi.org/10.1016/j.physbeh.2009.12.006

Vinkers, C.H., Groenink, L., van Bogaert, M.J.V., Westphal, K.G.C., Kalkman, C.J., van Oorschot, R., Oosting, R.S., Olivier, B., Korte, S.M., 2009a. Stress-induced hyperthermia and infection-induced fever: Two of a kind? Physiology & Behavior 98, 37–43. https://doi.org/10.1016/j.physbeh.2009.04.004

Vinkers, C.H., van Oorschot, R., Olivier, B., Groenink, L., 2009b. Stress-Induced Hyperthermia in the Mouse, in: Gould, T.D. (Ed.), Mood and Anxiety Related Phenotypes in Mice: Characterization Using Behavioral Tests. Humana Press, Totowa, NJ, pp. 139–152. https://doi.org/10.1007/978-1-60761-303-9_8

Viskaitis, P., Irvine, E.E., Smith, M.A., Choudhury, A.I., Alvarez-Curto, E., Glegola, J.A., Hardy, D.G., Pedroni, S.M.A., Paiva Pessoa, M.R., Fernando, A.B.P., Katsouri, L., Sardini, A., Ungless, M.A., Milligan, G., Withers, D.J., 2017. Modulation of SF1 Neuron Activity Coordinately Regulates Both Feeding Behavior and Associated Emotional States. Cell Rep 21, 3559–3572. https://doi.org/10.1016/j.celrep.2017.11.089

Wang, L., Talwar, V., Osakada, T., Kuang, A., Guo, Z., Yamaguchi, T., Lin, D., 2019. Hypothalamic Control of Conspecific Self-Defense. Cell Reports 26, 1747-1758.e5. https://doi.org/10.1016/j.celrep.2019.01.078

White, D.A., Kalinichev, M., Holtzman, S.G., 2007. Locomotor Response to Novelty as a Predictor of Reactivity to Aversive Stimuli in the rat. Brain Res 1149, 141–148. https://doi.org/10.1016/j.brainres.2007.02.050

Xu, M., Knox, A.J., Michaelis, K.A., Kiseljak-Vassiliades, K., Kleinschmidt-DeMasters, B.K., Lillehei, K.O., Wierman, M.E., 2012. Reprimo (RPRM) Is a Novel Tumor Suppressor in Pituitary Tumors and Regulates Survival, Proliferation, and Tumorigenicity. Endocrinology 153, 2963–2973. https://doi.org/10.1210/en.2011-2021

Xu, X., Coats, J.K., Yang, C.F., Wang, A., Ahmed, O.M., Alvarado, M., Izumi, T., Shah, N.M., 2012. Modular genetic control of sexually dimorphic behaviors. Cell 148, 596–607. https://doi.org/10.1016/j.cell.2011.12.018

Xu, Y., Nedungadi, T.P., Zhu, L., Sobhani, N., Irani, B.G., Davis, K.E., Zhang, X., Zou, F., Gent, L.M., Hahner, L.D., Khan, S.A., Elias, C.F., Elmquist, J.K., Clegg, D.J., 2011. Distinct Hypothalamic Neurons Mediate Estrogenic Effects on Energy Homeostasis and Reproduction. Cell Metab 14, 453–465. https://doi.org/10.1016/j.cmet.2011.08.009

Yang, C.F., Chiang, M.C., Gray, D.C., Prabhakaran, M., Alvarado, M., Juntti, S.A., Unger, E.K., Wells, J.A., Shah, N.M., 2013. Sexually dimorphic neurons in the ventromedial hypothalamus govern mating in both sexes and aggression in males. Cell 153, 896–909. https://doi.org/10.1016/j.cell.2013.04.017

Yang, S., Tan, Y.L., Wu, X., Wang, J., Sun, J., Liu, A., Gan, L., Shen, B., Zhang, X., Fu, Y., Huang, J., 2021. An mPOA-ARCAgRP pathway modulates cold-evoked eating behavior. Cell Reports 36, 109502. https://doi.org/10.1016/j.celrep.2021.109502

Ye, H., Feng, B., Wang, C., Saito, K., Yang, Y., Ibrahimi, L., Schaul, S., Patel, N., Saenz, L., Luo, P., Lai, P., Torres, V., Kota, M., Dixit, D., Cai, X., Qu, N., Hyseni, I., Yu, K., Jiang, Y., Tong, Q., Sun, Z., Arenkiel, B.R., He, Y., Xu, P., Xu, Y., 2022. An estrogen-sensitive

hypothalamus-midbrain neural circuit controls thermogenesis and physical activity. Sci. Adv. 8, eabk0185. https://doi.org/10.1126/sciadv.abk0185

Ye, Z., Wang, Jin, Shi, W., Zhou, Z., Zhang, Y., Wang, Jingdong, Yang, H., 2023. Reprimo (RPRM) as a Potential Preventive and Therapeutic Target for Radiation-Induced Brain Injury via Multiple Mechanisms. International Journal of Molecular Sciences 24, 17055. https://doi.org/10.3390/ijms242317055

Yin, L., Hashikawa, K., Hashikawa, Y., Osakada, T., Lischinsky, J.E., Diaz, V., Lin, D., 2022. VMHvlICckar cells dynamically control female sexual behaviors over the reproductive cycle. Neuron 110, 3000-3017.e8. https://doi.org/10.1016/j.neuron.2022.06.026

Yoon, N.A., Diano, S., 2021. Hypothalamic glucose-sensing mechanisms. Diabetologia 64, 985–993. https://doi.org/10.1007/s00125-021-05395-6

Yu, S., Qualls-Creekmore, E., Rezai-Zadeh, K., Jiang, Y., Berthoud, H.-R., Morrison, C.D., Derbenev, A.V., Zsombok, A., Münzberg, H., 2016. Glutamatergic Preoptic Area Neurons That Express Leptin Receptors Drive Temperature-Dependent Body Weight Homeostasis. J. Neurosci. 36, 5034–5046. https://doi.org/10.1523/JNEUROSCI.0213-16.2016

Zethof, T.J.J., Van Der Heyden, J.A.M., Tolboom, J.T.B.M., Olivier, B., 1994. Stress-induced hyperthermia in mice: A methodological study. Physiology & Behavior 55, 109–115. https://doi.org/10.1016/0031-9384(94)90017-5

Zhang, Y., Ou, G., Ye, Z., Zhou, Z., Cao, Q., Li, M., Wang, J., Cao, J., Yang, H., 2022. RPRM negatively regulates ATM levels through its nuclear translocation on irradiation mediated by CDK4/6 and IPO11. iScience 25, 105115. https://doi.org/10.1016/j.isci.2022.105115

Zhao, L., Kim, K.W., Ikeda, Y., Anderson, K.K., Beck, L., Chase, S., Tobet, S.A., Parker, K.L., 2008. Central Nervous System-Specific Knockout of Steroidogenic Factor 1 Results in Increased Anxiety-Like Behavior. Mol Endocrinol 22, 1403–1415. https://doi.org/10.1210/me.2008-0034